

`Titania Based Mixed, Binary and Ternary Nanosystems for Clean Energy Generation and Environmental Remediation

*Thesis submitted to the
University of Calicut in partial fulfillment of
the requirement for the degree of*

DOCTOR OF PHILOSOPHY IN CHEMISTRY
In the Faculty of Science

By

JULIYA A. P

Under the Guidance of
Dr. V.M Abdul Mujeeb
Professor (Retd.)



**DEPARTMENT OF CHEMISTRY
UNIVERSITY OF CALICUT
KERALA-673 635
MARCH 2021**

Dr. V.M. Abdul Mujeeb
Professor (Retd.)
Department of Chemistry
University of Calicut.

Calicut University (PO)
Kerala-673635

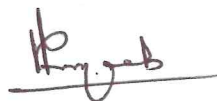
CERTIFICATE

This is to certify that the thesis entitled “**Titania Based Mixed, Binary and Ternary Nanosystems for Clean Energy Generation and Environmental Remediation**” is an authentic record of the research work carried out by Juliya A. P, under my guidance for the award of the degree of Doctor of Philosophy in Chemistry under the faculty of Science, University of Calicut, Kerala and the same has not been submitted elsewhere for a degree or diploma. Certified that all the modifications suggested by the examiners have been incorporated in the thesis.

I also certify that the adjudicators have not suggested any change / corrections in the thesis and recommends to accept in the present form.

19-10-2021

University of Calicut



Dr. V.M. Abdul Mujeeb
(Supervising Teacher)

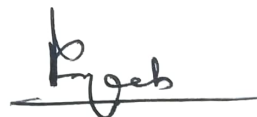
Dr. V.M. Abdul Mujeeb
Professor (Retd.)
Department of Chemistry
University of Calicut.

Calicut University (PO)
Kerala-673635

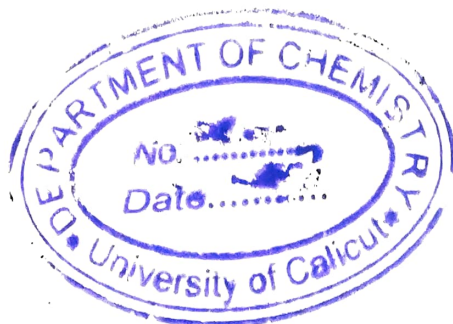
CERTIFICATE

This is to certify that the thesis entitled "**Titania Based Mixed, Binary and Ternary Nanosystems for Clean Energy Generation and Environmental Remediation**" is an authentic record of the research work carried out by Juliya A. P, under my guidance for the award of the degree of Doctor of Philosophy in Chemistry under the faculty of Science, University of Calicut, Kerala and the same has not been submitted elsewhere for a degree or diploma. Certified that all the modifications suggested by the examiners have been incorporated in the thesis.

University of Calicut



Dr. V.M. Abdul Mujeeb
(Supervising Teacher)



DECLARATION

I hereby declare that the thesis entitled “**Titania Based Mixed, Binary and Ternary Nanosystems for Clean Energy Generation and Environmental Remediation**” is the bonafide report of the original work carried out by me under the supervision of Dr. V.M. Abdul Mujeeb, Professor, Department of Chemistry, University of Calicut, and Co-supervision of Dr. K Muraleedharan, Professor, Department of Chemistry, University of Calicut and Dr Sreenivasan K.P, Assistant Professor, PG and Research Department of Chemistry, MES Kalladi College, Mannarkkad for the award of the degree of Doctor of Philosophy in Chemistry Under the Faculty of Sciences, University of Calicut, Kerala. The content of this thesis have not been submitted to any other institute or University for the award of any degree or diploma.

Calicut University
22-3-2021



Juliya A.P.

ACKNOWLEDGEMENTS

First of all, I am grateful to the most gracious and merciful God, the almighty for showering blessings for the accomplishment of my research work. The completion of my research work would not have been possible without the assistance of so many people whose names may not all be mentioned. Their contributions are sincerely appreciated and gratefully acknowledged.

I would like to express my deep sense of gratitude to my supervisor, Dr. V.M Abdul Mujeeb, Professor, Department of Chemistry, University of Calicut. I express my heartfelt thanks to him for his valuable advice, scholastic suggestions, continuous support, patience, motivation, encouragement and timely corrections. His guidance helped me in all perspectives.

I am thankful to my co-guides Dr. K Muraleedharan, Professor, Department of Chemistry, University of Calicut, and Dr. Sreenivasan K.P, Assistant Professor, Department of Chemistry, MES Kalladi college, Mannarkkad for their meticulous dynamic guidance, encouragement, and comprehensive discussions that helped me for the completion of my work.

I would like to thank all the faculties of Chemistry department, University of Calicut for their valuable support. I would also like to extend my sincere thanks to all non-teaching staff of my department. I thank Mr. K. Satheesan for the technical assistance he has provided throughout my research work.

I thank my fellow researchers Nadira, Dr. Nikhila M. P, Dr Sindhu, Akhila A. K., Nusrath Riyas, Dr. Jyothy P.R, Ansi V.A, Varsha Raveendran, Dr. Sanjay Gopal, Soufeena, Sabira, Jayaram. P for the thought-provoking discussions and co-operation offered to me during the work.

I express my sincere gratitude to Dr. Nandini Devi, Scientist, Catalysis and Inorganic Chemistry Division, CSIR-National Chemical Laboratory for providing me an opportunity to conduct water splitting studies from NCL Pune. I also extend my heartfelt thanks to Ms. Priyanka, Mr. Anurag, Ms. Deepali, research scholars at NCL Pune for their support and care.

I would like to thank STIC – Cochin CUSAT, Amrita Institute of Nanoscience, CSIF- University of Calicut, and NCL Pune for helping with the characterization part.

I would like to acknowledge my colleagues Dr.T.N Muhammed Musthafa, Nusrath. P, Sajna. P, Fausia. K. H, Raseena A, Dr. Mumthaz A.K for their sincere support. It's my pleasure to mention here the names of my friends Dr. Biyas Posha, Shimi. M, Najina. P, Vijitha Murali, Dr. Shaniba C.P, Dr. Yasmine C.K, Nabila Haneef and Achudhanendh for their everlasting love, support, and motivation.

My parents (Abdu. A.P and Laila. P.A) are my inspiration. I am forever indebted to them for giving me the opportunities, inspiration, and motivations that have made me who I am. I would not have submitted my work without their generous help, care, and encouragement. My deep sincere gratitude to my parents for their

continuous and unparalleled love, help, and support. A special thanks to my husband (Shinu. E) for all of the sacrifices that he made on my behalf. He has been inspiring, motivating, encouraging tremendously for the successful completion of my venture. Thanks for all your support without which I would have stopped these studies a long time ago. For my daughter, Eshana, sorry for being even grumpier than normal whilst I wrote my thesis. My special thanks to my sister (Rubiya. A. P), brother-in-law (Jahas. P), and their son (Khaleel Rahman) for their affection and support. I am thankful to my mother-in-law (Amina) and father-in-law (Muhammed. E) for their care and support. I would like to extend my sincere thanks to my brother in laws Shaneeb, Shabeeb, and sister-in-law Sona for their love and support.

I express my apology that I could not mention one by one.

Juliya. A.P

*Dedicated To
My
Uppa, Umma, Ikka
and
Kunjatta*

CONTENTS

<i>Chapter</i>	<i>Title</i>	<i>Page No.</i>
1.	Introduction	1-35
2.	Experimental methods and characterization techniques	37-54
3.	Sunlight assisted photocatalytic degradation of methylene blue via mesoporous TiO ₂ /RuO ₂ binary nanosystem	55-87
4.	Synthesis and characterization of mesoporous TiO ₂ /RuO ₂ /CuO ternary nanosystem	89-116
5.	Photocatalytic H ₂ evolution using TiO ₂ /RuO ₂ /CuO ternary nanosystem	117-138
6.	Photocatalytic degradation of cefixime using TiO ₂ /RuO ₂ /CuO under sunlight irradiation	139-161
7.	Synthesis of TiO ₂ /ZnO/Fe ₂ O ₃ nanocomposite for photocatalytic degradation of methylene blue	163-186
8.	Comparative study on photocatalytic degradation of methylene blue using strontium titanate synthesized in the presence and absence of pluronic P123	187-209
9.	Overall conclusion and future outlook	211-216

PREFACE

Environmental pollution brought about by urbanization and industrialization is one of the prime issues faced by the 21st century. The world is under the grip of various harmful pollutants. This creates the necessity for an effective mineralization process for the removal of harmful pollutants. Heterogeneous photocatalysis is a superior technique for the removal of pollutants in comparison to that of conventional methods. The depletion of fossil fuels has created necessity for the generation of energy sources. Photocatalytic water splitting is a promising technique for the generation of H₂. The present endeavour is focused on energy generation and environmental remediation via photocatalysis using titania-based mixed binary and ternary nanosystem.

Owing to favorable band gap and band edge positions various semiconducting metal oxides can be used as photocatalysts. The semiconducting metal oxides on irradiation with light of suitable frequency that matches with its band gap generates electron-hole pairs. The electrons on reaction with surface adsorbed oxygen produce superoxide anions, whereas holes generate free radicals on reaction with water molecules. The free radicals generated are highly oxidizing enough to detoxify harmful pollutants. Among the various semiconductors, TiO₂ serves to be the most widely explored photocatalyst. Low visible light sensitivity and faster electron-hole recombination are the major drawbacks of TiO₂. In this regard, we have

adopted strategies like coupling with semiconductors and development of the mesoporous structure to improve photocatalytic activity.

We have attempted to synthesize mixed, binary, and ternary nanosystem via sol-gel and sol-gel combustion method. The morphology, crystal phases, and porosity of the prepared catalysts were evaluated by various characterization techniques. We have also investigated the applicability of the catalysts in various areas like photocatalytic dye degradation, drug degradation, and water splitting.

In the third chapter, sol-gel method was designed for the synthesis of $\text{TiO}_2/\text{RuO}_2$ binary nanosystem. Sunlight-assisted photocatalytic degradation of methylene blue was conducted using the prepared sample. The next motive was to synthesize $\text{TiO}_2/\text{RuO}_2/\text{CuO}$ ternary nanosystem. Detailed analysis of various characterization techniques was presented in chapter 4. The fifth chapter presents the photocatalytic water splitting studies performed using $\text{TiO}_2/\text{RuO}_2/\text{CuO}$ ternary nanosystem. The sixth chapter comprises the photocatalytic drug degradation experiment conducted using $\text{TiO}_2/\text{RuO}_2/\text{CuO}$ ternary nanosystem. The seventh chapter comprises the synthesis of $\text{TiO}_2/\text{ZnO}/\text{Fe}_2\text{O}_3$ nanocomposite via sol-gel method. Photocatalytic dye degradation experiments were conducted under UV and sunlight irradiation using the ternary nanocomposite. In the eighth chapter, a comparative study on photocatalysis was performed using strontium titanate prepared in the presence and absence of pluronic P123.

CHAPTER 1

INTRODUCTION

Contents

- 1.1 *Environmental pollution*
 - 1.2 *Advanced oxidative process*
 - 1.3 *Heterogenous photocatalysis*
 - 1.4 *Semiconductor as photocatalyst*
 - 1.4.1 *Titanium dioxide*
 - 1.4.2 *Zinc oxide*
 - 1.4.3 *Strontium titanate*
 - 1.4.4 *Ruthenium dioxide*
 - 1.5 *Method of preparation of semiconducting metal oxides*
 - 1.5.1 *Sol -gel method*
 - 1.5.2 *Sol-gel combustion method*
 - 1.6 *Photocatalytic material*
 - 1.7 *Molding of semiconductor as an efficient photocatalyst*
 - 1.7.1 *Synthesis of mesoporous semiconductor*
 - 1.7.2 *Coupling with suitable semiconductors*
 - 1.8 *Applications of heterogenous photocatalysis*
 - 1.8.1 *Dye degradation*
 - 1.8.2 *Drug degradation*
 - 1.8.3 *Water splitting*
 - 1.9 *Objectives*
 - 1.10 *Overview of the experimental work*
-

1.1 Environmental pollution

The environmental pollution brought about by hazardous pollutants that are being derived as an outcome of industrialization is one of the prime concerns of environmentalist¹. Huge amount of synthetic organics like industrial, chemicals, pesticides, dyes, pharmaceuticals are released into the water streams². Most of these pollutants are highly toxic and carcinogenic. Various methods like biological, physical, and chemical oxidation methods are suggested for the water treatment process. The biodegradation of the recalcitrant pollutants is quite slow and their conventional treatment creates a deleterious effect on the ecology and hence seems to be ineffective³. However, the traditional physical methods like coagulation, flocculation, adsorption, and ultrafiltration are non-destructive as they just involve the transfer of contaminants from one phase to another⁴. The conventional chemical water treatment methods like sedimentation, filtration, chemical, and membrane technologies are costly and involve the production of secondary pollutants⁵. In this scenario, there needs an efficient system that has the capability for complete mineralization of organic pollutants. To overcome the limitations imposed by these conventional methods and to protect the natural treasure, advanced oxidative process was proposed as a promising technology for wastewater treatment. It is the need of the hour since unparalleled urbanization leads to facing lack of water.

1.2 Advanced oxidative process

Advanced oxidative process involves the production of highly oxidizing hydroxyl radicals (OH \cdot) for the mineralization of toxic pollutants⁶ with the use of innovative technology. Advanced oxidative process includes the generation of hydroxyl radicals by a series of methods like ozonation, photocatalysis, electrochemical oxidation, Fenton, and Fenton-like processes⁷. The hydroxyl radicals are highly oxidizing, unstable, and reactive. Through the various process technologies adopted for the advanced oxidative process, it is possible to oxidize trace organic chemicals, that is impossible via conventional methods. Among the various advanced oxidative processes, titanium dioxide/UV light process, hydrogen peroxide/UV light process, and Fenton's reactions are the most widely used ones⁸. The transient species formed in the advanced oxidative process abstracts hydrogen from the organic pollutant, generating organic radicals that undergo a series of degradation processes finally producing biodegradable components. Based on the methodology of OH \cdot generation, the advanced oxidation process can be classified into chemical, electrochemical, sonochemical, and photochemical processes, and based on the phase they can be classified into homogeneous and heterogeneous process. Homogenous photocatalysis utilizes Fenton's reagent (mixture of H₂O₂ and Fe²⁺ salt) whereas heterogeneous photocatalysis utilizes semiconducting oxides for the generation of OH \cdot ⁹. Heterogeneous photocatalysis is ubiquitous among the various advanced oxidative processes as it leads to the complete mineralization of recalcitrant pollutants at ambient temperature and low cost¹⁰.

1.3 Heterogeneous photocatalysis

Heterogeneous photocatalysis can be defined as the acceleration of photoreaction in the presence of light on the surface of the photocatalyst. Water splitting and detoxification of pollutants are the two main applications of heterogeneous photocatalysis. The heterogeneous photocatalytic oxidation process involving semiconductors and UV light has achieved promising results for the mineralization of recalcitrant pollutants¹¹. As H₂ is produced from fossil fuels that are in the edge of extinction, there should be some alternative for H₂ production. Photocatalytic H₂ production will be an ideal solution for the existing energy crisis. They were Honda and Fujishima who led the substratum for heterogenous photocatalysis in 1972 with the evolution of H₂ from water. In heterogeneous photocatalysis, the semiconductors on illumination with light of suitable frequency that is matching with its band gap gets excited resulting in the generation of electron- hole pairs which degrade the pollutants after undergoing a series of redox processes. Various semiconductors like TiO₂, ZnO, ZnS, Fe₂O₃, and CdS can be used as photocatalysts for the detoxification process due to the filled valence band and empty conduction band in the electronic structure of such metal atoms in combination¹².

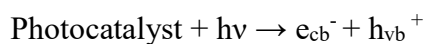
1.4 Semiconductor as photocatalyst

For the last few decades, semiconductors act as excellent photocatalytic material for the environmental remediation process. Semiconductor photocatalysis is used in various areas like degradation

of recalcitrant pollutants, antibacterial activity, deterioration of cancer cells, H₂ production, solar cells, and N₂ fixation¹³. Various strategies are adopted to improve the photocatalytic efficiency of semiconductors i.e., textural design¹⁴, doping¹⁵, noble metal loading¹⁶, and forming semiconductor composites¹⁷. A semiconductor material is characterized by three regimes in which the highest occupied energy band called valence band; lowest energy conduction band are separated by forbidden energy band. The activation of semiconductors occurs with the absorption of a photon of ultra-band gap energy¹⁸. The semiconductor material on irradiation with energy equal to or greater than the band gap energy creates photo-excited electron-hole pairs. The electron-hole pairs can undergo recombination or get trapped in metastable surface states or initiate a series of redox reactions after migrating to the surface of photocatalyst¹⁹. The detailed mechanism of degradation of pollutants is described in the following equations.

1. Photoexcitation

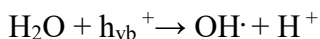
As mentioned earlier the semiconductor on the absorption of photon of energy either equal to or greater than its band gap gets excited and promotes electron from the valence band to conduction band simultaneously leaving hole in the valence band.



2. Conversion of holes to hydroxyl radicals

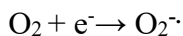
The holes on reaction with the water adsorbed on the photocatalyst, producing highly oxidizing hydroxyl free radical (OH[•]). It is the highly

oxidizing hydroxyl radicals that undergo the degradation of hazardous pollutants.



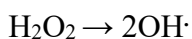
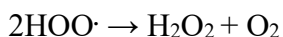
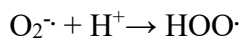
3. Generation of superoxide anion

The electrons react with surface adsorbed oxygen producing superoxide anion that can react with pollutants generating hydroperoxide radical.



4. Conversion of superoxide anion to hydroxyl radical

Superoxide anion on protonation is converted to hydroperoxide radical which subsequently dissociates producing hydroxyl radical.



Finally, the recalcitrant pollutants react with hydroxyl radicals producing CO_2 and H_2O .

Schematic representation of photocatalysis is presented below:

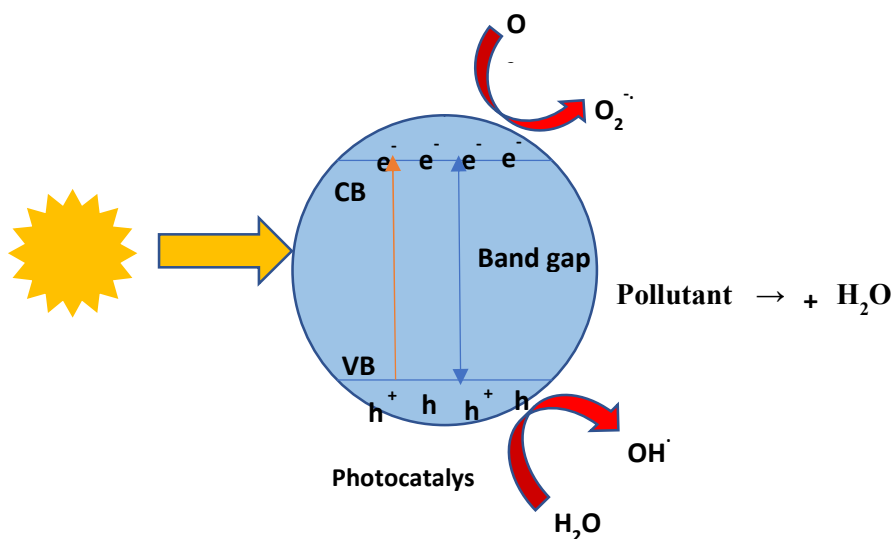


Figure 1.1 Schematic diagram illustrating pollutant degradation

For photocatalytic water splitting, the semiconductors should possess properly located valence and conduction band edges i.e., the thermodynamic requirement of water splitting implies that the conduction band edge of the semiconductor should be more negative than the reduction potential of water for H_2 evolution whereas the valence band edge should be more positive than the oxidation potential of water for O_2 evolution²⁰. The performance of photocatalyst depends mainly on the absorbance capacity and effective separation of photogenerated electron-hole pairs. The photocatalytic water splitting using semiconductor photocatalyst is illustrated below.

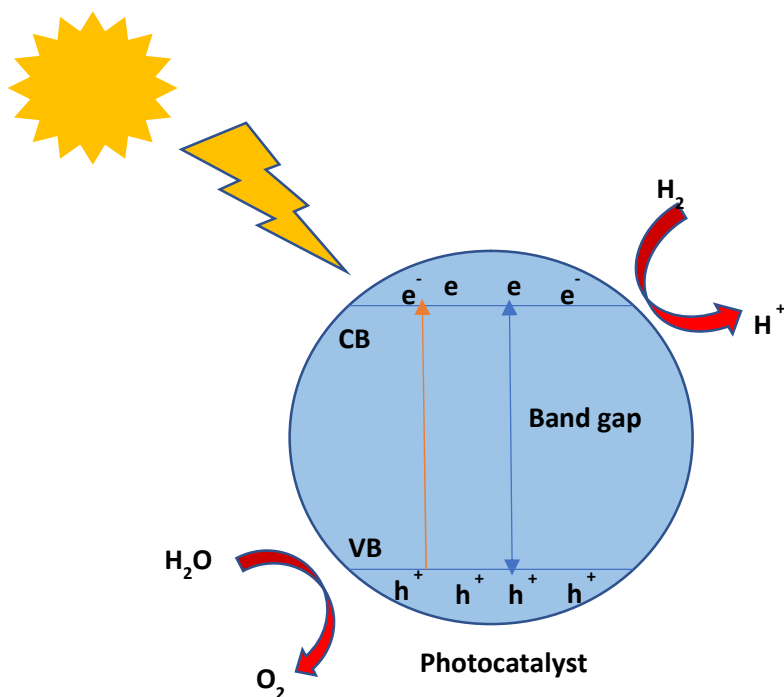


Figure 1.2 schematic diagram illustrating water splitting

1.4.1 Titanium dioxide (TiO₂)

Titanium dioxide is the most versatile semiconductor with potential applications in catalysis, photocatalysis, energy storage, gas sensors, dye-sensitized solar cells, and photovoltaics²¹⁻²². Titanium dioxide exists in three different polymorphs, brookite, anatase, and rutile. Rutile is thermodynamically the most stable structure whereas anatase and brookite are metastable and get converted to rutile form on heating²³. Anatase is the kinetically stable structure. TiO₂ is formed from distorted TiO₆ octahedra in which each Ti atom is surrounded by six O₂ atoms. The unit cell of tetragonal anatase consists of four TiO₂

units (12 atoms), whereas the unit cell of tetragonal rutile contains two TiO_2 units (6 atoms), and the unit cell of orthorhombic brookite contains eight TiO_2 units (24 atoms)²⁴. After all, in the case of anatase, the octahedra are connected by their vertices, in rutile by edges whereas in brookite they are connected both by edges and vertices. The crystal structure of rutile and anatase differ by the distortion in the octahedra. In rutile, the octahedra are irregular with slight orthorhombic distortion whereas in anatase it is distorted to a large extent with asymmetry lower than that of orthorhombic. The crystallographic representation of polymorphs of TiO_2 is shown in Figure 1.3. On comparison to the other two polymorphs anatase phase is most preferred for photocatalytic applications. Though anatase is having lower absorbance towards solar light due to the larger band gap (3.2) in comparison to that of rutile (3) the higher surface adsorption capacity towards hydroxyl group and longer life time of photogenerated electrons and holes make anatase more photoactive than rutile². It is difficult to synthesize brookite in the laboratory. Anatase and rutile are commonly used for photocatalytic studies. TiO_2 on irradiation with UV light with a wavelength less than 385 nm are capable of degrading pollutants utilizing the holes and hydroxyl radicals generated at valence band and electrons, and superoxide anion radicals generated at conduction band during the photocatalytic process²⁶. The superior properties of TiO_2 like low-cost synthesis, high physical and chemical stability, optical and electronic properties, eco-friendliness, non-toxicity, non-corrosive nature makes TiO_2 a promising candidate for various practical applications²⁷⁻²⁸. Despite all these positive factors some limitations set aside TiO_2 as a good photocatalyst. The large band gap (3.2) hinders the TiO_2 from effective

utilization of solar energy and reduces its photocatalytic efficiency²⁹. Moreover, the high chance of electron-hole recombination also affects the photocatalytic performance of TiO₂. Scientists have developed various strategies to improve the photocatalytic activity of TiO₂. The physical properties of TiO₂ are determined by various factors like phase, pore, particle size, and surface area. The modification of TiO₂ has been accomplished by various methods like doping³⁰, photosensitization³¹, coupling with semiconductors³², and addition of sacrificial agent³³. Solar energy is an inexhaustible form of energy. With the breakthroughs in the modification of TiO₂, it has been manifested that solar energy can be effectively utilized for energy crises and environmental issues. There is an economic logic too to renewable energy. These unique properties unambiguously demonstrate the application of TiO₂ in various fields like solar cells, dye degradation, water splitting, cosmetics, paints, drug delivery, etc., and equally important, it will help to provide power in an environmentally sustainable fashion.

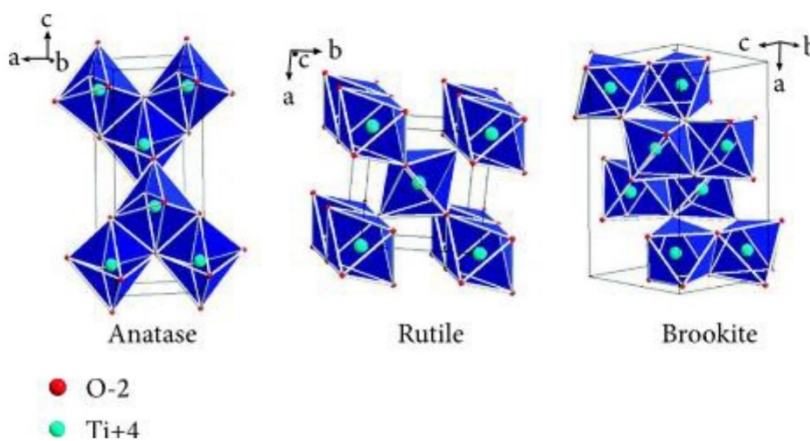


Figure 1.3 Crystalline forms of TiO₂

1.4.1.1 Electronic structure of TiO₂

In the case of Ti⁴⁺, the t_{2g} band is empty as there are no valence electrons. Here the band gap is the energy gap between the filled p band which is the valence band and the empty t_{2g} conduction band. The energy difference between the filled p band of TiO₂ and the empty t_{2g} band constitutes the band gap which was found to be 3.2 in the case of anatase and 3.1 in the case of rutile and both comes under UV range.

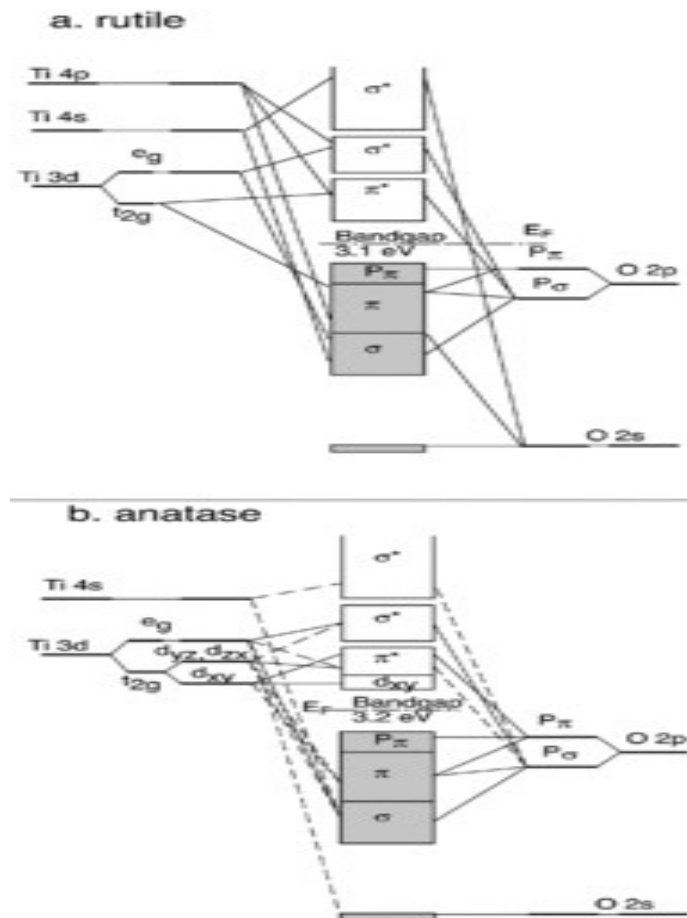


Figure 1.4 Band diagram of TiO₂

1.4.2 Zinc oxide

ZnO is a wide band gap semiconductor (3.37 eV) that has been a subject of focused research due to the amazing electrical, mechanical, optical, magnetic, physical, and chemical properties. Wurtzite, zinc blende, and rock salt are the three different crystalline structures of ZnO. Among these structures, the hexagonal wurtzite form is the most common and stable structure³⁴. Stabilization of zinc blend can be achieved by growing ZnO on substrates with cubic lattice structure. Wurtzite ZnO consists of hexagonal structure, with lattice parameters $a = 0.3296$ and $c = 0.52065$ nm³⁵. In ZnO each ZnO is tetrahedrally surrounded by four O₂ atoms and vice versa. It is the tetrahedral coordination in ZnO with the lack of central symmetric structure that contributed to the piezo and piero electricity. ZnO is a versatile semiconductor with a wide variety of morphologies. ZnO can appear in one (1-D), two (2-D) and three-dimensional (3-D) structures. One dimensional structure constitutes the major group that includes nanorods, needles, helixes, springs and rings, ribbons, tubes, belts, wires, and combs³⁶⁻⁴³. Zinc oxide also occurs in 2D structures like nanoplate/nanosheet and nanopellets⁴⁴⁻⁴⁵. The three-dimensional forms of ZnO include flower, dandelion, snowflakes, and coniferous urchin⁴⁶⁻⁴⁹. The properties that make ZnO distinct are unique physical, chemical properties and optical properties, thermal and mechanical stability, piezo and pyroelectrical properties, high band gap, and high bond energy⁵⁰. These unique properties of ZnO unambiguously demonstrate the application of ZnO in various fields like UV lasers⁵¹, light-emitting diodes⁵², solar cells⁵³, nanogenerators⁵⁴, gas sensors⁵⁵, photodetectors⁵⁶, and photocatalysts⁵⁷. ZnO can be synthesized via

various processes like mechanical ball milling, mechanochemical process laser ablation, hydrothermal method, sol-gel method, chemical bath deposition, wet chemical process, and green synthesis.⁵⁸

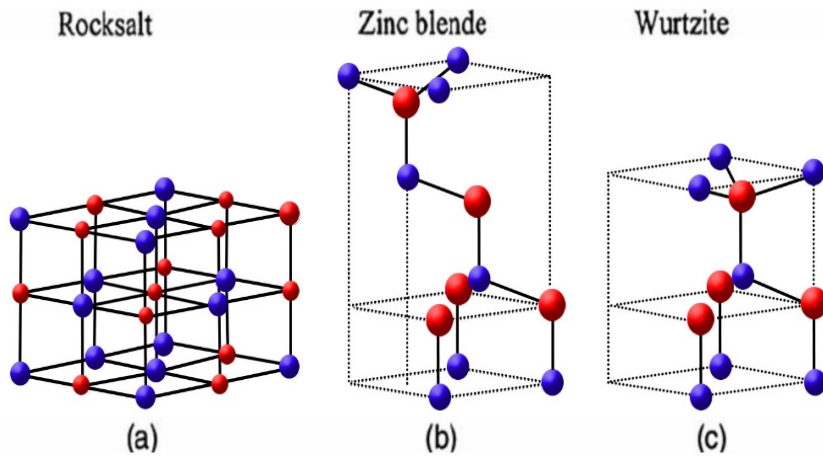


Figure 1.5 Crystalline forms of TiO₂

1.4.3 Strontium titanate

Strontium titanate is a complex oxide material with perovskite structure⁵⁸. Perovskites are ternary compounds with the general formula ABX₃ with two cations in the same ratio and an anion that is either O or F. Strontium titanate possesses cubic perovskite structure at ambient temperature. At 110 °C strontium titanate is in tetragonal phase and at 65 °C in orthorhombic phase⁵⁹. SrTiO₃ is chemically stable and possesses high melting point of 2080 °C⁶⁰. SrTiO₃ is ecofriendly and cost-effective semiconductor with a wide band gap of 3.15 eV. STO is a potential ferroelectric material in which the ferroelectric transition is suppressed by quantum fluctuation⁶¹. Strontium titanate is one of the widely studied materials as it exhibits

interesting features like dielectric and ferroelectric properties, thermoelectric properties, thermal, photo, and structural stability and, unique physical and chemical properties⁶²⁻⁶⁵. To improve the photocatalytic performance by extending visible absorption and increasing the lifetime of photogenerated charge carriers, various modifications like doping with metals and non-metals⁶⁶, coupling with semiconductors⁶⁷, and molding the textural properties using structure directing agents⁶⁸. Strontium titanate is an efficient catalyst with diverse range of applications like electro-ceramics and electronic or optoelectronic devices, photoelectrode in electrochemical cells for water splitting, photocatalytic degradation of dyes, photocatalytic water splitting, dilute magnetic semiconducting application, and solar cells⁶⁹⁻⁷². Various synthetic strategies are adopted for the reaction of Strontium titanate. Thermal decomposition, sol-gel method, hydrothermal method, solid-state reaction, combustion synthesis, and coprecipitation reactions are the commonly employed methods⁶⁷.

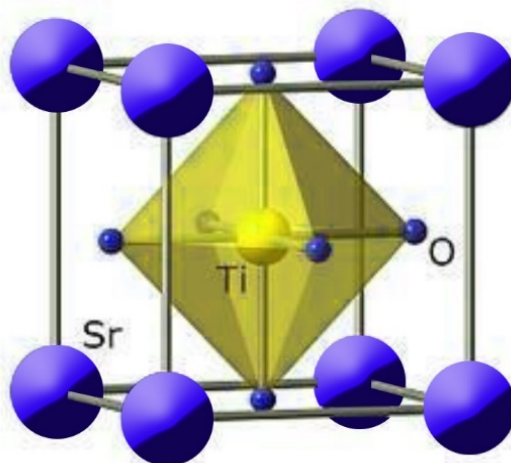


Figure 1.6 Crystalline forms of SrTiO₃

1.4.4 Ruthenium dioxide

Ruthenium dioxide, the thermodynamically most stable oxide of ruthenium possesses unique surface chemistry that renders it as oxidation catalyst⁷³⁻⁷⁴. The stable solid-state anhydrous form of ruthenium dioxide mainly adopts rutile structure with a greater probability to attain RuO_6 octahedra with four oxygen ions at 1.984 Å and two axial oxygen ions at 1.942 Å from the Ru^{4+} ⁷⁵. The electrical resistivity of RuO_2 is 35 $\mu\Omega\text{cm}$ which is an indication of high conductivity of the oxide⁷⁶. The molecular orbital theory explained well the high thermodynamic stability and charge transfer property of ruthenium⁷⁷. RuO_2 based catalysts have been explored due to the fascinating features like diffusion barrier properties, high thermal stability, low-temperature resistivity, electrical conductivity, electrochemical stability, and intermediate hydrogen over potential⁷⁸⁻⁷⁹. RuO_2 has a variety of useful application in various fields likes supercapacitors, electrodes, electrochemical capacitors, electrodes, gas sensors, oxidation reactions, photochemical water decomposition, electrochemical evolution of chlorine, and oxygen⁸⁰⁻⁸².

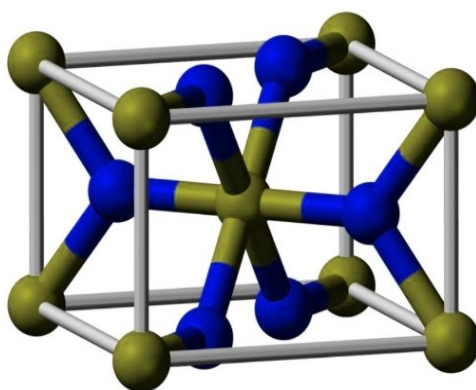


Figure 1.7 Crystalline form of RuO_2

1.5 Method of preparation of semiconducting metal oxides

Various preparative methods like sol-gel⁸³, sol-gel-combustion⁸⁴, solvothermal method⁸⁵, hydrothermal method⁸⁶, chemical vapor deposition⁸⁷, microwave-assisted synthesis⁸⁸ etc. are followed for the successful synthesis of semiconducting metal oxides. We have employed the sol-gel method and sol-gel combustion method for the present research.

1.5.1 Sol-gel method

The sol-gel (SG) technique is a wet chemical process that has emerged as one of the superior methods for the synthesis of glass, ceramics, and organic-inorganic hybrid from colloidal solutions⁸⁹. The process involves the formation of liquid suspension called sol that is subsequently converted to solid gel. Initially, the metal hydroxides or inorganic metal salts undergo a hydrolysis reaction producing a colloidal solution called sol. This is followed by condensation resulting the formation of a 3-dimensional gel. Based on the method of the drying process, xerogel or aerogel are formed. On the basis of the solvent used the sol-gel method can be classified into aqueous sol-gel method and non-aqueous sol-gel method. In the case of aqueous sol-gel method water is the solvent whereas in non-aqueous sol-gel process organic solvent is used⁹⁰. The sol-gel method possesses various advantages like low cost, homogenous distribution of components, low-temperature synthesis, and better control of the morphology of the particles⁹¹.

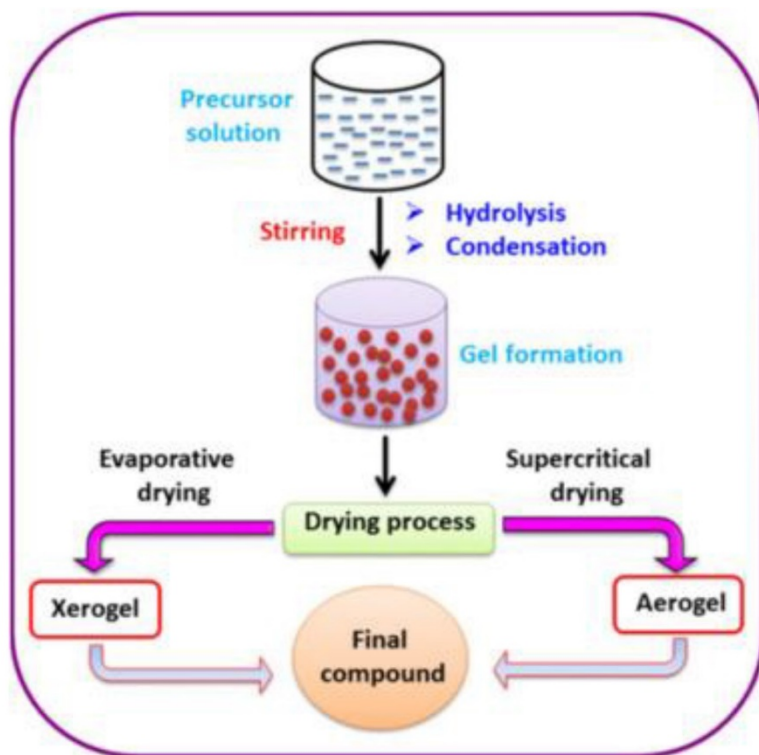


Figure 1.8 schematic diagram illustrating the sol-gel process

1.5.2 Sol-gel combustion method

Sol-gel combustion method is one of the cost-effective methods for the synthesis of pure, homogenous, and crystalline oxide powder⁹². This method involves the chemical combination of sol-gel followed by the combustion process. Initially, a gel is formed from the aqueous solution containing metal salt by the sol-gel method. The gelation is followed by the combustion of gel resulting formation of voluminous fluffy powder of large surface area. The sol-gel combustion method is based on the principle of propellant chemistry⁹³. Various factors like

the condition of the synthesis, nature of the fuel, fuel/metal nitrate ratio, pH, and annealing temperature affect the formation of products⁹⁴. The main advantages of the sol-gel combustion method are the formation of homogenous, high purity, quality, high-density ceramics with luminescence properties, and controllable stereochemistry⁹⁵⁻⁹⁶.

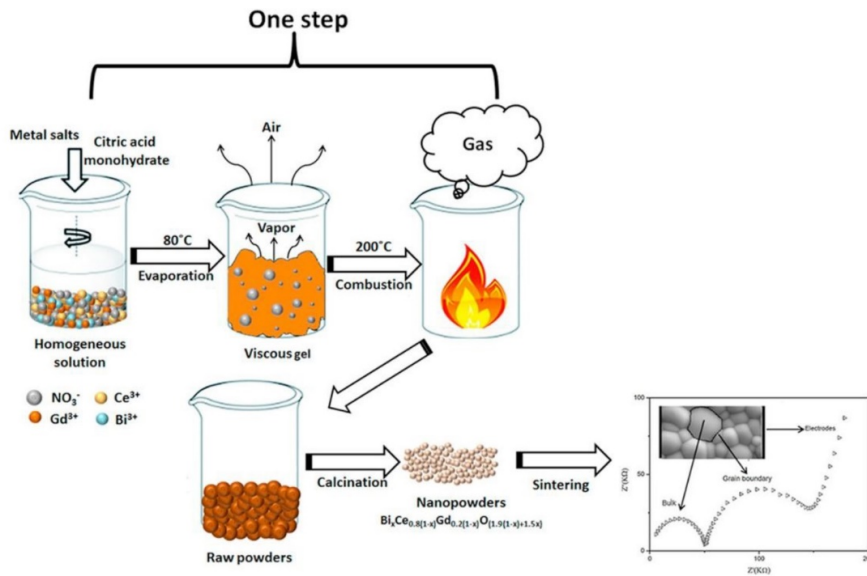


Figure 1.9 schematic diagram illustrating the sol-gel process

1.6 Photocatalytic material

Various semiconducting materials like TiO₂, ZnO, CdS, Fe₂O₃, etc. have been explored as photocatalytic material with a wide range of potential applications like dye degradation, water splitting, CO₂ reduction, antibacterial activity, fuel generation etc⁹⁷. Photocatalyst on irradiation with photon of energy equal to or greater than its band gap

promotes an electron from valence band to conduction band simultaneously generating holes in the valence band. The generated photoexcitons can either recombine or dissipate the energy as heat or get trapped in metastable surface states or undergo a series of redox reactions. To be an ideal photocatalyst the semiconductor should possess the following features i.e., the semiconductor should be⁹⁸⁻⁹⁹.

- Cheap
- Easily available
- Lack of toxicity
- Possess high surface area
- Efficient charge separation
- High mobility of charge carriers
- Chemically inert and stable
- Efficiently utilize solar energy
- Photoactive
- Ecofriendly

Semiconductors with these properties have proved to be efficient photocatalysts with diverse applications. However various shortages like poor visible light absorption and electron-hole recombination of the samples result in poor efficiency of the catalysts. The aforementioned facts can be overcome by modifying the structure of photocatalysts in various ways.

1.7 Molding of the semiconductor as an efficient photocatalyst

UV light covers only 4-5 % of the solar spectrum whereas visible light covers 40 %. The band gap of TiO₂ is 3.2 eV. So TiO₂ cannot efficiently utilize the solar spectrum. TiO₂ can only be activated by UV irradiation. This makes TiO₂ ineffective for the efficient utilization of solar energy. Various strategies are adopted to modify the photocatalyst so as to improve the efficiency of photocatalysis. Some of the strategies that we have adopted in our present research work are mentioned here¹⁰⁰.

1.7.1 Synthesis of mesoporous semiconductor

The mesoporous materials have gained great importance owing to their potential applications in various fields like catalysis, adsorption, separation, sensing, medical usage, ecology, and gas separators energy converters^{101 -102}. According to IUPAC definition the materials with pore size 2-50 nm are categorized into mesoporous materials. Mesoporous materials can be synthesized in the presence and absence of templates. Triblock copolymers like pluronic (P123) and pluronic (F127), diblock copolymer brij 56 (B56nly), other surfactants like tetradecyl phosphate, dodecyl phosphate, tetradecylamine, dodecyl ammonium chloride (DDAC), cetyl methyl ammonium bromide (CTAB) are the commonly used structure-directing agents applied for the synthesis of mesoporous structures¹⁰². Various physical properties such as porosity, surface area, and crystallinity have a pronounced influence on enhancing photocatalytic activity¹⁰³. As the mesoporous structures have these desirable features they are highly recommended

for various photocatalytic applications. With the increase in surface area of the semiconductor, the number of active sites increases, which leads to the greater absorption of pollutants on the catalyst surface leading to greater photocatalytic activity. The large surface area and the mesoporous channel favor the mass transfer and enhance the activity.

Pluronic is a high molecular weight amphiphilic triblock copolymer that consists of poly (ethylene oxide)-poly (propylene oxide)-poly (ethylene oxide) (PEO-PPO-PEO) i.e., central hydrophobic polymer block of polypropylene oxide, flanked by two polyethylene oxide blocks. The chemical formula of pluronic P123 is (ethylene oxide)₂₀-(propylene oxide)₇₀-(ethylene oxide)₂₀. Block copolymer (Pluronic P123) plays a prominent role in controlling the hydrolysis and condensation reaction in sol-gel processes for the synthesis of mesoporous materials¹⁰⁴. The long hydrophilic chain present in pluronic P123 enables the synthesis of mesoporous oxide with high thermal stability. Marien et al synthesized mesoporous TiO₂ via sol-gel method using pluronic P123 as a structure-directing agent and the studies indicated that P123 had a profound influence on the control of the morphology of prepared TiO₂¹⁰⁵. Pluronic P123 assisted sol-gel method resulted in the formation of spherical and rod-shaped TiO₂ nanoparticles with high photocatalytic activity in comparison to that of commercial P25 samples¹⁰⁶.

1.7.2 Coupling with suitable semiconductors

Another strategy to improve photocatalytic activity is by coupling with semiconductors. To overcome the shortcoming of TiO_2 that can absorb only in the UV region, the use of heterojunctions is widely employed. The heterojunctions formed can increase the photocatalytic activity of the semiconductors. In the case of the coupled system of semiconductors enhanced activity is observed on account of the optical absorption, vectorial transfer of charge carriers from one semiconductor to that of other, and efficient separation of the charge carriers^{107, 108}. On the basis of band gap energies and valence band and conduction band edges the electronic structure of the semiconducting photocatalysts can be classified into three types, i.e., straddling gap (type I), staggered gap (type II) and broken gap (type III) heterojunctions. In the case of type I structures the conduction band of the large band gap semiconductor is placed above the conduction band of the other one whereas its valence band is below the valence band of the low band gap semiconductor. Here the electrons and holes from large band gap semiconductors are transferred to that of small band gap semiconductors. Hence the electrons get accumulated in the small band gap semiconductor. In type II heterojunctions as the conduction band edge potential of the large band gap semiconductor is more negative than that of the other the electrons will be transferred to the small band gap semiconductor. At the same time holes from the valence band of small band gap semiconductor are transferred to that of large band gap semiconductor. Here the electrons and holes are effectively separated and the photocatalytic activity will increase. Type

III structure is similar to that of type II except the fact that there is large difference in the valence band and conduction band energy levels of the semiconductors which provides a greater driving force for the charge transfer.

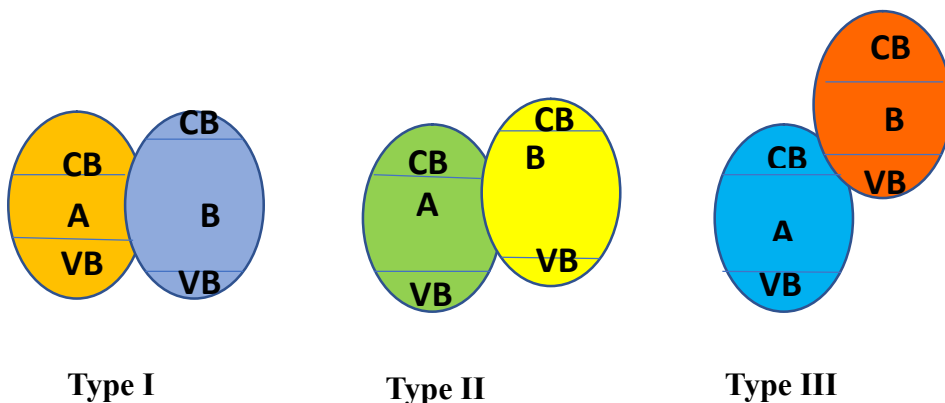


Figure 1.10 Classification of coupled semiconductors on the basis of the valence band and conduction band edges

1.8 Applications of heterogeneous photocatalysis

1.8.1 Dye degradation

As color is the main attraction of a product, it is an inevitable part of the commercialization of a substance. Colors provide a pleasing appearance to the commodities. Dyes are colored substance that binds to the substrate to which it is being applied. About 12 % of dyes are lost into the environment during the manufacturing process¹⁰⁹. The textile industries constitute one of the major polluting industries. The other industries that release dyes into the environment are the leather industry, paper industry, hair coloring industry, and the food industry¹¹⁰. The deleterious effect of the effluents released from the

textile industries is a major threat to aquatic life, human beings, and microorganisms¹¹¹. Effluents released from textile industries include surfactants and organic pollutants that are highly carcinogenic and toxic. Initially, various physical methods like adsorption, ultra-filtration, and reverse osmosis were used for the degradation process. Activated carbon, zeolites, silicon-based adsorbents, agricultural wastes, etc. were used as adsorbents for dye removal. However various shortcomings like the requirement of more time and space were addressed during the removal process. The traditional biological methods (biodegradation) too proved to be inefficient for the degradation of recalcitrant pollutants. Earlier chemical processes like coagulation, flocculation, chlorination, ozonation, etc. were employed for dye removal. A high degree of aromatization and high stability was observed in the dye molecules¹¹². All these conventional methods were proved to be inefficient as all these processes were nondestructive and resulted in the formation of secondary pollutants by mere transfer of pollutants from one phase to another. With the emergence of the advanced oxidative process, all these shortcomings were solved to an extent. In the advanced oxidative process hydroxyl radicals generated were responsible for the complete mineralization of dye molecules. Among the various advanced oxidative processes like Fenton based process, UV based process, ozone-based process, and photocatalytic process, the photocatalytic process seems to be the most efficient one, as it is environmentally friendly, carried out at ordinary temperature, and leads to the complete oxidation of pollutants into CO₂ and H₂O¹¹³. Methylene blue (C₁₆H₁₈N₃SCl), the heterocyclic compound is a

ubiquitous organic dye that may cause various adverse effects like eye burn, vomiting, breathing difficulty, chest pain, hemolysis, and mental confusion,¹¹⁴⁻¹¹⁵. So various research works are focused on the heterogeneous photocatalytic degradation of methylene blue¹¹⁶⁻¹¹⁸. TiO₂ seems to be an effective photocatalyst for the degradation of textile dyes¹¹⁹⁻¹²¹.

1.8.2 Drug degradation

The presence of pharmaceutical products in the water stream is a major threat to the ecosystem¹²²⁻¹²³. Antibiotics are released enormously from various sources like pharmaceutical companies, hospital sewages, excretion of human and domestic animals into the ground and surface water¹²⁴. The presence of antibiotics in water results in the development of antibiotic-resistant bacteria. Such a situation is a major threat to mankind and animals which are the finest natural treasures of this planet. As seen earlier, the advanced oxidative process is the most efficient degradation process among the various physical, biological, and chemical treatment methods as it leads to the complete mineralization of the antibiotics. Herein heterogeneous photocatalysis is adopted for the degradation of the antibiotic cefixime. The third degeneration cephalosporin antibiotic cefixime, belonging to the β lactam family of antibiotic is used to treat various diseases related to the urinary tract, respiratory tract, and skin infections¹²⁵.

1.8.3 Water splitting

Fossil fuels, the major energy suppliers of mankind are being depleted for the past few centuries because of their continuous usage and nonrenewable nature¹²⁶. Total dependence on fossil fuel has raised the concern regarding environmental sustainability and modern-day energy production¹²⁷. This creates the necessity for the replacement of fossil fuels by another energy source. The entire world has to think positively about how it meets its energy needs and to find ways to reduce the release of "greenhouse gases" caused by the use of fossil fuels. H₂ can be considered as the best alternative for energy production due to the characteristics like¹²⁸ (1) Clean energy source, (2) Ease of storage, (3) Absence of pollutants, and global warming, (4) Renewable source, and (5) Nontoxicity. Hydrogen can be considered as environmental benign and sustainable source of energy. The inexhaustible energy i.e., solar energy can be utilized for the conversion of water into hydrogen through heterogeneous photocatalysis. Thus, sunlight serves to be renewable, and clean energy source that can produce H₂ without causing any adverse effect to the ecosystem and will create energy security to the world¹²⁹. TiO₂ seems to be an efficient photocatalyst for water splitting reaction¹³⁰. Different modifications of TiO₂ i.e., doping, adding sacrificial agents, dye sensitization, etc. were adopted for increasing the efficiency of photocatalysis¹³¹. Various factors like stability, ecofriendly nature, low cost, and non-corrosive nature favors TiO₂ over the other semiconducting photocatalysts¹³¹⁻¹³².

1.9 Objectives

The overall objective of the present research was

1. To develop efficient photocatalytic systems for various applications
2. To synthesize different photocatalysts like mesoporous TiO₂, mesoporous TiO₂/RuO₂, mesoporous TiO₂/RuO₂/CuO, TiO₂, TiO₂/ZnO, TiO₂/ZnO/Fe₂O₃, mesoporous SrTiO₃, nonporous SrTiO₃ using synthetic strategies like sol-gel method and sol-gel combustion methods
3. To characterize the above mentioned semiconducting photocatalysts
3. To investigate the efficiency of semiconducting photocatalysts by the degradation of the dye methylene blue via photocatalysis
4. To generate H₂ by undergoing visible-light-driven heterogeneous photocatalysis
5. To undergo water purification so as to eliminate the accumulation of antibiotic cefixime that may result in the production of antibiotic-resistant bacteria by sunlight assisted heterogeneous photocatalysis
6. To compare the effect of structure-directing agent on the photocatalytic degradation of methylene blue

1.10 Overview of the experimental work

We have included the experimental methods, characterization techniques used, and results and discussion in chapters 2-9. The experimental methods that we have adopted for our research work were described in chapter 2. The preparation, characterization, and photocatalytic studies of mesoporous binary system $\text{TiO}_2/\text{RuO}_2$ have been illustrated in chapter 3. Methylene blue was chosen as a model for photocatalytic experiments. All the experiments were conducted under sunlight irradiation. In chapter 4, we have demonstrated the synthesis and characterization of mesoporous $\text{TiO}_2/\text{RuO}_2/\text{CuO}$. We have presented a detailed study of H_2 evolution via photocatalytic water splitting using mesoporous $\text{TiO}_2/\text{RuO}_2/\text{CuO}$ in chapter 5. Its photocatalytic activity was investigated and compared with mesoporous $\text{TiO}_2/\text{RuO}_2$ and mesoporous TiO_2 . Sunlight-assisted photocatalytic degradation of cefixime using the photocatalyst mesoporous $\text{TiO}_2/\text{RuO}_2/\text{CuO}$ was presented in the chapter. We have also performed photocatalytic studies by varying the various parameters like catalyst weight, the concentration of CuO, different catalysts, etc. In chapter 7, preparation, the characterization and photocatalytic application of $\text{TiO}_2/\text{ZnO}/\text{Fe}_2\text{O}_3$ were explained. The sol-gel method was used for the synthetic process. In chapter 8 synthesis, characterization, and photocatalytic application of strontium titanate in the presence and absence of structure-directing agent was illustrated. A facile sol-gel combustion method was adopted for the synthetic strategy. The photocatalytic performance was evaluated on the basis of the degradation of the dye methylene blue.

REFERENCES

1. Zhao J, Chen, C. C, Wanhong M, Topics in Catalysis, 2005, 35, 3–4
2. Brillas E, Journal of the Brazilian Chemical Society, 2014, doi.org/10.5935/0103-5053.20130257
3. Chatterjee D, Dasgupta S, Journal of Photochemistry and Photobiology C: Photochemistry Reviews, 2005, 6, 186–205
4. Zangeneh H, Zinatizadeh A.A.L, Habibi M, Akia M, Isa M.H, 2014, doi.org/10.1016/j.jiec.2014.10.043
5. Wang C.C, Jian-Rong Li J.R, Lv X.L, Zhang Y.Q, Guo G, Energy Environ. Sci., 2014, 7, 2831-2867
6. Silva, J.P.A, Carneiro L.M., Roberto I.C, Biotechnology Biofuels, 2012, doi.org/10.1186/1754-6834-6-23
7. Asghar A, Raman A.A.A, Daud, W.M.A.W, Journal of Cleaner Production, 2015, 87, 826-838
8. Stasinakis A.S, Global NEST Journal, 2008, 10, 376-385
9. Ong C.B, Ng L.Y, A W Mohammad, Renewable and Sustainable Energy Reviews 81, 2018, 536–551
10. Chong M.N, Jin B, Chow C.W.K, Saint C, Water Research, 2010, 44, 2997-3027
11. Ahmed S, Rasul M.G, Martens W.N, Water Air Soil Pollut, 2011, 215, 3–29
12. Aziz N. A. A, Palaniandy P, Aziz H.A, Dahlan I, journal of chemical research, 2016, 40, 704–712
13. Hoffmann M.R, Martin S.T, Choi W, Bahnemann D.W, Chem. Rev. 1995, 95, 69-96
14. Cheng Y.W, Chan R.C.Y, Wong P.K, Water Res, 2007, 41, 842
15. Ksibi. M, Rossignol S, Tatibouet J.M, Trapalis C, Mater. Lett., 2008, 62, 4204

16. Yu J. G, Xiong J.F, Cheng B and Liu S.W, *Appl. Catal., B*, 2005, 60, 211
17. Ng Y.H, Iwase A, Bell N.J, Kudo A, and Amal R, *Catal. Today*, 2011, 164, 353
18. A Mills A, S L Hunte, *Journal of Photochemistry and Photobiology A: Chemistry*, 1997, 108, 1-35
19. Shkrob I.A, Sauer Jr M.C, *J. Phys. Chem. B*, 2004, 108, 12497-12511
20. Cao S, Yua J, *Journal of Photochemistry and Photobiology C: Photochemistry, Reviews*, 2016, 27, 72–99
21. Mosquera A, Albella J, Navarro V, 2016, doi.org/10.1038/srep32171
22. Reyes-Coronado D, Rodriguez-Gattorno G, Espinosa-Pesqueira M.E, Cab C, Coss R and Oskam G, *Nanotechnology*, 2008, 19 145605
23. Matsui M, Akaogi M, *Molecular Simulation*, 2006, 6, 239-244
24. Oi L E, Choo M Y, Lee H. V, Ong H. C, Hamida S.B.A, Juan J.C, *RSC Adv*, 2016, 6, 108741 –108754
25. Zhang J, Zhou P, Liu J, Yu J, *Phys. Chem. Chem. Phys.*, 2014, 16, 20382
26. Huang Z, Maness P.C, Blake D.M, Wolfrum E J, Smolinskia S.L, Jacoby W.A, *Journal of Photochemistry and Photobiology A: Chemistry*, 130, 2000, 163-170
27. Mohamad M, Haq B.U, Ahmed R, Shaari A, Alia N, Hussain R, *Materials Science in Semiconductor Processing*, 2015, 31, 405–414
28. Moma J, Baloyi J, 2018, DOI: 10.5772/intechopen.79374
29. Pawar M, Sendogdular S.T, Gouma P, 2018, doi.org/10.1155/2018/5953609
30. Dozzi M.V, Selli E, *Journal of Photochemistry and Photobiology C: Photochemistry Reviews*, 2013, 14, 13-28

31. Xagas A, P, Bernard M.C, Hugot-Le Goff Spyrellis A.N, Loizos Z, Falaras P, *Journal of Photochemistry and Photobiology A: Chemistry*, 2000, 132, 115–120
32. Keller V, F Garin, *Catalysis Communications*, 2003, 4, 377-383
33. Galinska A, Walendziewski J, *Energy Fuels* , 2005, 19, 1143-1147
34. Vandana P, Mohan R and Rini P, *Reviews on Advanced Materials Science* 2018, 5, 119, 130
35. Wang Z.L, *J. Phys.: Condens. Matter* , 2004, 16, 829
36. Banerjee D, Lao J.Y, Wang D.Z, Huang J.Y, Ren Z.F, Steeves D, Kimball B, Sennett M, *Appl. Phys. Lett.*, 2003, 83, 2061–2063
37. Wahab R, Ansari S.G, Kim Y.S, Seo H.K, Shin H.S, *Appl. Surf. Sci.* 2007, 253, 7622–7626
38. Kong X, Ding Y, Yang R, Wang Z.L, *Science*, 2004, 303, 1348–1351
39. Pan Z.W, Dai Z.R, Wang Z, *Science*, 2001, 291, 1947–1949
40. Wu J.J, Liu S.C, Wu C.T, Chen K.H, Chen L.C, *Appl. Phys. Lett.* 2002, 81, 1312–1314
41. Huang Y, He J, Zhang Y, Dai Y, Gu Y, Wang S, Zhou C, *J. Mater. Sci.* 2006, 41, 3057–3062
42. Nikoobakht B, Wang X, Herzing A, Shi J, *Chem. Soc. Rev.* 2013, 42, 342–365
43. Xu T, Ji P, He M, Li J. G, *Nanomater.*, 2012, Doi: 10.1155/2012/797935
44. Chiu W.S, Khiew P.S, Cloke M, Isa D, Tan T.K, Radiman S, Abd-Shukor R, Abd-Hamid M.A, Huang N.M, Lim H.N, *Chem. Eng. J.* 2010, 158, 345–352
45. Jose-Yacamán M, Gutierrez-Wing C, Miki M, Yang D.Q, Piyakis K.N, Sacher E, *J. Phys. Chem. B.* 2005, 109, 9703–9711
46. Polshettiwar V, Baruwati B, Varma R.S, *ACS Nano.* 2009, 3, 728–736

47. Xie Q, Dai Z., Liang J, Xu L, Yu W, Qian Y, *Solid State Commun*, 2005, 136, 304–307
48. Liu J, Huang X, Li Y, Sulieman K.M, Sun F, He X, *Scr. Mater.*, 2006, 55, 795–798
49. Keldysh L.V, *Contemporary Physics*, 2006, 27, 395-428
50. Kołodziejczak-Radzimska A, Jesionowski T, *Materials* 2014, 7, 2833-2881
51. Chu S, Wang G, Zhou W, *Nature Nanotechnology*, 2011, 6, 506–510
52. Na J.H, Kitamura M, Arita M, and Arakawa Y, *Applied Physics Letters*, 2009, 95, 253303
53. Sudhagar P, Kumar R.S, Jung J.H, *Materials Research Bulletin*, 2011, 46, 1473–1479
54. Wang Z.L, Yang R, Zhou J, *Materials Science and Engineering R*, 2010, 70, 320–329,
55. Xu J, Han J, Zhang Y, Sun Y, Xie B, *Sensors and Actuators*, 2008, 132, 334–339,
56. Lu Y, Chang S.J, Chang S.P, *Applied Physics Letters*, 2006, 89, 153101
57. Cho S, Kim S, Jang J.W, *Journal of Physical Chemistry C*, 2009, 113, 10452–10458
58. Canu G, Buscaglia V, *Cryst Eng Comm*, 2017, 19, 3867-3891
59. Neville R.C, Hoeneisen B, Mead C.A, *Journal of Applied Physics*, 1972, 43, 2124
60. Deak D.S, *Materials Science and Technology*, 2007, 23, 2127
61. Cowley R A, *Phil. Trans. R. Soc. A*.1996, 354, 2799–2814
62. Ura B, Trawczynski J, Kotarb A, Bieniasz W, Illan-Gomez M.J, Bueno-Lopez A, Lopez-Suarez F.E, *Applied Catalysis B: Environmental*, 2011, 101, 169–175
63. Ohta H, *Materials Today*, 2007, 10, 44-49

64. Enhancing photocatalysis with strontium titanate, *Advanced Science News, Micro-/Nanotechnology*, 2014
65. Phoon B.L, Lai C.W, Juan J C, Show P.L, Pan G.T, *international journal of hydrogen energy*, 2019, 44, 14316-14340
66. Xie T, Wang Y, Liu C, Xu L , 2018, 11, 646
67. Ha M.N, Feng Zhu, Liu Z, Wang L, Liu L, Lu G, Zhao Z, *RSC Adv.*, 2016, 6, 21111
68. Srdic V.V, Djenadic R.R, *J. Optoelectronic, Adv. Mater.*, 2005, 7, 3005-3013
69. Tomar A.K, G Singh, R. K Sharma, *Journal of Power Sources* 2019, 426, 223-232
70. Wrighton M.S, Ellis A.B, Wolczanski P.T, Morse D.L, Abrahamson H.M, Ginley D.S, *Journal of the American Chemical Society*, 1976, 10, 2774-2779
71. Karimi L, Zohoori S, Yazdanshenas M, *Journal of Saudi Chemical Society*, 2014, 18, 581-588
72. Shi J, Shen S, Chen Y, Guo L, Mao S.S, 2012, 20, 351-359
73. M. L. Green, *J. Electrochem. Soc.* 1985, 132, 2677
74. Herbert Over, *Chem. Rev.* 2012, 112, 3356-3359
75. McKeown D.M, Hagans P.L, Carette L.P.L, Russell A.E, Swider, K.E, Rolison D.R, *J. Phys. Chem. B* 1999, 103, 4825-4832
76. Rossi L.M., *Journal of the Brazilian Chemical Society*, 2004, 15, 901-910.
77. Neupane S, Kaganas G, Valenzuela R, *J Mater Sci*, 2011, 46, 4803–4811
78. Qu J, Zhang X, Wang Y, Xie C, *J. Electrochimica Acta*, 2005, 50, 3576–3580
79. MajumdarD, MaiyalaganT, Jiang Z, *Chem Electro Chem* 2019, 6, 4343-4372

80. Rossi L.M, Machado G, Fichtner P.F.P, Teixeir S.R, Dupont J, Catalysis Letters , 2004, 92, 3–4
81. Debecker D.P, Farin B, Gaigneaux E.M, Sanchez C, Sassoey C, Applied Catalysis A: General, 2014, 481, 11–18
82. Park BO, Lokhande C.D, Park HS, Journal of Materials Science, 2004, 39, 4313–4317
83. Chen D.H, He X.R, Materials Research Bulletin, 2001, 36, 1369-1377
84. Zak A.K, Abrishami M.E, Majid W.H.A, Yousefi R, Hosseini S.M, Ceramics International, 2011, 37, 393-398,
85. Zhang W, Yanga Z, Liu Y, Tang S, Han X, Chen M, Journal of Crystal Growth, 2004, 263, 394–399
86. Verma S, Joy P.A, Kholam Y.B, Potdar H.S, Deshpande S.B, Materials Letters 2004, 58, 1092–109
87. Barron A.R and Rees Jr W.S, advanced materials for optics and electronics, 1993, 2, 271-288
88. Mirzaeia A, Neri G, Sensors and Actuators B Chemical, 2016, 237, 749-775
89. Esposito S, Materials, 2019, 12, 668
90. Rao B.G, Reddy B.R, 2017, 1, 1-3
91. Tseng T.K, Lin Y.S, Chen Y.J, Chu H, Int., J. Mol. Sci. 2010, 11, 2336-2361
92. Shi L, Zeng C, Jin Y, Wang T, Tsubaki N, Catal. Sci. Technol., 2012, 2, 2569-2577
93. Jain S.R, Adiga K.C, Verneker V.R.P, Combust. Flame, 1981, 40, 71
94. Bhagwat V.R, Humbe A.V, More S.D, Jadhav K.M, Materials Science & Engineering B, 2019, 248, 114388
95. Butkute S, Gaigalas E, Beganskiene A, Ivanauskas F, Ramanauskas R, Kareiva A, journal of Alloys and Compounds, 2018, 739, 504-509,

96. Kumar A, Yadav Bhatt M, Mishra N.K, Chaudhary P, Singh
Research Journal of Chemical Sciences, 2015, 5, 98-105
97. Shen S, Kronawitter C, Kiriakidis G, Journal of Materiomics, 2017, 3,
1-2,
98. Neațu S, Agullo J.A.M, Garcia H, Int. J. Mol. Sci., 2014, 15, 5246-
5262
99. Ibhaddon A.O, Fitzpatrick P, Catalysts, 2013, 3, 189-218
100. Medynska A.Z, Recent Patents on Engineering, 2008, 2, 157-164
101. Vinu A, Mori T, Ariga K, Science and Technology of Advanced
Materials, 2006, 7, 753–771,
102. Ismail A.A, Bahnemann D.W, journal of Materials Chemistry, 2011,
21, 11686
103. Zhang R, Elzatahry A.A, Al-Deyab S.S, Zhao D, Nano Today, 2012
7, 344-366
104. Mgwetyan U, Makhath M.E, Mamo M, Ndungu P, ScienceDirect
Materials Today: Proceedings, 2018, 5, 10585–10591
105. Marien C.B.D, Marchal C, Koch A, Robert D, Drogui P, Environ Sci
Pollut Res Int., 2017, 14, 12582-12588
106. Feng P, Bu X, Pine D.J, Langmuir, 2000, 16, 5304-5310
107. Di Paola A, Palmisano L, Venezia A.M, Augugliaro V, J. Phys.
Chem. B 1999, 103, 8236-8244
108. Humayun M, Raziq F, Khan A, Luo W, Green Chemistry Letters and
Reviews, 2018, 11, 86-102
109. Sima J, Hasal P, Chemical engineering transactions, 2013, 32, 79-84
110. Rochkind M, Pasternak S, Paz Y, Molecules 2015, 20, 88-110
111. Akpan U.G, Hameed B.H, Journal of Hazardous Materials, 2009,
170, 520–529
112. Konstantinou I. K, Albanis T.A, Applied Catalysis B: Environmental,
2004, 49, 1–14
113. Zangeneh H, Zinatizadeh A.A.L, Habibi M, Akia M, Isa M.H,
journal of Industrial and Engineering Chemistry, 2015, 26, 1-36,

114. Rafatullaha M, Sulaiman O, Hashima R, Ahmad A, *Journal of Hazardous Materials*, 2010, 177, 70–80
115. Jing H.P, Wang C.C, Zhang Y.W, Wang P, Lia R, *RSC Advances*, 2014, 4, 54454-54462
116. Tuyen L.T.T, Quang D.A, Toan T.T.T, Tung T.Q, Ho T.T, Mau T.X, KhieuD.Q, *Journal of Environmental Chemical Engineering*, 2018, 6, 5999–6011
117. Tayade R.J, Natarajan T.S, Bajaj H.C, *Ind. Eng. Chem. Res.* 2009, 48, 10262–10267
118. Chithambararaj A, Sanjini N. S, Velmathi S, Chandra Bose A: *Phys. Chem. Chem. Phys.*, 2013, 15, 14761-14769
119. Neppolian B, Choi H.C, Sakthivel S, Arabindoo B, Murugesan V, *Chemosphere* 2002, 46, 1173–1181
120. Malagutti A.R, Mourao H.A.J.L, Garbin J.R, Ribeiro *Applied Catalysis B: Environmental*, 2009, 90, 205–212
121. Prieto O, Feroso J, Nunez Y, Del Valle J.L, Irusta R, *Solar Energy*, 2005, 79, 376-383
122. ChatzitakisA, Berberidou C, Papalists I, Kyriakou G, Sklaviadis T, Poulis I, *Water Research*, 2008, 42, 386-394,
123. El-KemaryM, El-ShamyH, El-MehasselI, *journalof Luminescence*, 2010, 130, 2327-2331
124. Elmolla E.S, Chaudhuri M, *Desalination* 252 , 2010, 46–52
125. PamudjiJ.S, MauludinR, Nurhabibah, *ProcediaChemistry*, 2014, 13, 119-127
126. Li Y, Peng Y, Hu L. *Nat Commun*, 2019, 10, 4421
127. Hisatomi, T, Domen, K., *Nat Catal*, 2019, 2, 387–399
128. Fajrina N, Tahir M, *International Journal of Hydrogen Energy*, 2019, 44, 540-577
129. Acar C, Dincer I, Naterer G.F, *Int. J. Energy Res.*, 2016, 40, 1449-1473
130. Fan Y, Li D, Deng M, Luo Y, *Chem. China*, 2009, 4, 343–351
131. Miyoshi A, Nishioka S, and Maeda K, 24, 2018, 18204-18219
132. Ni M, Leung M.K.H, Leung D.Y.C, Sumathy K, *Renewable and Sustainable Energy Reviews*, 2007, 11, 401–425

CHAPTER 2

EXPERIMENTAL METHODS AND CHARACTERIZATION TECHNIQUES

Contents

- 2.1 Introduction
 - 2.2 Analytical techniques
 - 2.3 General description of methods adapted for synthesis of mixed, binary and ternary metal oxide nanosystem
 - 2.3.1 Synthesis of mesoporous $\text{TiO}_2/\text{RuO}_2/\text{CuO}$, mesoporous $\text{TiO}_2/\text{RuO}_2$ and mesoporous TiO_2 nanosystem
 - 2.3.2 Synthesis of TiO_2 , TiO_2/ZnO and $\text{TiO}_2/\text{ZnO}/\text{Fe}_2\text{O}_3$ nanocomposite
 - 2.3.3 Synthesis of MSTO and STO
 - 2.4 Procedure of methods adapted for the catalytic studies done using mixed, binary and ternary metal oxide nanosystem
 - 2.4.1 Photocatalytic dye degradation studies under sunlight irradiation using $\text{TiO}_2/\text{RuO}_2$ binary nanosystem
 - 2.4.2 Photocatalytic water splitting studies using mesoporous $\text{TiO}_2/\text{RuO}_2/\text{CuO}$ ternary nanosystem
 - 2.4.3 Photocatalytic drug degradation studies using $\text{TiO}_2/\text{RuO}_2/\text{CuO}$ ternary nanosystem
 - 2.4.4 Photocatalytic methylene blue degradation studies using $\text{TiO}_2/\text{ZnO}/\text{Fe}_2\text{O}_3$ nanocomposite under UV and sunlight irradiation
 - 2.4.5 Photocatalytic methylene blue degradation studies using MSTO under UV irradiation
 - 2.5 Characterization techniques
 - 2.5.1 UV-Visible Spectroscopy
 - 2.5.2 FTIR Spectroscopy
 - 2.5.3 X-ray Diffraction (XRD)
 - 2.5.4 Surface Area Measurements
 - 2.5.5 X-ray Photoelectron Spectroscopy (XPS)
 - 2.5.6 Scanning Electron Microscopy (SEM)
 - 2.5.7 Transmission Electron Microscopy (TEM)
 - 2.5.8 Photoluminescence Spectroscopy (PL)
 - 2.5.9 Gas Chromatography
 - 2.5.10 Total Organic Carbon analyzer
-

2.1 Introduction

This chapter demonstrates the synthetic strategies adopted for the preparation of mesoporous $\text{TiO}_2/\text{RuO}_2$, mesoporous $\text{TiO}_2/\text{RuO}_2/\text{CuO}$, $\text{TiO}_2/\text{ZnO}/\text{Fe}_2\text{O}_3$, and mesoporous SrTiO_3 and the characterization techniques used. In the first part of this chapter, we have demonstrated the procedures of the synthesis of mesoporous $\text{TiO}_2/\text{RuO}_2/\text{CuO}$, mesoporous $\text{TiO}_2/\text{RuO}_2$, $\text{TiO}_2/\text{ZnO}/\text{Fe}_2\text{O}_3$, and mesoporous SrTiO_3 via the sol-gel method and sol-gel combustion method. The methodology for the various photocatalytic applications like water splitting, dye degradation, and drug degradation has been explained in the preceding sections. The last section deals with the explanation of characterization techniques used in our research work. The list of chemicals used for this research work is given in Table 2.1. All the chemicals were of analytical grade and used without any purification. Deionized water was used throughout the research work.

2.2 Analytical techniques

To have a better understanding of morphology, nature, and structure of the photocatalysts, various characterizations like UV-Vis diffuse reflectance spectroscopy, FTIR spectroscopy, X-ray diffraction (XRD), X-ray photoelectron spectroscopy (XPS), Surface area measurements, Scanning electron microscopy (SEM), Transmission electron microscopy (TEM), Photoluminescence spectroscopy (PL) measurements were employed. The photocatalytic degradation was confirmed through Ultraviolet-Visible absorption spectroscopy and

Total organic carbon analyzer. The H₂ evolution experiments were monitored using Gas chromatography.

Table, 2.1 List of chemicals used and suppliers

Sl. No	Name of chemicals	Name of manufacturer
1.	Titanium(IV)tetraisopropoxide (TTIP)	Sigma Aldrich
2.	Ruthenium (IV) nitrosyl nitrate (Ru(NO)(NO ₃) ₃)	Sigma Aldrich
3.	Pluronic P123	Sigma Aldrich
4.	Copper (II) nitrate	Sigma Aldrich
5.	Acetic acid	Merck
6.	Concentrated nitric acid	Merck
7.	Ethanol	Merck
8.	Tetrabutyl titanate (TBOT)	Sigma Aldrich
9.	Zinc nitrate	Sigma Aldrich
10.	Ferric nitrate	Sigma Aldrich
11.	Ethylene glycol	Merck
12.	Citric acid	Merck
13.	Strontium nitrate	Merck

2.3 General description of methods adopted for the synthesis of mixed, binary, and ternary metal oxides nanosystem

The synthetic strategy adapted for the preparation of various catalyst for the present study is provided in this section.

2.3.1 Synthesis of mesoporous TiO₂/RuO₂/CuO, mesoporous TiO₂/RuO₂, and mesoporous TiO₂ nanosystem

One step pluronic P123 assisted sol-gel process was used to synthesize mesoporous TiO₂/ RuO₂ and TiO₂/RuO₂/CuO nanomaterials. About

3.2 g of the triblock copolymer pluronic P123, 4.6 mL of CH₃COOH and 1.5 mL of HNO₃ were dissolved in 30 mL of ethanol in a 200 mL beaker. About 5.8 mL of titanium (IV) tetra isopropoxide was added slowly to the above mixture and stirred for 10 minutes. Calculated amount of ruthenium (IV) nitrosyl nitrate was added to the above mixture and the mixture was stirred vigorously for 30 minutes. About 0.0074, 0.0149, 0.0747 and 0.1497 g of CuNO₃ were dissolved in 10 mL of ethanol and were added to the above solution followed by continuous stirring for 2.5 hours to obtain mesoporous TiO₂/RuO₂/CuO 0.05, 0.1, 0.5 and 1 % respectively. The obtained materials were kept for 12 hours for drying at room temperature. Then these were transferred into an oven maintained at 65 °C and aged for an additional 24 hours. Finally, the materials were calcined at 500 °C for 5 hours. The obtained materials were labeled as mesoporous TiO₂/RuO₂/CuO. The same procedure was repeated in the absence of CuNO₃ and Ru(NO)(NO₃)₃ to obtain mesoporous TiO₂/RuO₂ nanomaterial and mesoporous TiO₂ respectively

2.3.2 Synthesis of TiO₂, TiO₂/ZnO and TiO₂/ZnO/Fe₂O₃ nanocomposite

12.9 mL TBOT was initially dissolved in 51.1 mL absolute ethanol under vigorous stirring and 8.7 mL acetic acid, 0.66 mL water, and 12.9 mL ethanol were added slowly until a yellow transparent solution was formed. Secondly, in a mixed solution of 20 mL absolute ethanol, 6.5 mL acetic acid, and 2.5 mL deionized water; Zn(NO₃)₂·6H₂O and Fe(NO₃)₃·9H₂O were added in required amounts. This second solution was mixed with the first solution dropwise with vigorous stirring at

least for two hours. After aging this for 48 hours, the prepared sol was dried at 100 °C for 12 hours and then calcined at 500 °C for 5 hours in a microwave muffle furnace to obtain the end product. The same method was repeated for the synthesis of TiO₂ and TiO₂/ZnO in the absence of Zn(NO₃).6H₂O, Fe(NO)₃.9H₂O, and Fe(NO)₃.9H₂O, respectively.

2.3.3 Synthesis of MSTO and STO

For the synthesis of MSTO, about 0.2 g of pluronic P123 was dissolved in 60 mL ethanol and stirred for 2 hours. 6.5 mL titanium isopropoxide solution was added to the above reaction mixture followed by the addition of 6.7 mL ethylene glycol, and 6.6 mL water. The resulting solution was stirred continuously for 2 hours. About 35 mL 6.3 g citric acid was added dropwise with stirring to the above solution and stirred for 10 minutes. This was followed by the addition of 25 mL of 4.23 g Sr (NO₃)₂, refluxed for 4 hours at 80 °C and kept in the oven at 100 °C for 24 hours to obtain the dried gel. It was followed by calcination in a closed crucible at 800 °C for 3 hours in a muffle furnace. The obtained material was labeled as mesoporous SrTiO₃ (MSTO). The same procedure was repeated in the absence of pluronic P123 to obtain STO.

2.4 Procedure of methods adapted for the catalytic studies done using mixed, binary, and ternary metal oxide nanosystem

2.4.1 Photocatalytic dye degradation studies under sunlight irradiation using TiO₂/RuO₂ binary nanosystem

Photocatalytic activities of synthesized samples were evaluated by the degradation of methylene blue dye (MB) in sunlight. About 0.005 g of

the photocatalyst dissolved in 100 mL of 10^{-5} M aqueous solution of methylene blue was taken in a beaker and stirred for 30 minutes to maintain the adsorption-desorption equilibrium. After that, the solution was exposed to direct sunlight. At an interval of 20 minutes, 5 mL of the solution was withdrawn, centrifuged for 20 minutes at 3500 rpm. Moreover, the absorbance was measured using JASCO Spectrofluorometer (FP-8300) in the wavelength range of 200 to 800 nm. We carried out the experiments on sunny days to assure the maximum availability of sunlight. The intensity of sunlight at an interval of five minutes was measured using LUXMETER (LX-103).

2.4.2 Photocatalytic water splitting studies using mesoporous TiO₂/RuO₂/CuO ternary nanosystem

The photocatalytic reaction was carried out at room temperature in an air-tight quartz cell of 70 mL capacity which was closed with a silicone rubber septum. The catalyst was sonicated initially for 15 minutes. Typically, 5 mg of the photocatalyst was dispersed in 5 mL methanol (methanol acts as a sacrificial reagent) and 20 mL water by magnetic stirrer in an air-tight quartz cell. A high-pressure 450 W Hg lamp was used as a light source for irradiation covered with water circulating Pyrex jackets. The amount of H₂ evolved was determined using gas chromatography (5700 Nucon gas chromatograph with carboxsphere column and Ar as carrier gas) with a thermal conductivity detector. The program used in GC for all the analyses involved the detector temperature of 100 °C and oven temperature of 50 °C at the time of injection. A gas-phase syringe (injection volume of 500 µL) was used to inject the sample periodically at the headspace of the

reactor. The experiment was carried out for six hours. Photocatalytic studies were performed by varying the parameters like catalyst weight, the concentration of Cu, amount of sacrificial agent, varying the chain length of the sacrificial agent, and using different sacrificial agents. We have also done the experiment to evaluate the effect of recycling the catalyst by taking 5 mg of mesoporous TiO₂/RuO₂/CuO 1%, keeping all other parameters constant for 6 hours. Photocatalytic water splitting experiments were performed continuously for 18 hours using 25 mg of mesoporous TiO₂/RuO₂/CuO 1%. TEM and XPS analysis were performed before and after the water splitting reaction to evaluate the morphological and surface characteristics of the photocatalyst.

2.4.3 Photocatalytic drug degradation studies using TiO₂/RuO₂/CuO ternary nanosystem

The degradation studies were performed by adding 0.0125 g of TiO₂/RuO₂/CuO in 100 mL of desired concentration of cefixime. The reaction mixture was taken in a beaker and stirred in the dark to eliminate the errors due to adsorption taking place in the catalyst. After that, the beaker was placed in direct sunlight for 60 minutes with constant stirring. 5 mL aliquots were withdrawn at a specific time interval and centrifuged for 30 minutes at 3600 rpm to avoid the effect of scattering prior to measurement of photocatalytic activity. Subsequently, we determined the decrease in the concentration of cefixime by measuring the absorbance of cefixime at 287.5 nm using JASCO Spectrofluorometer (FP-8300). All the photocatalytic degradation experiments were carried out on sunny days to ensure maximum availability of sunlight. We have investigated the

optimization of various parameters like catalyst concentration, the concentration of the antibiotic, the effect of time, the effect of catalyst loading, etc. We calculated the efficiency of the experiment using the equation,

$$\text{Degradation}\% = (C_0 - C_t) / C_0 \times 100,$$

Where C_0 and C_t represent the concentration of cefixime at irradiation time 0 and t, respectively. Degradation % represents the efficiency of degradation of cefixime. We conducted the following experiments to study the effect of various parameters on the mineralization of the antibiotic cefixime under solar irradiation.

2.4.4 Photocatalytic methylene blue degradation studies using $\text{TiO}_2/\text{ZnO}/\text{Fe}_2\text{O}_3$ nanocomposite under UV and sunlight irradiation

About 50 mL of prepared standard methylene blue with the concentration of 10^{-4} M and 0.2 g of calcined photocatalyst (TiO_2 , TiO_2/ZnO , and $\text{TiO}_2/\text{ZnO}/\text{Fe}_2\text{O}_3$) was added to the dye solution and stirred in the dark in a UV reactor for 30 minutes to maintain the adsorption-desorption equilibrium. This was followed by the performance of reaction in the presence of UV light. The photocatalytic reaction was carried out in LZC-4X- Luzchem photo reactor provided with a bead. The reaction was monitored by withdrawing 3 mL aliquots at an interval of 20 minutes. After degradation, the solution was centrifuged to eliminate the effects of scattering before the evaluation of the photocatalytic activity. The same experiment was conducted in direct sunlight with the most active

catalyst. The intensity of sunlight at an interval of five minutes was measured using LUXMETER (LX-103).

2.4.5 Photocatalytic methylene blue degradation studies using MSTO under UV irradiation

In order to study the photocatalytic efficiencies of the MSTO and STO materials, photocatalytic degradation studies were conducted on a photoreactor of model LZC-4X-Luzchem photoreactor with UV light intensity 600 lux. About 0.2 g of the catalyst was added to 50 mL methylene blue at a concentration of 1×10^{-4} M taken in a beaker. The solution was stirred for 30 minutes in the UV reactor in the absence of light to maintain the adsorption-desorption equilibrium. After that, the reaction was performed in the presence of UV light. The photocatalytic reaction was performed in the photoreactor of model LZC-4X-Luzchem photoreactor with UV light intensity 600 lux. The reaction was monitored by withdrawing 3 mL aliquots at an interval of 20 minutes. The solution was centrifuged to eliminate the effects of scattering prior to record the absorption spectra.

2.5 Characterization techniques

2.5.1 UV-Visible spectroscopy¹

UV-Visible spectroscopy is a quantitative technique that measures the absorption of light by molecules induced by electronic excitation. The light absorbed can be determined by measuring the intensity of light passing through the sample with respect to the intensity of light through the reference sample. An optical spectrometer is used to

measure the wavelength of that particular absorption. The plot of absorption against wavelength provides the absorption spectrum. The working of UV-Visible spectroscopy is based on the principle of Beer Lambert's law. According to Beer-Lambert's law, the absorbance of a solution is directly proportional to the concentration of the absorbing species in the solution and the path length of the medium. It can be mathematically represented as $A = \epsilon c l$. In the case of solid samples, diffuse reflectance spectroscopic accessories are attached separately. The band gaps of the semiconductors are estimated using Kubelka Munk Plots. UV-Visible spectroscopy provides qualitative and quantitative information of the sample.

Here A is the absorbance, ϵ is the molar absorptivity is the concentration, and l is the path length of the medium. In our present research work, Jasco-V-550-UV/VIS spectrophotometer was used to measure the optical properties and absorbance spectra of samples.

2.5.2 FTIR spectroscopy²

FTIR spectroscopy is an analytical technique used for the identification of organic and inorganic compounds. The molecule on absorbing light in the infrared region of electromagnetic spectra results in bands corresponding to the bonds in the molecules. Molecule on irradiation with infrared beam results in the excitation of molecules to higher vibrational states. The wavelength of absorbed radiation corresponds to the molecular structure of materials.

FTIR instrument consists of components like an interferometer, sample compartments, detector, and computer. On passing the infrared beam

through the sample a part of the radiation is absorbed and another part is reflected. The interferometer is used to modulate the infrared emission from the source. Usually, the detector measures the intensity of light measured as a function of wavelength. The computer analyses the interferogram obtained from the detector. The resulting FTIR spectrum obtained indicates the molecular absorption and transmission of the sample.

The FTIR spectra of the sample were measured from the Department of Chemistry, University of Calicut. The FTIR spectra of the samples mesoporous SrTiO₃ and nonporous SrTiO₃ were analyzed using Jasco-FT/IR-4100 spectrophotometer in the range 4000-400 cm⁻¹. A sample pellet was prepared by mixing a fixed amount of the sample and spectroscopic grade KBr in a ratio of 1:100.

2.5.3 X-ray Diffraction (XRD)³

X-ray Diffraction (XRD) is an analytical technique used for the determination of crystal structure, chemical composition, and physical properties of the sample under investigation. The X-ray diffractometer consists of three important components namely an X-ray tube, sample holder, and X-ray detector. A monochromatic beam of X-ray of suitable wavelength is allowed to fall on a set of parallel and equidistant planes called lattice planes at a particular angle θ . When the light of suitable wavelength is incident upon crystal lattice, they get diffracted from the lattice points resulting in constructive and destructive interference. This will give rise to suitable diffraction

patterns in the case of constructive interference. W.H Bragg identified a relationship, $n\lambda=2d\sin\theta$.

Where λ is the wavelength of the X-rays used, d is the spacing between the lattice planes, θ is the angle of incidence at which a diffraction peak is measured and n is an integer that indicates the 'harmonic order' of the diffraction. The intensities of the diffracted X-ray beam are plotted against 2θ values.

In our present work, the XRD analysis of all the samples except mesoporous $\text{TiO}_2/\text{RuO}_2$ was performed on a Bruker AXS D8 advance diffractometer using $\text{Cu-K}\alpha$ radiation ($\lambda = 1.5406 \text{ \AA}$) and the measurements were done in the Bragg angle range 20° to 80° . In the case of mesoporous $\text{TiO}_2/\text{RuO}_2$, the diffraction patterns were recorded using Rigaku Miniflex Diffractometer with $\text{CuK}\alpha$ ($\lambda = 1.54 \text{ \AA}$) irradiation available at the Department of Physics, University of Calicut. The diffraction patterns were recorded from 20° to 80° . The spectra obtained were analyzed with the data from the Joint Committee Powder Diffraction Standards (JCPDS).

The crystallite size of the samples was determined using the Scherrer equation.

$$\phi = (0.9\lambda)/\beta\cos\theta$$

Where ϕ = Crystallite size (nm), λ = Wavelength of X-ray (\AA),
 θ = Bragg's angle, β = Full width at half maximum.

2.5.4 Surface Area Measurements⁴

The BET theory was developed by Stephen Brunauer, Paul Emmett, and Edward Teller. In BET the specific surface area of the sample is calculated by physical adsorption of a gas on the surface of the solid sample and by calculating the amount of adsorbate gas corresponding to a monomolecular layer on the surface. The weak forces between the adsorbate and the adsorbent are responsible for the physisorption. The analysis was carried out at the temperature of liquid nitrogen. The pore volume, pore area, and pore distribution can be determined by BJH analysis. The specific surface area can be determined using the BET equation, the equation can be represented as,

$$(P/P_0)/V (1 - P/P_0) = 1/V_m C + (C-1) (P/P_0)/ V_m C$$

Here, V is the volume of gas adsorbed (in cm^3/g) at pressure P . V_m is the volume adsorbed on the surface of the solid is completely covered with a monolayer of adsorbed gas molecules in cm^3/g is a constant depending upon the nature of the gas. Since ‘ C ’ and ‘ V_m ’ are constants for a given gas-solid system, a plot of $P/V(P_0-P)$ vs P/P_0 will give a straight line. Total surface area of the sample can be calculated using the equation,

$$\text{Surface area (S)} = V_m N A / M$$

Here N = Avogadro Number, $6.023 \times 10^{23} \text{ mol}^{-1}$, A is the cross-sectional area of a single molecule of the adsorbate (m^2) and M is the Molecular weight of the adsorbate (g/mol).

BET surface area, pore volume, and pore diameter of the samples in our research work were analyzed by BELSORP-max instrument

2.5.5 X-ray Photoelectron Spectroscopy (XPS)⁵

XPS an electron spectroscopic technique is used to analyze the surface morphology of the samples. Utilizing this instrumentation method, we were able to detect the elemental composition, empirical formula, chemical state, and electronic state of the elements within a material. When a solid surface is irradiated with a beam of X-ray, electrons are emitted. The kinetic energy of the emitted electrons from the top of the surface (0 nm) to 10 nm depth of a surface is measured simultaneously. The resulting photoelectron spectrum consists of a plot of ejected electrons as a function of the kinetic energy. The XPS measurement of the sample mesoporous TiO₂/RuO₂/CuO was done from NCL Pune, using a custom-built ambient pressure XPS system from Prevac and equipped with VG Scienta monochromator (MX650). The energy of the photoelectrons was analyzed using VG Scienta's R3000 HP differentially pumped analyzer. The XPS of the TiO₂/ZnO and mesoporous SrTiO₃ was recorded from Amrita Institute of Science and Technology, Kochi. The instrument used was Axis Ultra, Kratos Analytical, UK with an Al-K α (1486.6 eV) source.

2.5.6 Scanning Electron Microscopy (SEM)⁶

Scanning electron microscope is a nondestructive analytical technique, that produces a magnified image for analysis. In the SEM, a beam of electrons ejected from the source is focused on the specimen surface. The interaction of the incident electrons with the atomic surfaces

results in the generation of secondary electrons, backscattered electrons, and auger electrons that are being detected to form an image. The secondary electrons originating from the surface of the samples provide detailed information on surface morphology, whereas backscattered electrons originating from the deeper regions of the sample provide information regarding the atomic number and phase composition. The information regarding surface atomic composition is obtained from auger electrons.

The FEI, QUANTA 200 3D SEM instrument that was operating at 10, 15, and 20 kV using tungsten filament as electron source was used for SEM imaging of the sample mesoporous TiO₂ /RuO₂/CuO.

2.5.7 Transmission Electron Microscopy (TEM) ⁷

Transmission electron microscope is an analytical technique that provides information regarding topography, morphology, composition, and crystallography of the samples. TEM analysis provides high-resolution 2-dimensional images by utilizing highly energetic electrons. In Transmission electron microscope high-energy beam of electrons are focused on the thin sample. Various features of the sample like crystal structure, dislocations, and grain boundaries can be evaluated by analyzing the interaction between electrons and atoms. The Transmission electron microscope works on the same principle as that of the light microscope. The high magnification power and provision of both image and diffraction information of the sample are the advantages.

In our present research work, FEI Tecnai F30 S-TWIN HR-TEM Transmission electron microscopes with accelerating voltage of 200 kV were used for TEM imaging of the sample mesoporous TiO₂/RuO₂/CuO. JEOL/JEM 2100 Transmission electron microscope was used to obtain the TEM image of TiO₂/ZnO/Fe₂O₃ and mesoporous SrTiO₃.

2.5.8 Photoluminescence Spectroscopy (PL)⁸

Photoluminescence spectroscopy often referred to as PL is a non-destructive method for the study of optical properties of the materials. On illuminating the sample, the light gets absorbed and the sample undergoes photoexcitation. The photo-excitation can be described as the excitation of material to a higher electronic state, and return to a lower energy level with the release of energy. The emission of light or luminescence through this process is photoluminescence. The period between the absorption and emission can either be in the order of 10 nanoseconds or may be extended to minutes or hours. The energy distribution of the materials is measured to analyze the property of materials. In our present work, PL spectra of the sample mesoporous TiO₂/RuO₂/CuO and mesoporous TiO₂/RuO₂ were obtained using JASCO Spectrofluorometer (FP-8300). PL spectra of the samples STO, MSTO, and TiO₂/ZnO/Fe₂O₃ were measured by Perkin Elmer LS 55 PL spectrophotometer.

2.5.9 Gas chromatography⁹

Gas chromatography is an analytical method used to separate and identify various analytes that can be vaporized without decomposition.

Here the components are separated based on their volatility. In Gas chromatography, the carrier gas constitutes the mobile phase, and inert gases like nitrogen and helium are used as the stationary phase. Usually, a very thin layer of polymer or liquid on an inert solid support, inside a metal or glass tube constitutes the column. The sample to be separated is mixed with the mobile phase followed by the injection to the column. The separation occurs between a gas mobile phase and a liquid stationary phase. The sample undergoing separation should be able to vaporize without undergoing thermal decomposition. Finally, the detectors produce the chromatogram by detecting the components present in the chromatogram.

In the present study, the gas analysis was carried out by regular sampling every hour and a gas chromatograph (GC) equipped with a TCD detector (Agilent 7890) was employed for quantitative analysis

2.5.10 Total Organic Carbon Analyser¹⁰

Total organic carbon measurement is used for analyzing the degree of organic molecules or contaminants in water. Total organic carbon analysis usually measures the total carbon (TC), inorganic carbon (IC), total organic carbon (TOC), purgeable organic carbon (POC), and non purgeable organic carbon (NPOC). Sampling, oxidation, and detection are the three main steps involved in the total organic carbon analysis. For satisfying the required regulations, the sampling system must have automatic sampling, acidification, and sparging for TOC analysis, automatic dilution capability, and autocalibration using a single stock standard to improve reproducibility and increase throughput. For

Experimental Methods

determining the TOC, the carbon should be oxidized. Several strategies like photocatalytic oxidation, chemical oxidation, and high-temperature combustion are adopted for the oxidation process. In our research work, TOC analysis was conducted to determine the carbon content in the sample obtained after photocatalytic antibiotic degradation. TOC-L Shimadzu TOC analyzer was used for analyzing the total organic carbon content in the sample.

REFERENCES

1. Williams D.H and Fleming I, Spectroscopic Methods in Organic Chemistry, The McGraw- Hill Companies, UK, 1995
2. Hoffmann F, M, Infrared reflection-absorption spectroscopy of adsorbed molecules, 3, 1983, 3, 107-192
3. X-ray Methods-Analytical Chemistry by Open Learning, John Wiley & Sons, New York, 1987
4. Brunauer S, Emmett P.H and Teller E, J, J. Am. Chem. Soc., 1938, 60, 309
5. Skoog D.A, Holler F.J, and Crouch S.R, Principles of Instrumental Analysis, Thomson Brooks/Cole, USA, 2007
6. Inkson B.J, Materials Characterization Using Nondestructive Evaluation (NDE) Methods, 2016, 17-43
7. Williams D.B, Carter C.B, The Transmission Electron Microscope, Springer, Boston, MA, 1996
8. Timothy H.G Froerer, Encyclopedia of Analytical Chemistry, R.A. Meyers, 2000, 9209–9231
9. Jonathan B and James. M.M, Analytical chemistry in a GMP environment, John Wiley & Sons. Inc., USA, 2000
10. Fung Y.S, Wu Z and Dao K.L, Anal. Chem., 1996, 68, 2186-2190

CHAPTER 3

SUNLIGHT ASSISTED PHOTOCATALYTIC DEGRADATION OF METHYLENE BLUE VIA MESOPOROUS TiO_2 / RuO_2 BINARY NANOSYSTEM

Contents

- 3.1 Introduction*
 - 3.2 Experimental methods*
 - 3.3 Photocatalytic methylene blue degradation studies*
 - 3.4 Results and discussion*
 - 3.4.1 UV-Visible DRS analysis*
 - 3.4.2 XRD analysis*
 - 3.4.3 BET analysis*
 - 3.4.4 XPS studies*
 - 3.4.5 PL studies*
 - 3.5 Photocatalytic degradation studies*
 - 3.5.1 Accumulated light energy calculation*
 - 3.5.2 Photocatalytic degradation of methylene blue*
 - 3.5.2.1 Effect photocatalyst*
 - 3.5.2.2 Effect of catalyst loading*
 - 3.5.2.3 Effect of concentration of dye*
 - 3.5.2.4 Effect of concentration of RuO_2*
 - 3.6 Kinetic study*
 - 3.7 Mechanism of photocatalytic degradation of methylene blue*
 - 3.8 Conclusion*
-

3.1 Introduction

Textile dye constitutes one of the major environmental issues for the past decades as they are highly hazardous to the living organisms because of their carcinogenic and non-biodegradable nature¹. We require a complete mineralization process that helps us to get out of the deleterious effect of pollutants. The various advanced oxidative process like sonolysis, photocatalysis, and radiolysis are often used for the environmental remediation process². As photocatalysis results in complete mineralization, most of the degradation studies are based on this method³. Sunlight is an efficient source for photocatalysis as it is quite abundant and renewable. Sunlight-assisted heterogeneous photocatalysis is a cost-effective technology for the mineralization of recalcitrant chemicals⁴.

As explained in the previous chapter TiO_2 is an ideal semiconductor photocatalyst that is cost effective, ecofriendly, chemically inert, photocatalytic active and non toxic⁵⁻⁷. TiO_2 is widely used in various areas like drug delivery, sensors, electrochemical cells, electrodes, solar cells, mineralization of various pollutants, photovoltaic cell, water splitting etc⁸⁻¹⁰. The wide band gap of TiO_2 restricts the complete utilization of solar energy as it can absorb only in the UV region¹¹. Another drawback of TiO_2 is the electron-hole recombination. To extend the visible light activity and enhance the charge separation several strategies have been proposed by various research groups including metal or nonmetal doping, coupling with semiconductors, dye sensitization, the addition of sacrificial reagent, and construction

of heterojunction¹²⁻¹⁴. Coupling TiO₂ nanomaterials with metal oxides were found to be a suggestive method for enhanced solar conversion efficiency.

RuO₂ is a superior electrode material because of its high metallic conductivity and thermodynamic stability¹⁵. The Ru_{1-x}Ti_xO₂ solid solution is an excellent catalyst in various areas like gas sensing, catalysis, drug delivery, antibacterial activity, and supercapacitor¹⁶⁻²⁰. Studies have shown that coupling of TiO₂ with RuO₂ resulted in a remarkable change in photocatalytic efficiency. Kim et al adopted the acetic acid-mediated sol-gel process for the preparation of Ru/TiO₂ catalyst. RuO₂ nanomaterials were supported on mesoporous TiO₂ for the successful methanation of CO₂²¹. Seki et al developed thermally stable RuO₂/Rutile TiO₂ in which RuO₂ crystallites are highly dispersed for the oxidation of HCl through a green process²². Adel et al evaluated the photocatalytic degradation efficiency of the hexagonal TiO₂/RuO₂ mesoporous nanocomposite prepared by the sol-gel method by the photooxidation of methanol and observed that the incorporation of RuO₂ results in the increase of photonic efficiency²³. Tian et al adopted a coprecipitation method for the synthesis of nanobelt heterostructure TiO₂/RuO₂ in which RuO₂ was dispersed on TiO₂ nanobelts for the successful photocatalytic degradation of methyl orange²⁴.

The high surface to volume ratio of mesoporous structures enables them to enhance the photocatalytic efficiency due to the availability of more surface active sites²⁵. It has been reported in various papers that

the surface properties of the catalysts like surface area, porosity, grain size, pore volume, etc. have a profound influence on the photocatalytic performance²⁶⁻²⁸. The mesoporous materials can harvest more amount of sunlight due to their large surface area. Changsheng et al developed mesoporous TiO₂ microspheres through a one-step solvothermal process and achieved enhanced photocatalytic degradation of Bisphenol A in comparison to the commercial P25 TiO₂ under UV illumination²⁹. The transparent mesoporous TiO₂ synthesized by Jimmy et al via modified reverse micellar and sol-gel route showed superior photocatalytic activity and light induced hydrophilicity due to the presence of mesopores of high surface area and roughness and enhanced separation of photogenerated electrons and holes³⁰.

There are various methods for the preparation of TiO₂ i.e., electrochemical, hydrothermal, sol-gel, dip coating, ball milling etc³¹. Among these sol-gel method is the simplest and most convenient method to synthesize shape and size controlled, crystalline, pure, and homogenous nanomaterials³¹. Roy and coworkers synthesized a wide variety of ceramic oxide compositions of high purity and homogeneity by following the sol-gel method³². Valencia et al synthesized TiO₂ nanoparticles in the anatase phase that showed high photocatalytic activity for degradation of methyl orange prepared, by sol-gel method followed by hydrothermal treatment³³. Yongfa et al performed the sol-gel process for the synthesis of TiO₂ nano Powders and conducted a study on the influence of gelation time, size, and reactivity on the polymerization process³⁴.

Herein we demonstrate sunlight-assisted photocatalytic degradation of methylene blue using the binary nanocomposite mesoporous $\text{TiO}_2/\text{RuO}_2$. The sol-gel method was employed to synthesize the mesoporous material. Pluronic acid was used as a structure-directing agent for framing the mesoporous structure. We have conducted studies to monitor the effect of various parameters like catalyst loading, irradiation time, the concentration of dye, and the concentration of Ru on the photocatalytic degradation of methylene blue. The catalyst that we have developed in the present work was much effective for the mineralization process.

$\text{TiO}_2/\text{RuO}_2/\text{CuO}$ can be considered as a superior catalyst for photocatalytic degradation of methylene blue. Some reports on photocatalytic degradation are presented in Table 1.

Table. 1 Degradation characteristics of various materials

Photocatalyst		Dye		Energy source	% of Degradation		Reference
Name	Catalyst dosage(mg/L)	Name	Concentration (mg/L)		Value	Time (minutes)	
RuO ₂ /10 wt.% SiO ₂ -TiO ₂ nanoparticles	NA	Methyl Orange	5	UV light	100	120	35
N/S-TiO ₂ nanoparticles	125	Methyl Orange	10	UV light	88	90	36
N/S-TiO ₂ nanoparticles	125	Methyl Orange	10	Sunlight	41	130	36
2wt.%Ag/1.9 wt.% In ₂ O ₃ -TiO ₂ Nanocomposite	1.67	Rhodamine B	25	UV light	100	105	37
N/S-TiO ₂ nanoparticles	125	Methyl Orange	10	UV light	88	105	38
at.% B/5 at.% N-TiO ₂ nanopowder	2.8	Methyl Orange	18	vis light irradiation	99.6	240	39
1at.% Cu-TiO ₂	500	Acid Orange 7	70.06	UV light	100	150	40
PtCl ₄ ²⁻ -TiO ₂	500	Rhodamine B	47.9	vis irradiation	90	120	41
[Pt ₃ (CO) ₆] ₂ -TiO ₂	500	Rhodamine B	47.9	vis irradiation	100	70	41
TiO₂/RuO₂	50	Methylene blue	31.98	Sunlight	100	120	Present work

3.2 Experimental methods

The chemicals used for the preparation of mesoporous TiO₂ and mesoporous TiO₂/RuO₂ nanosystem, their suppliers, and the synthetic procedures are explained in chapter 2.

3.3 Photocatalytic methylene blue degradation studies

Photocatalytic activities of synthesized samples were evaluated by the degradation of methylene blue dye (MB) in sunlight. The absorbance of the solution was measured using JASCO V-750 Spectrophotometer in the wavelength range 200 to 800 nm. The procedure is well explained in chapter 2.

3.4 Results and discussion

We have synthesized the binary mesoporous nanosystem TiO₂/RuO₂ by the sol-gel method and employed it for the degradation of the dye methylene blue under sunlight irradiation. The prepared catalytic systems were characterized using UV-Visible DRS, XRD, BET, and XPS and PL analysis.

3.4.1 UV-Visible DRS analysis

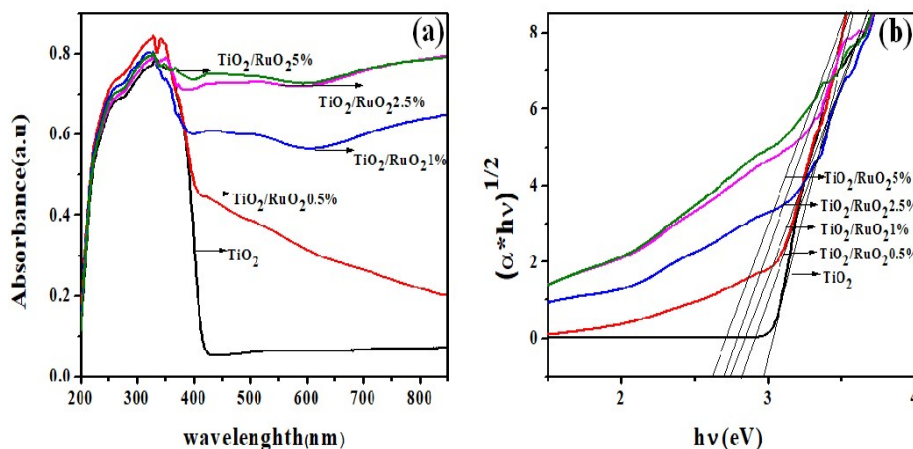


Figure 3.1(a) UV-Vis DRS and (b) Kubelka Munk plot of mesoporous TiO₂, mesoporous TiO₂/RuO₂ with different percentage composition of RuO₂ (0.5, 1, 2.5 and 5 % respectively)

The optical properties of mesoporous TiO₂ and RuO₂ were investigated using UV-Vis DRS analysis. Figure 3.1 displays the UV-Visible DRS spectrum and Kubelka Munk plot of mesoporous TiO₂ and mesoporous TiO₂/RuO₂. In the case of bare TiO₂ absorption band was observed below 400 nm. The band at 224-400 nm was attributed to the transfer of valence band electrons to the conduction band in the Titanium matrix ($O2p \rightarrow Ti3d$)⁴². The introduction of RuO₂ resulted in the observation of the absorption edge in the deep visible light range, 400 to 800 nm. On increasing the RuO₂ content there was an enhancement in the redshift. The thermal excitation of electrons trapped in the defect states was responsible for the enhancement in the red shift⁴³. The absorption in the visible range from 400 to 800 nm can be attributed to the charge transition of the donor ($Ru^{4+} \rightarrow Ru^{5+} + e^{-}$, $Ru^{3+} \rightarrow Ru^{4+} + e^{-}$) or acceptor ($Ru^{3+} \rightarrow Ru^{4+} + h^{*}$)⁴⁴. The band gap of mesoporous TiO₂

and $\text{TiO}_2/\text{RuO}_2$ were estimated using the Kubelka Munk plots derived from UV-Visible diffuse reflectance spectral measurement. The following equation was used to calculate the band gap⁴⁵,

$$\alpha \times hv = A(hv - E_g)^n$$

α = absorption coefficient, ν = frequency of light, E_g = band gap energy, and A = constant, and n is determined by the nature of the semiconductor ($1/2$ or 2 for the direct or indirect transition).

The plots revealed a drastic decrease in band gap from 3 to 2.6 for mesoporous $\text{TiO}_2/\text{RuO}_2$ compared to that of mesoporous TiO_2 . The band gap energy was found to be dependent on the extend of RuO_2 content. As the content of RuO_2 increased in the samples there was a decrease in the band gap.

3.4.2 XRD analysis

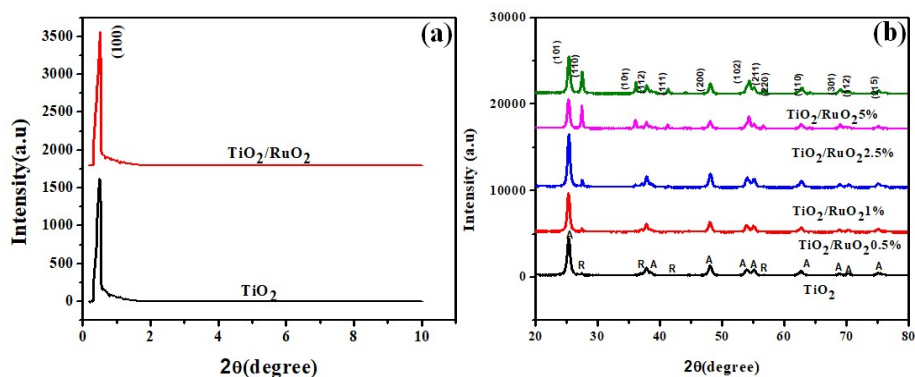


Figure 3.2(a) low angle powder XRD patterns and (b) high angle powder XRD patterns of mesoporous TiO_2 , mesoporous $\text{TiO}_2/\text{RuO}_2$ with different percentage compositions of RuO_2 (0.5, 1, 2.5 and 5% respectively), where A and R stand for anatase and rutile phase respectively.

Figure 3.2 presents the low angle and high angle XRD patterns of mesoporous TiO_2 and $\text{TiO}_2/\text{RuO}_2$. From Figure 3.2(b) it is clear that there isn't a shift in the peak positions of TiO_2 and the binary system. The diffraction patterns clearly indicate the presence of both the anatase and rutile phases. The XRD patterns of all the samples exhibited diffraction peaks at 2θ values of 25.2° , 27.3° , 36.2° , 37.8° , 41° , 48.2° , 54.3° , 55.2° , 56.7° , 62.7° , 68.9° , 70.21° and 75.1° . The peaks with 2θ values 25.2° , 37.8° , 48.2° , 54.3° , 55.2° , 62.7° , 68.9° , 70.21° and 75.15° corresponds to (101), (112), (200), (102), (211), (110), (301), (112), and (215) planes of anatase⁴⁶. Similarly, the peaks at 2θ values of 27.3° , 36.2° , 41° and 56.7° can be indexed to (110), (101), (111), and (220) planes of rutile phase⁴⁷. The intensity of the rutile phase increased with the increase in the concentration of Ru in the doped samples. Notably, the XRD pattern of the catalysts did not show any new peaks which can be ascribed to the high dispersion of Ru^{4+} in the lattice sites of TiO_2 . So, we were not able to observe the peaks corresponding to RuO_2 . As the ionic radii of TiO_2 and RuO_2 were similar the substitution between TiO_2 and RuO_2 was quite easy. The low angle XRD patterns (Figure 3.2(a)) indicated strong diffraction peak corresponding to (100) plane, characteristics of two-dimensional mesoporous structure with spatial group P6mm, typical of structures organized in a hexagonal array⁴⁸.

3.4.3 BET analysis

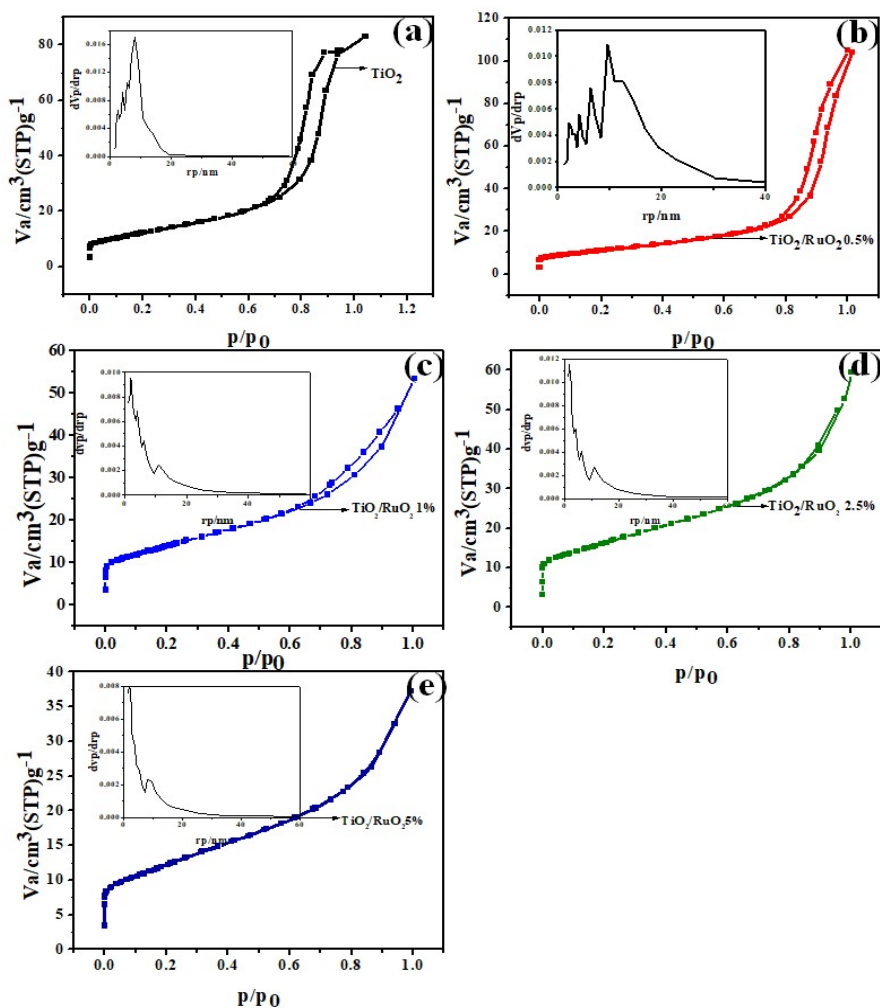


Figure 3.3 N₂ adsorption-desorption isotherms and BJH pore size distribution plots of mesoporous TiO₂, mesoporous TiO₂/RuO₂ with different percentage composition of RuO₂ (0.5, 1, 2.5 and 5 % respectively).

Figure 3.3 shows N₂ adsorption-desorption isotherms and Barret-Joyner-Halenda (BJH) pore size distribution plots of TiO₂ and TiO₂/RuO₂ nanomaterials. Both of the materials exhibited type IV

adsorption-desorption isotherms. The hysteresis loop indicated that the material displays the characteristic feature of type IV isotherm with H3 type hysteresis for mesoporous material⁴⁹. The N₂ adsorption-desorption isotherms of both materials showed a typical type IV isotherm with monolayer adsorption at low values of relative pressures (P/P₀), followed by multilayer adsorption and capillary condensation step at a relative pressure of 0.62-1 P/P₀ and 0.63-0.99 P/P₀ respectively. The presence of type H3 hysteresis loop comprised of plate like particle aggregates forming slit like pores⁵⁰⁻⁵¹.

From textural property studies, it is evident that the average pore size of TiO₂ and TiO₂/RuO₂ were in the mesoporous range. But there was a decrease in pore volume and average pore diameter of the doped materials, TiO₂/RuO₂. The textural properties, including specific surface area, pore volumes, and BJH pore diameters obtained for mesoporous TiO₂ and TiO₂/RuO₂ nanomaterials are summarized in Table .2.

Catalyst	BET surface area (m ² /g)	Pore volume (cm ³ /g)	Average pore diameter (nm)
TiO ₂	43.8	0.1	16.4
TiO ₂ /RuO ₂ 0.5%	39.5	0.1	18.9
TiO ₂ /RuO ₂ 1%	49	0.08	2
TiO ₂ /RuO ₂ 2.5%	57.4	0.09	3.9
TiO ₂ /RuO ₂ 5%	42.605	0.06	3.9

Table. 2.

a. calculated from BET adsorption isotherms

b. calculated from Barrett–Joyner–Halenda (BJH) equation using the desorption isotherm

3.4.4 XPS analysis

The elemental composition of the binary nanosystem was determined using X-ray photoelectron spectroscopy (XPS). We recorded and processed the XPS spectra using CASA XPS and Peak fit 41 software⁵². The internal charge correction was depleted by setting C1s to 284.8 eV. The XPS spectra of the elements Ti2p, Ru3d, and O1s of the mesoporous TiO₂/RuO₂ are represented in Figure.3.4. The atomic percentages of elements obtained from the area of curves are tabulated.

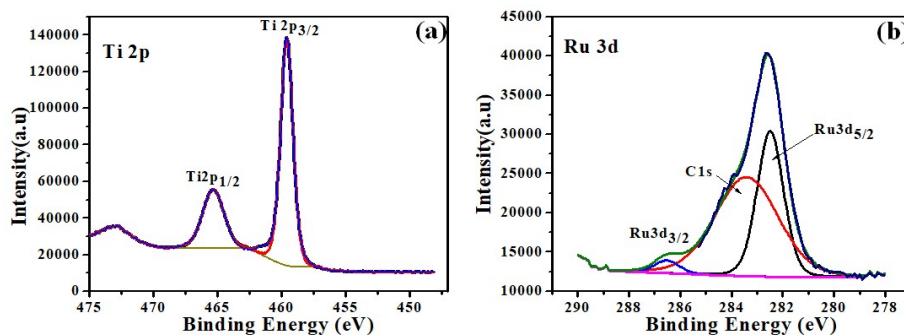


Figure 3.4 CoreLevel Elemental X-ray Photoelectron spectra of (a) Ti2p fitted with single Gaussian components showing valance stability (b) Ru3d in TiO₂/RuO₂ mesoporous nanomaterial

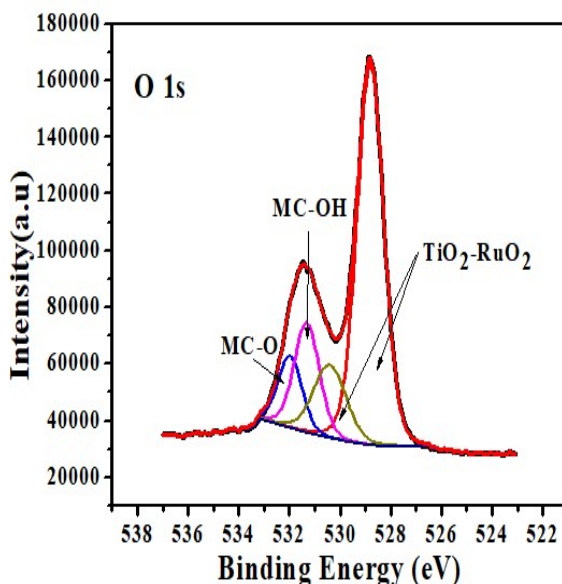


Figure 3.5 Core level Elemental X-ray Photoelectron spectra of O1s in $\text{TiO}_2/\text{RuO}_2$ mesoporous nanoparticles

Name	Position (eV)	FWHM (eV)	At %
Ti2p	459.1	2.6	22.5
Ru3d	286.1	3.6	3.3
O1s	531.1	4.5	74.3

Table.3. XPS fitting parameter obtained from the survey scan of $\text{TiO}_2/\text{RuO}_2$ 0.5 % and the atomic percentages obtained from it

The plots of strong and intense Ti2p emissions coupled with $\text{Ti}2p_{3/2}$ and $\text{Ti}2p_{1/2}$ components and a low intensity Ru3d asymmetric curve fitted with $\text{Ru}3d_{3/2}$ and $\text{Ru}3d_{5/2}$ components are enclosed in Figure.3.4. The elemental photoelectron emissions Ti2p and Ru3d give rise to two different possible energy states for the same level established as the spin-orbit j-j coupling⁵³. $\text{Ti}2p_{3/2}$ situated at 459.58 eV and $\text{Ti}2p_{1/2}$ at

465.28 eV, were fitted with a single Gaussian-Lorentzian established the formation of another chemical state or sub-oxides⁵⁴. As in the previous results, the typical peak difference (ΔV) between Ti2p slip states 5.7 eV is exactly reproduced here⁵⁵. Pure TiO₂ exhibits peaks 458 and 464 eV⁵⁶. The variation in the TiO₂ peak implies the existence of the interaction and electron transfer between TiO₂ and RuO₂⁵⁷. Ru3d emission in the TiO₂/RuO₂ (Fig.3.4. (b)) appeared between 278 eV to 287 eV is an integral peak inclusive of a minimum number of three emissions probably arising from Carbon (C1s) and the split components of Ru3d (Ru3d_{3/2} and Ru3d_{5/2}). As in Figure 3.4 (b) Ru3d_{3/2} at 286.53 eV and Ru3d_{5/2} at 282.48 eV was resolved with spin-orbit split ($\Delta V=4.05$ eV), also consistent with references⁵⁸⁻⁶⁰

Figure 3.5, shows the deconvoluted O1s asymmetric curve obtained from TiO₂/RuO₂ system fitted with corresponding components. Herein, O1s pop up with a strong emission with shoulder peak. Both the emissions are considered as cumulative and are well fitted with four components centered at 528.81 eV, 530.31 eV, 531.39 eV, and 532.03 eV. The binding energy (B.E) positions 528.81 eV and 530.31 eV of the mesoporous TiO₂/RuO₂ is attributed to the Metal-Oxygen (M-O) emissions and clearly, here the only state is +4 state of cations with oxygen⁶¹⁻⁶². By virtue, carbonates will be present in all samples and the 532.03 eV component is assigned as metal-carbonate (M-C) bonded with oxygen and hydroxides (O-H) 531.39 eV⁶¹.

3.4.5 PL studies

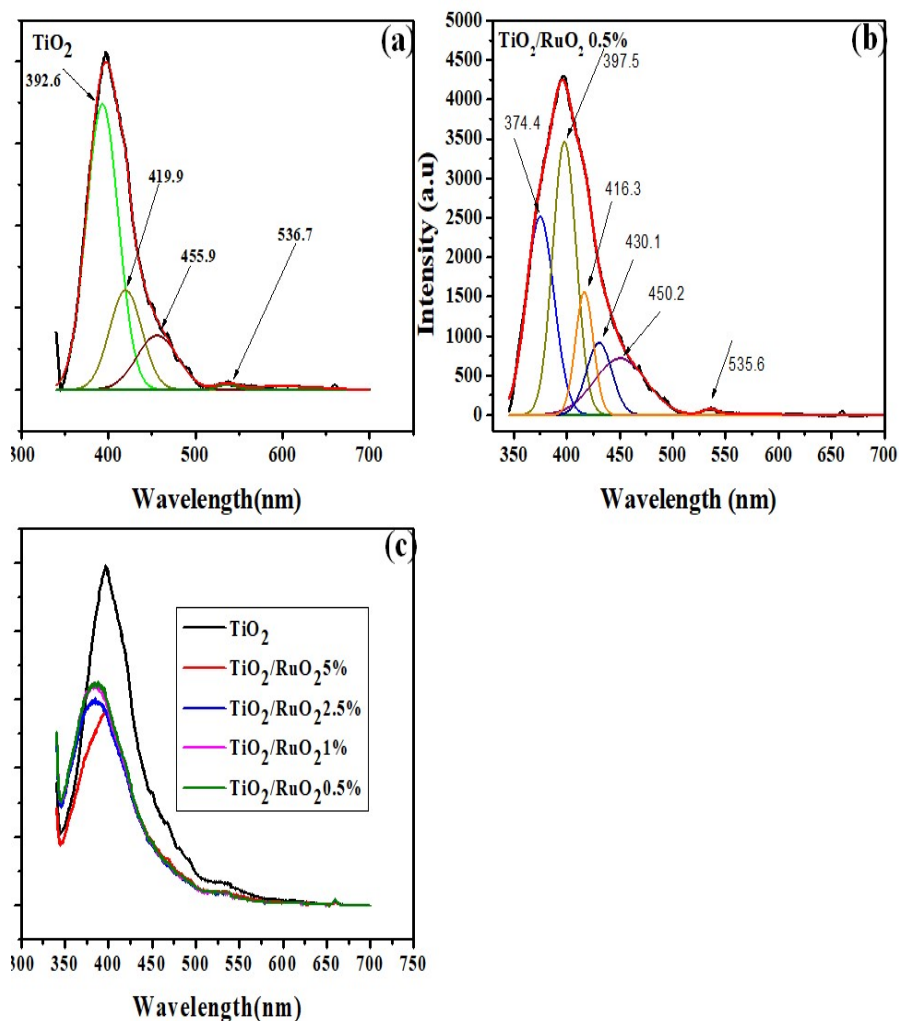


Figure 3.6 Photoluminescence spectra of mesoporous (a) TiO₂ (b) TiO₂/RuO₂ nanomaterials with different percentage composition of RuO₂ (0.5, 1, 2.5 and 5 % respectively) photoluminescence spectra of the samples (c) Relative emission from TiO₂ and TiO₂/RuO₂ nanomaterials with different percentage composition of RuO₂ (0.5, 1, 2.5 and 5 % respectively)

PL measurements were carried out with an excitation wavelength of 330 nm and the emission spectrum was monitored in the range from 345 to 700 nm. A broad emission band was observed in the spectral range from 350-550 nm in the PL spectrum originated from various transitions of valance band to the conduction band and vice versa. The deconvolutions in PL illustrate corresponding bands. The surface modification of TiO₂ with RuO₂ has resulted in an appreciable change in the PL emission spectra of the binary TiO₂/RuO₂ nanosystem. The deconvoluted PL spectra of TiO₂ analysis indicated the main PL emission peak at 392 nm and shoulder peaks at 420, 456, and 537 nm. In the case of TiO₂/RuO₂ nanomaterial the dominant peak was observed at 398 nm and shoulder peaks at 374, 416, 430, 450, and 536 nm. The emission of intermediate band transmission of Titania was responsible for the shoulder peak around 370 nm⁶³. The emission peak around 392 nm was due to the direct transition of energy from the conduction to valence band⁶⁴. The peak around 416 and 536 nm is due to the self-trapped excitons that are being located on TiO₆ octahedran⁶⁵. The emission peak around 430 nm can be attributed to the electron transmission being facilitated by defect levels in the band gap like the formation of oxygen vacancies during the synthesis of samples⁶⁶. The shallow trap level due to the oxygen vacancy accounts for the emission peak around 450 nm⁶⁷⁻⁶⁸. The PL intensity of TiO₂/RuO₂ is suppressed in comparison to TiO₂. The lower PL intensity for TiO₂/RuO₂ binary system suggests reduced recombination and efficient electron-hole separations in the compound. The order of PL intensity is as follows TiO₂ > TiO₂/RuO₂ 5 % > TiO₂/RuO₂ 2.5 % > TiO₂/RuO₂ 1% > TiO₂/RuO₂ 0.5 %.

3.5 Photocatalytic degradation studies

3.5.1 Accumulated light energy calculation

The intensity of sunlight was measured at an interval of 5 minutes using LUXMETER (LX-103). The conversion of the intensity of sunlight to accumulated light energy is presented in Table 4.

Irradiation time(min)	In hours	Light intensity (LUX)	Integrated area of Intensity× time graph(A)	Wh/m ² A*0.0094444	Wh(*exposed area of the reaction mixture)	KWh
0	0	178000				
5	0.083	190000				
10	0.167	188000				
15	0.250	195000	63227.5	597.15	660.01	0.66
20	0.333	195000				
25	0.417	190000				
30	0.500	188000				
35	0.583	193000	127108	1200.46	1326.84	1.32
40	0.667	193000				
45	0.750	193000				
50	0.833	195000				
55	0.917	179000	190382	1798.04	1987.34	1.98
60	1	179000				
65	1.083	187000				
70	1.167	182000				
75	1.250	185000	251654.5	2376.73	2626.95	2.63
80	1.333	185000				
85	0.083	196000				
90	0.167	196000				
95	0.250	190000	316464.5	2988.82	3303.48	3.3
100	0.333	190000				
105	0.417	182000				
110	0.500	185000				
115	0.583	196300	395177.66	3732.22	4125.14	4.12
120	0.667	196300				

Table.4 Accumulated light energy calculations for the study on photocatalytic degradation of cefixime.

3.5.2 Photocatalytic degradation of methylene blue

Figure 3.7 represents the UV-Visible spectra of degradation of 10^{-5} M methylene blue collected every 20 minutes interval after exposure to sunlight using .005 g mesoporous $\text{TiO}_2/\text{RuO}_2$.

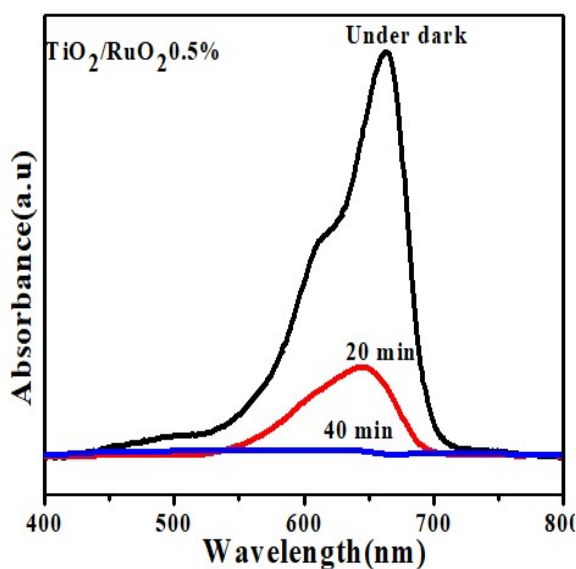


Figure 3.7 UV-Vis Spectra of the reaction mixtures after catalyst removal, collected after sunlight irradiation of 0, 20 and 40 minutes of 100 mL reaction mixture with 10^{-5} M methylene blue and 0.005 g mesoporous $\text{TiO}_2/\text{RuO}_2/\text{CuO}$ 0.05 % catalyst

From the results, it was evident that there was an increase in degradation efficiency with the progress of time. Most of the degradation has occurred in the initial 20 minutes, and after that, the degradation was slowed down. This may be attributed to the production of a large amount of free radicals in the first twenty minutes. Thereafter there was a decrease in the rate of degradation.

The mineralization process was accompanied by the production of certain intermediates. As the reaction proceeded, the free radicals produced by the photocatalysts might have been consumed by the intermediates produced during the degradation process. This ultimately resulted in the low availability of the free radicals for the mineralization process. We achieved the complete degradation of methylene blue within 40 minutes.

3.5.2.1 Effect photocatalyst

The degradation of methylene blue of concentration 10^{-5} M concentration using different catalysts is shown in Figure 3.8. Among the various catalysts mesoporous $\text{TiO}_2/\text{RuO}_2$ 0.5 % was found to be more efficient in the sunlight-assisted degradation of the methylene blue.

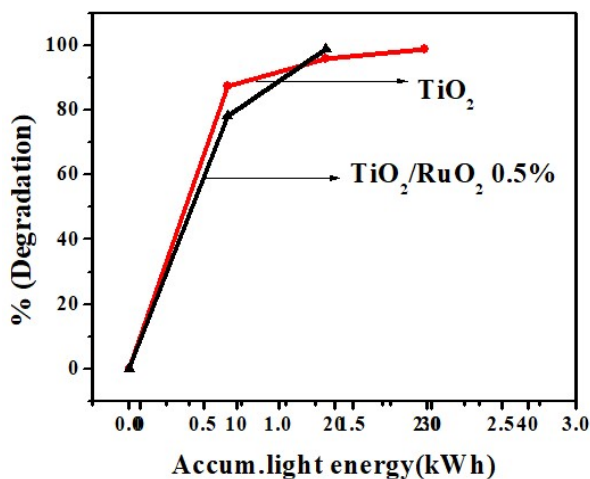


Figure 3.8. Performance of different photocatalysts towards the sunlight-assisted degradation of 10^{-5} M methylene blue.

The photocatalytic efficiency of semiconductors is influenced by various factors of the catalysts like crystallinity, surface area, size of the particles, and amount of the dopants⁶⁹. The results that we obtained were in accordance with this fact. The greater activity of mesoporous TiO₂ may be attributed to the large surface area of the photocatalyst. However, the performance of the catalyst mesoporous TiO₂/RuO₂ was superior to that of mesoporous TiO₂. This may be because of the low band gap energy and reduced recombination of electrons and holes in the binary system of mesoporous TiO₂/RuO₂ system in comparison with the mesoporous TiO₂. The argument is well supported by UV-Visible diffuse reflectance spectroscopy and PL measurements.

3.5.2.2 Effect of Catalyst loading

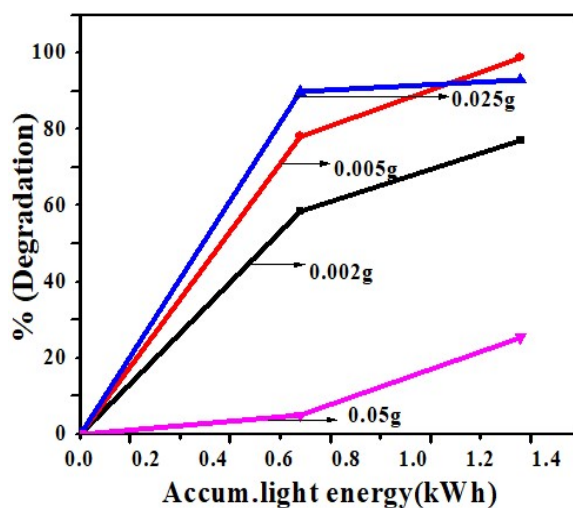


Figure 3.9. Optimization studies of catalyst weight carried out under irradiation with sunlight

The effect of catalyst weight on degradation efficiency was investigated by varying the mass of the catalyst keeping all other parameters fixed. The results obtained are summarized in Figure 3.9. Initially, on increasing the weight of the catalyst from 0.002 to 0.025 g an enhancement in photocatalytic degradation was observed. The degradation rate increased with the amount of catalysts because of the generation of more photoexcitation centers. But the rate was found to decrease with the further increase of the amount of catalyst to 0.05 g. This can be rationalized based on the availability of light for degradation. As the amount of catalyst mixture increased, the transparency of the reaction mixture was lost due to the adverse effect of absorption and scattering caused by the aggregation of catalyst⁷⁰. Thus, the increased opacity of the suspension brought about by the higher amount of catalyst resulted in the decrease of the photocatalytic efficiency at high catalyst loading⁷¹. The maximum degradation was observed when the mass of the catalyst was 0.025 g. Thus, the minimum percentage of degradation at high catalyst concentration can be attributed to the minimum availability of light for the generation of photoexcited electrons and holes.

3.5.2.3 Effect of concentration of dye

We have monitored the effect of the concentration of methylene blue on the degradation of methylene blue by varying the concentration of methylene blue from 10^{-5} M concentration to 10^{-4} M by keeping all other parameters constant. The results obtained are summarized in Figure 3.10.

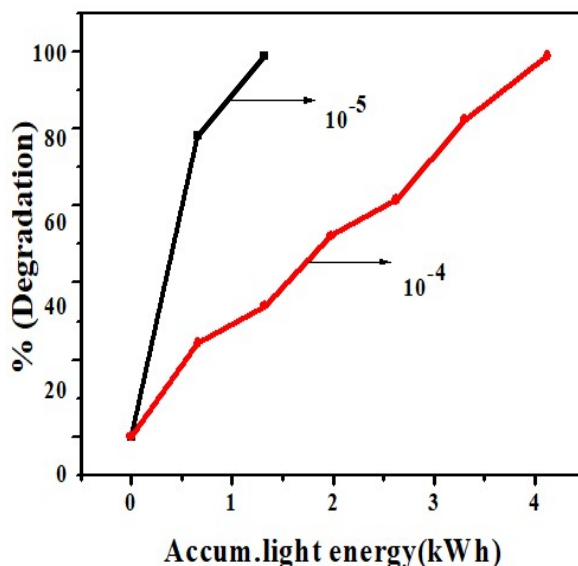


Figure 3.10. Effect of initial methylene blue concentration

It can be inferred that the degradation efficiency decreased with the increase in the concentration of methylene blue. This may be due to the fact that with the increase in the concentration of dye the requirement of the surface of the photocatalyst increased. However, as the availability of the catalyst mass, time, and all parameters were fixed there would be a decrease in the generation of free radicals responsible for the degradation⁷⁰. And also, as the concentration of methylene blue increased, more dye may be adsorbed on the catalyst surface which adversely affected the path length of light entering into the solution⁷². Hence at a high concentration of methylene blue, there will be a decrease in photocatalytic efficiency as a part of sunlight entering the surface of the catalyst may be adsorbed by dye rather than the catalyst which inhibits the generation of photoactive species.

3.5.2.4 Effect of concentration of RuO₂

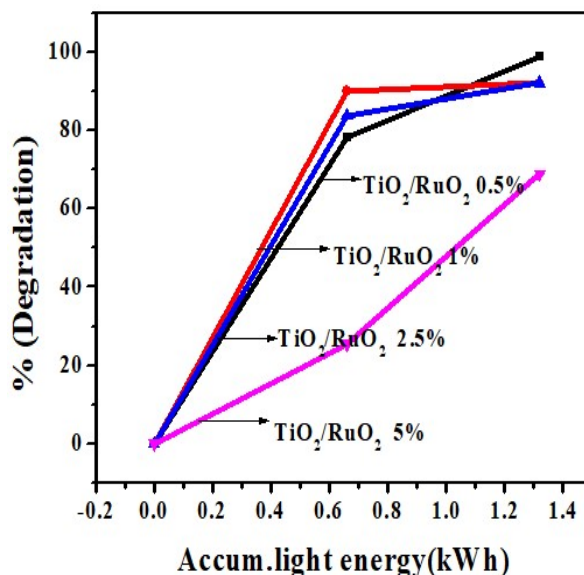


Figure 3.11 Effect of concentration of RuO₂

We carried out the photocatalytic degradation of methylene blue using different concentrations of RuO₂ keeping all other parameters fixed and the results obtained are illustrated in Figure 3.11. It can be seen that the mesoporous TiO₂/RuO₂ 0.5 % was the most effective photocatalytic system in the mineralization of methylene blue under sunlight irradiation. On increasing the concentration of the dopant there was suppression in the performance of the photocatalytic system. Though the presence of RuO₂ led to a substantial increase in the photocatalytic rate, the excess of RuO₂ resulted in a drastic reduction in the degradation performance. The excess amount of RuO₂ on TiO₂ might have decreased the specific surface area of TiO₂ and obstructed the adsorption of the reactant on the catalyst by masking the surface of

TiO₂⁷³. All these factors contributed to the reduction of performance of the photocatalysts.

3.6 Kinetic study

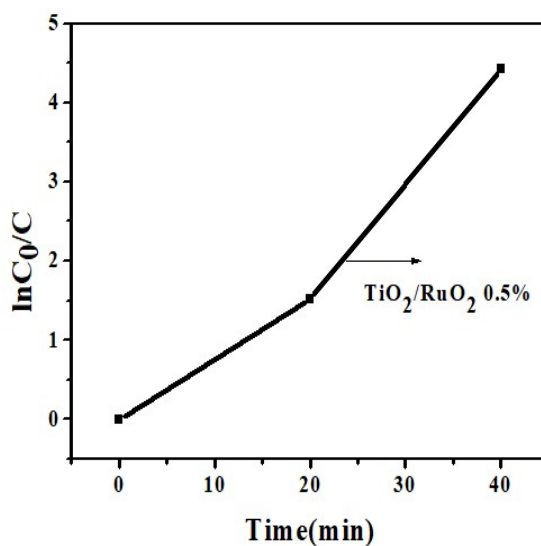


Figure 3.12 Plot of $\ln C_0/C$ versus time for the degradation of methylene blue

The degradation kinetics of methylene blue using the mesoporous TiO₂/RuO₂ 0.5 % can be described based on the Langmuir Hinshelwood model. In the present study, the degradation of methylene blue followed first-order kinetics. The rate of degradation of methylene blue can be expressed by the following relation⁷⁴.

$$\ln C_0/C = kt$$

where C_0 is the initial concentration of the dye methylene blue, C is the concentration of methylene blue at time t , k is the apparent rate constant.

The plot of $\ln C_0/C$ versus time for the degradation of methylene blue is shown in Figure 3.12. From the linear fit of $\ln C_0/C$ against time, it is evident that the degradation kinetics is first order. The apparent rate constant is obtained from the slope of the graph. The value of $K_{app}t$ and regression coefficient obtained from the regression analysis is summarized in Table.5.

Photocatalyst	Regression coefficient(R^2)	$K_{app}(\text{min})^{-1}$
Mesoporous $\text{TiO}_2/\text{RuO}_2/\text{CuO}$ 0.5 %	0.94	0.11

Table.5 Value of $K_{app}t$ and regression coefficient

3.7 Mechanism of photocatalytic degradation of methylene blue

Figure 3.13 illustrates the charge transfer mechanism taking place in the binary mesoporous system $\text{TiO}_2/\text{RuO}_2$ nanosystem. It has been reported that the conduction band edge of RuO_2 (0.76) is more positive than that of TiO_2 (-0.27) and also the valence band edge of TiO_2 (2.88) is more positive than that of RuO_2 (2.98)²⁴. Due to the matching band structure of RuO_2 and TiO_2 , the photoexcited electrons of the TiO_2 are transferred to the conduction band of RuO_2 , on exposure to sunlight. At the same time, the holes in the valence band of RuO_2 are transferred to the valence band of TiO_2 . This leads to the effective separation of charges and the electrons and holes migrate to the surface of the

photocatalyst. The holes react with hydroxyl ions producing hydroxyl radicals ($\text{OH}\cdot$) whereas the electrons in the conduction band react with dissolved oxygen generating superoxide anions ($\text{O}_2^{\cdot-}$) which subsequently react with H^+ to generate hydroxyl radicals ($\text{OH}\cdot$). Finally, the hydroxyl radicals ($\text{OH}\cdot$) with high oxidizing ability degrade the methylene blue dye. The enhanced separation of charges and their improved lifetime facilitate the complete degradation of methylene blue under solar irradiation.

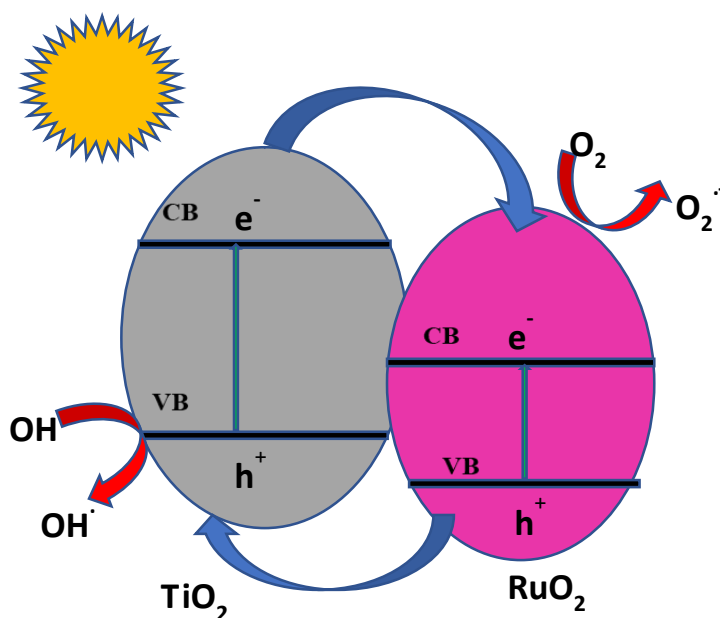


Figure 3.13. Mechanism of methylene blue degradation

3.8 Conclusion

In the present study, we report a facile sol-gel method for the synthesis of binary nanosystem, $\text{TiO}_2/\text{RuO}_2$. We have demonstrated the practical application of the binary system for the environmental remediation

process using sunlight as the irradiation source. In the photocatalytic degradation of methylene blue, the mesoporous TiO₂ was not much effective for the complete mineralization of methylene blue. But the introduction of RuO₂ to the nanosystem resulted in the complete degradation of methylene blue within 40 minutes. The low band gap and reduced electron-hole recombination attributed to the high photocatalytic performance of TiO₂/RuO₂ which is being well supported by UV and PL results. The oxidative degradation of methylene blue was found to be affected by various factors like catalyst loading, the concentration of methylene blue, and the concentration of ruthenium. The degradation of the methylene blue followed first-order kinetics. After all mesoporous TiO₂/RuO₂ proves to be a promising candidate for the degradation of methylene blue using sunlight as the irradiation source.

REFERENCE

1. Ince N.H, Wat. Res, 1999, 33, 1080-1084
2. Stock N.L, Peller J, Vinod Gopal K, Kamat P.V, Environ. Sci. Technol 2000, 34, 1747-1750
3. Akpan U.G, Hameed B.G, Journal of Hazardous Materials, 2009, 170, 520–529
4. Khaki M.R.D, Shafeeyan M.S, Raman A.A.A, Daud W.M.A.W, Journal of Molecular Liquids, 2018, 258, 354-365
5. Gouvea C.A.K, Wypych F, Moraes S.G, Duran N, Nagata N, Peralta-Zamora P, Chemosphere, 2000, 40, 433-440
6. Zhu X, Pei L, Zhu R, Jiao Y, Tang R& Wei Feng, Sci Rep 8, 2018, 12387
7. Gupta S, Tripathi M, Cent. Eur. J. Chem., 2012, 10, 279-294
8. Zaleska A, Recent Patents on Engineering, 2008, 2, 157-164
9. Haider A.J, Jameel Z.N, Al-Hussaini I.H.M, Energy Procedia, 2019, 157, 17-29
10. Yadav S, Jaiswar G, J. Chin. Chem. Soc., 2017, 64, 103-116
11. Ullattil S.G, Periyat P, J. Mater. Chem. A, 2016, 4, 5854 –5858
12. Ni M, Leung M.K.H, Leung D.Y.C, Sumathy K, Renewable and Sustainable Energy Reviews, 2007, 11, 401–425
13. Shayegan Z, Lee C.S, Haghightat F, Chemical Engineering Journal, 2017, DOI.org/10.1016/j.cej. 2017.09.153
14. Low J, Cheng B, Yu J, AppliedSurfaceScience, 2017392, 658–686
15. Kim S.J, Jung H, Lee C, Kim M.H, Jung H.Y, Sensorsand Actuators B, 2014, 191, 298-304

16. Ananth A, Dharaneedharan S, Gandhi M.S, Heo M.S, Mok Y.S, 2013, 223, 729–736
17. Mousli F, Chaouchi A, Jouini M, Maurel F, Kadri A, Chehimi M.M, *Catalysts*, 2019, 9, 578
18. Wang Y, Zhang X.G, *Electrochimica Acta*, 2004, 49, 1957–1962
19. Chueh Y.L, Hsieh C.H, Chang M.T, Chou L.J, Lao C.S, Song J.H, Gan J.Y, Wang Z.L, *Adv. Mater.* 2007, 19, 143–149
20. Chrzescijanska E, Kusmierk E, *Journal of Photochemistry and Photobiology A: Chemistry*, 2013, 257, 5-10
21. Kim A, Sanchez C, Bernard Haye, Boissiere C, Sassoie C, Debecker D.P, *ACS Appl. Nano Mater*, 2019, 2, 3220–3230
22. Kohei Seki, *Catal Surv Asia*, 2010, 14, 168–175
23. Adel A. Ismail, Lars Robben, and Detlef W. Bahnemann, *Chem Phys Chem*, 2011, 12, 982–991
24. Tian J, Hu X, Wei N, Zhou Y, Xu X, Cui H, H Liu, *Solar Energy Materials & Solar Cells*, 2016, 151, 7–13
25. Yu Y, Yu J.C, Yu J.G, Kwok Y.C, Che Y.K, Zhao J.C, Ding L, Ge W.K, Wong P.K, *Applied Catalysis A: General*, 2005, 289, 186–196
26. Subramanian V, Wolf E.E, Kamat P.V, *J. Am. Chem. Soc.*, 2004, 126, 4943
27. Yu J.C, Yu J.G, Ho W.K, Jiang Z.T, Zhang L.Z, *Chem. Mater.*, 2002, 14, 3808-3816
28. Yu J, Wang G, Cheng B, Zhou M, *Applied Catalysis B: Environmental*, 2007, 69, 171–18
29. Guo C, Ge M, Liu M, Gao G, Feng Y, *Environ. Sci. Technol.* 2010, 44, 419–425

30. Jimmy C. Y, Jianguo Y, Wingkei H, Jincai Z, *Journal of Photochemistry and Photobiology A: Chemistry*, 2002, 148, 331–339
31. Akpan U.G, Hameed B.H, *Applied Catalysis A: General*, 2010, 375, 1–11
32. Hench L.L, West J.K, *Chem. Rev.*, 1990, 90, 33-72
33. Valencia S, Marin J.M, Restrepo G, *The Open Materials Science Journal*, 2010, 4, 9-14
34. Zhu Y, Zhang L, Gao C, Cao L, *Journal of Materials Science*, 2000, 35, 4049– 4054
35. Ibhadon A.O, Greenway G.M, Yue Y, *Catal. Commun.*, 2008, 9, 153–157
36. Wei F, Ni L, Cui P, *J. Hazard. Mater.* , 2008, 156, 135–140
37. Suarez-Parra R, Hernandez-Perez I, Rincon M.E, Lopez-Ayala S, Roldan-Ahumada M.C, *Sol. Energy Mater. Sol. Cells* , 2003, 76, 189–199
38. Wei F, Ni L, Cui P, *J. Hazard. Mater.*, 2008, 156, 135–140.
39. Gombac V, De Rogatis L, Gasparotto A, Vicario G, Montini T, Barreca D, Balducci G, Fornasiero P, Tondello E, M. Graziani, *Chem. Phys.*, 2007, 339, 111–123
40. Wong R.S.K, Feng J, Hu X, Yue P.L, *J. Environ. Sci. Health A*, 2005, 39, 2583–2595
41. Kowalska E, Remita H, Colbeau-Justin C, Hupka J, Belloni J, *J. Phys. Chem. C*, 2008, 112, 1124–1131
42. Ismael M, *New J. Chem.*, 2019, 43, 9596-9605
43. Mihail S, Cursaru1 D.L, Matei D, Manta A.M, Somoghi R, Branoiu G, *Sci Rep*, 2019, 9, 18798
44. Nguyen-Phan T.D, Luo S, Vovchok D, Llorca J, Sallis S, Xu W, Bai J, Piper L.F.J, Polyansky D.E, Senanayake S.D,

-
- Stacchiola D.J, Rodriguez, J.A, Phys. Chem. Chem. Phys, 2016, 18, 15972-15979
45. Raman K, Masilamani S.A, Chandra Bose R.S, Rasayan J. Chem, 2018, 11, 53-62
46. Al-Taweel S.S, Saudethod H.R, J. Chem. Pharm. Res., 2016, 8, 620-626,
47. Duan Y, Zhang M, Wang L, Wang F, Yang L, Li X, Wang C, Applied Catalysis B: Environmental, 2017, 204, 67–77
48. Fernandes F.R.D, Pinto F.G.H.S, Lima E.L.F, Souza L.D, Caldeira V.P.S, Santo A.G.D, Appl. Sci. 2018, 8, 725
49. Singh K.S.W, Pure & Appl Chem, 1985 57, 603—619
50. Zhelin W, Xuewei J, Mao P and Yongmin S, Minerals, 2020, 10, 377
51. Leofanti G, Padovan M, Tozzola G, Venturelli B, Catalysis Today, 1998, 41, 207-219
52. Luo W, Surface chemistry of black phosphorus under a controlled oxidative environment, Nanotechnology, 2016, 27, 434002
53. Biesinger M, C, Payne B.P, Grosvenor A.P, Lau L.W.M, Gerson A.R, Applied Surface Science, 2011, 257, 2717-2730
54. Bond G.C, Flamerz S, Appl. Catalysis , 1989, 46, 89-102
55. Gonbeau D, Guimon C, Pfister-Guillouzo G, Levasseur A, Meunier G, Dormoy R, Surf. Sci. , 1991, 254, 81 -89
56. Jia T, Fu F, Yu D, Cao J, Sun G, Applied Surface Science 430, 2018, 430, 438–447
57. Divya K. S, Xavier M.M, Vandana P. V, Reethu V. N., Mathew S, New J. Chem., 2017, 41, 6445-6454
58. Shen J.Y, Adnot A., Kaliaguine S, Appl. Surf. Sci. , 1991, 51, 47-60
-

-
59. Jayaram P, Pradyumnan P.P, Karazhanov S.Z, *Physica B Condensed matter*, 2016, 501, 140-145
 60. Felthouse T.R., Fraundorf P.B., Friedman R.M., Schosser C.L, *J. Catal.*, 1991, 127, 421-444
 61. Taylor J.A., Perry D.L, *J. Vac. Sci. Technol. A*, 1984, 2, 771 - 774
 62. Sivastava S, Badrinarayanan S, Mukhedkar A.J, *Polyhedron*, 1985, 4, 409-414
 63. Giahi M, Pathania D, Agarwal S, Alid G.A.M, Chong K.F, Gupta V.K, *Studia UBB Chemia*, 2019, 1, 7-18
 64. Sinthiya M.M.A, Kumaresan N, Ramamurthi K, *Bull Mater Sci*, 2019, 42, 127
 65. Chang Y.M, Wu J.M, *Crystal Growth & Design* , 2010, 10, 1647-1651
 66. Zhao Y, Li C, Liu X, Gu F, Jiang H, Shao W, Hang L, He Y, *Materials Letters*, 2010, 61, 79-83
 67. Wu Z, Wang Y.Y, Sun L, Mao Y, Wanga M, Lin C, *J. Mater, J. Mater. Chem. A* , 2014, 2, 8223 -8229
 68. Saha A, Moya A, Kahnt A, Iglesias D, Marchesan S, Wannemacher R, Prato M, Vilatela J, and Guldi D.M, *Nanoscale*, 2017, 9, 7911-7921
 69. Muruganandham M, Swaminathan M, *Journal of Hazardous Materials B*, 2006, 135, 78–86
 70. Neppolian B, Choi H.C, Sakthivel S, Arabindoo B, Murugesan V, *Journal of Hazardous Materials B*, 2002, 89, 303–317
 71. Daneshvar N, Salari D, Khataee A.R, *Journal of Photochemistry and Photobiology A: Chemistry*, 2003, 157, 111–116
-

72. Sobana N, Swaminathan M, Separation and Purification Technology, 2007, 56, 101–107
73. Akpan U.G, Hameed B.H, Journal of Hazardous Materials, 2009, 170, 520–529
74. Anwar M.S, Danish R, and Koo B.H, Journal of Nanoscience and Nanotechnology, 2016, 16, 12851–12855

CHAPTER 4

SYNTHESIS AND CHARACTERIZATION OF MESOPOROUS TiO₂/RuO₂/CuO TERNARY NANOSYSTEM

Contents

4.1 Introduction

4.2 Experimental methods

4.3 Results and Discussion

4.3.1 UV-Visible DRS analysis

4.3.2 XRD analysis

4.3.3 BET analysis

4.3.4 XPS studies

4.3.5 SEM studies

4.3.6 TEM studies

4.3.7 PL studies

4.4 Conclusion

4.1 Introduction

Titanium dioxide (TiO_2) is a versatile semiconductor material with a wide variety of applications in photocatalysis¹, DSSC², solar hydrogen energy production³, CO_2 reduction⁴, bacterial degradation⁵, electrocatalysis⁶, and in optoelectronic application⁷. TiO_2 is one of the most widely used photocatalysts because of its excellent chemical and thermal stability, highly economical, nontoxic nature, availability, resistance to photo-corrosion, and high photocatalytic efficiency⁸⁻¹⁰. However, for the conventional TiO_2 , there are numerous shortcomings like poor visible sensitivity, high electron-hole recombination and wide band gap^{8, 10, 11}. To overcome these limitations various techniques are adopted to modify the features of TiO_2 to improve the photocatalytic efficiency¹².

It was reported that the coupling of TiO_2 with metal oxides such as transition metal oxide or sulfide can improve the visible light sensitivity and photocatalytic activities of TiO_2 ¹³⁻¹⁶. However poor stability and high photocorrosion of such systems limit their applications in various fields. The transition metal oxide, RuO_2 acts as an adaptable candidate for both photocatalytic and electrocatalytic activity with relatively high stability¹⁷⁻¹⁸. It exhibits various properties like high metallic conductivity, electrical conductivity, electrochemical stability, low resistivity, high thermal stability, and high resistance to chemical corrosion¹⁹⁻²⁰. This material has been used in various realms of life. RuO_2 have been used as a catalyst in various organic transformations, electrochemical process, and photocatalytic process²¹⁻

²⁵. The binary metal oxide consisting of TiO₂/RuO₂ has been explored recently in various applications²⁶⁻²⁸. Moreover, recent studies of binary oxide focused on TiO₂/CuO due to extended visible light absorption and controlled recombination of photogenerated electron-hole pairs²⁹⁻³¹. The biological and chemical stability, low cost, superior adsorption capacity, narrow band gap, etc. adorn CuO as a supreme candidate for catalysis, adsorption of gas, electrochemical sensors, superconductors, lithium-ion batteries, supercapacitors, antimicrobial materials etc³²⁻³³.

Mesoporous materials are known for their catalytic applications, which are characterized by ordered pore structure, large surface area, porosity, and high thermal stability³⁴. A large surface area enables the photocatalyst in enhancing the photocatalytic performance. Kim et al synthesized mesoporous TiO₂ via sol-gel method using triblock copolymer as structure-directing agent³⁵. It was observed that mesoporous TiO₂ exhibited higher photocatalytic activity in the degradation of methylene blue in comparison to P25. Furthermore, the photocatalytic disinfection of bacteria was found to be better when mesoporous TiO₂ was used as the photocatalyst. Zhou et al reported the facile synthesis of ordered mesoporous black TiO₂ with a high surface area³⁶. The material depicted excellent photocatalytic performance towards hydrogen evolution. Bastakoti et al synthesized mesoporous TiO₂/RuO₂ composite with uniform pore size 30 nm via facile one-pot approach. Poly (styrene-*b*-2-vinyl pyridine-*b*-ethylene oxide) triblock copolymer was used as structure-directing agent³⁷. Rahimnejad et al reported the synthesis of copper oxide-titania

catalysts with nanocrystalline mesoporous structure via single-step sol-gel route³⁸. The synthesized nanomaterial exhibited a high surface area that enabled it to act as an efficient photocatalyst.

Mesoporous materials can be synthesized either in the presence or absence of templates. The most commonly used structure-directing agents used for the synthesis of mesoporous materials are triblock copolymers like pluronic (P123) and pluronic (F127), diblock copolymer polyoxyethylene (10) cetyl ether (Brij-56), other surfactants like tetradecyl phosphate, dodecyl phosphate, tetradecylamine, dodecylammonium chloride (DDAC), cetyl methyl ammonium bromide (CTAB). Results from various studies reveal that the texture and porous structure of the catalysts were finely tuned when pluronic P123 was used as structure-directing agent³⁹⁻⁴⁰.

Many routes are reported for the preparation of TiO₂/RuO₂ nanomaterials, oxidative pyrolysis or sol-gel techniques are common synthetic methods adopted for the preparation of RuO₂ based oxide on the metal surface⁴¹. Guglielmi et al adopted the sol-gel method to prepare RuO₂-TiO₂ films containing 30 mol % of RuO₂ and 70 mol % of TiO₂⁴². Malek et al used the sol-gel method to prepare single phase solid solutions from the amorphous gel through controlled nanocrystallization⁴³. Panic et al synthesized RuO₂-TiO₂ active coating and recommend sol-gel coating can provide uniform dissolution of active species and optimal porosity⁴⁴. Swider et al synthesized aerogels comprised of ruthenium dioxide-titanium dioxide, (Ru-Ti) Ox with enhanced surface area via sol-gel method⁴⁵.

Various studies have been conducted on the binary systems TiO₂/RuO₂ and TiO₂/CuO⁴⁶⁻⁴⁹. Here we are attempting to extend the mesoporous binary system to the ternary system by doping TiO₂ with RuO₂ and CuO. We expect that doping TiO₂ with oxides of Ru and Cu can improve the functionality of TiO₂ when the mesoporous materials of them are synthesized. Based on knowledge such a kind of ternary system with a large surface area is not reported yet. The efficiency of photocatalysts mainly depends on the surface area and the synthetic route of the materials⁵⁰.

In the present work, we report the synthesis and characterization of ternary metal oxide TiO₂/RuO₂/CuO mesoporous nanostructures by triblock copolymer, pluronic P123 assisted sol-gel method followed by calcination at moderate temperature. The obtained materials were well characterized by UV-Visible spectroscopy, powdered X-ray diffraction (XRD), X-ray photoelectron spectroscopy (XPS), Field emission scanning electron microscopy (FE-SEM), Transmission electron microscopy. The textural properties such as surface area and pore size distribution of the materials were analyzed by Brunauer–Emmett–Teller (BET) adsorption-desorption technique followed by BJH pore size distribution data. The photogenerated electronic transitions, excitations, and deexcitations were elucidated by recording the photoluminescence spectra.

4.2 Experimental method

The chemicals used for the preparation of mesoporous TiO₂, mesoporous TiO₂/RuO₂, and mesoporous TiO₂/RuO₂/CuO

nanomaterials, their suppliers, and the synthetic procedures are well explained in chapter 2.

4.3 Results and Discussions

We have synthesized mesoporous $\text{TiO}_2/\text{RuO}_2/\text{CuO}$ nanomaterials and performed various characterization techniques.

4.3.1 UV-Visible DRS analysis

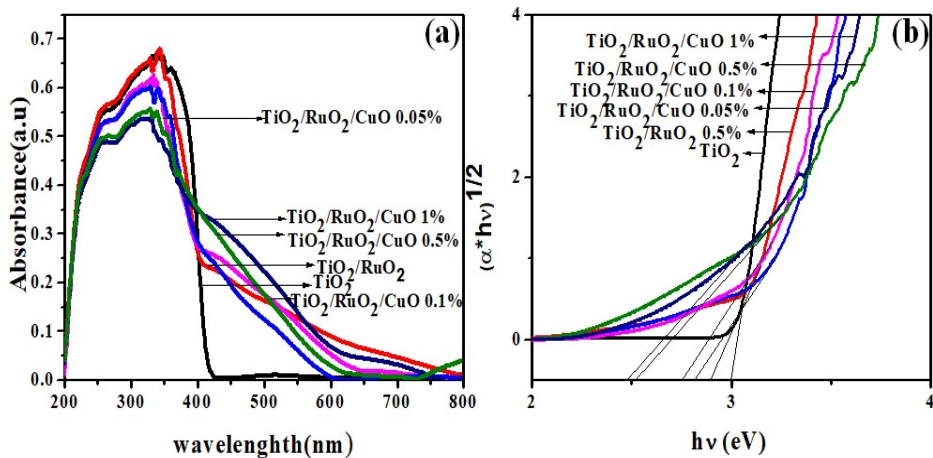


Figure 4.1 (a) UV-Vis-DRS and (b) Kubelka Munk plot of mesoporous TiO_2 , mesoporous $\text{TiO}_2/\text{RuO}_2$ 0.5 % and mesoporous $\text{TiO}_2/\text{RuO}_2/\text{CuO}$ with different percentage composition of CuO (0.1, 0.05 , 0.5 and 1 % respectively)

The optical absorption properties of $\text{TiO}_2/\text{RuO}_2$ and $\text{TiO}_2/\text{RuO}_2/\text{CuO}$ mesoporous nanomaterials have been studied using DRS spectra were presented in Figure 4.1. The absorption spectra of TiO_2 (Figure 4.1(a)) showed a peak below 400 nm, which indicated the transition of electrons from the valence band to the conduction band of TiO_2 ⁴⁸. The introduction of RuO_2 and CuO to TiO_2 has resulted in the shift of

absorbance edge towards the visible range. The absorption band at 224-400 nm was associated with O 2p-Ti 3d transition (from the valence band to conduction band)⁵¹. The Visible-light absorption (400–800 nm) of TiO₂/RuO₂ was due to the charge transition of the donor (Ru⁴⁺ → Ru⁵⁺ + e⁻; Ru³⁺ → Ru⁴⁺ + e⁻) or acceptor (Ru³⁺ → Ru⁴⁺ + h*)⁵¹⁻⁵². CuO loading resulted in the shift of the absorption edge to a longer wavelength region. The absorption band at 400-776 suggested the appearance of crystalline and bulk CuO in octahedral symmetry⁵³. The band gaps of the materials have been calculated from the Kubelka Munk plot (Figure 4.1(a)). The UV-vis spectra recorded data results have shown that the band gaps became narrower and red-shifted for mesoporous TiO₂/RuO₂ and mesoporous TiO₂/RuO₂/CuO nanomaterials. The band gap energy reduced from 3 eV for mesoporous TiO₂ to ~ 2.9 eV for TiO₂/RuO₂ nanomaterial and ~ 2.5 eV for mesoporous TiO₂/RuO₂/CuO nanomaterials respectively. These results indicated that Ru and Cu ions were effectively incorporated into the lattice of TiO₂. The highest band gap reduction was found in mesoporous TiO₂/RuO₂/CuO nanomaterial. The narrow band gap promoted the excitation of electron from the valence band to the conduction band in the doped samples.

4.3.2 XRD analysis

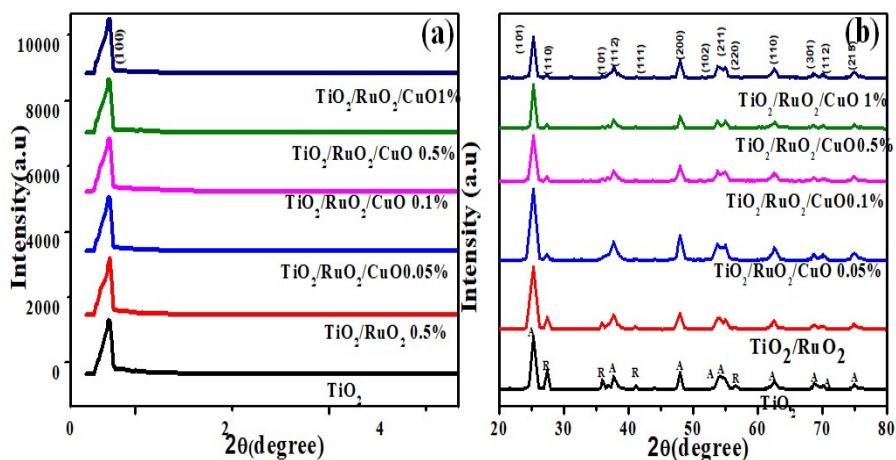


Figure 4.2 (a) low angle powder XRD patterns and (b) high angle powder XRD patterns of mesoporous TiO_2 , mesoporous $\text{TiO}_2/\text{RuO}_2$ and mesoporous $\text{TiO}_2/\text{RuO}_2/\text{CuO}$ with different percentage composition of CuO (0.1, 0.05, 0.5 and 1 % respectively), where A and R stands for anatase and rutile phase respectively.

Figure 4.2 shows the low angle and high angle XRD patterns of mesoporous $\text{TiO}_2/\text{RuO}_2$ and mesoporous $\text{TiO}_2/\text{RuO}_2/\text{CuO}$ nanostructures. All the samples (Figure 4.2(a)) exhibited similar patterns of low angle XRD diffraction corresponding to reflection from (100) plane, characteristics of two-dimensional mesoporous structure with spatial group $P6mm$, typical of structures organized in a hexagonal array⁵⁴. This suggested the formation of mesoporous structures. From the high angle diffraction pattern, it can be inferred that $\text{TiO}_2/\text{RuO}_2$ and $\text{TiO}_2/\text{RuO}_2/\text{CuO}$ have nearly the same peak positions as TiO_2 reported previously in mixed anatase (JCPDS Card no. 21-1272) and rutile phases (JCPDS Card no. 21-1276)⁵⁵⁻⁵⁶. However, the growth of crystallites is conspicuously along with the

anatase phase in the tetragonal geometry of space-group symmetry I41/amd⁵⁶. The diffraction patterns indicated in Figure 4.2(b) are identical and shows both anatase and rutile phases with variation in crystallinity

The Homogeneous growth of nanostructured materials was confirmed from the XRD pattern. The absence of additional peaks in TiO₂/RuO₂ and TiO₂/RuO₂/CuO systems indicate that the cationic species Ru⁴⁺ and Cu²⁺ were highly dispersed and diluted in the lattice sites of TiO₂. Therefore, no diffraction peak corresponding to RuO₂ or CuO was observed in the XRD pattern. We believe that due to the similar ionic radii of Ru⁴⁺ and Ti⁴⁺ RuO₂ and TiO₂ existed in the same crystal structure, and the substitution between RuO₂ and TiO₂ was feasible than in any other systems. The average crystallite size of TiO₂/RuO₂ and TiO₂/RuO₂/CuO in the mesoporous materials were calculated by using Scherrer equation⁵⁷ and shown in Table1. Dislocation densities were determined from Williamson and Smallman's formula⁵⁸ and shown in Table.1. The addition of CuO in the titanium dioxide matrix slightly affected the crystallographic parameters. These results were adequately confirmed further through the SEM and BET analysis.

Catalyst	Average Grain Size (nm)	Dislocation Density ($\delta \times 10^{16} \text{m}$)	BET surface area (m^2/g)	Pore volume (cm^3/g)	Average pore diameter (nm)
TiO₂	22.59	0.20	43.8	0.1	16.4
TiO₂/RuO₂ 0.5%	20.41	0.24	39.5	0.1	18.9
TiO₂/RuO₂/CuO 0.05%	18.76	0.28	39.7	0.06	3.9
TiO₂/RuO₂/CuO 0.1%	18.72	0.29	48	0.05	3.5
TiO₂/RuO₂/CuO 0.5%	23.51	0.18	49.5	0.01	4.4
TiO₂/RuO₂/CuO 1%	19.98	0.25	53	0.08	3.9

Table.1. Average grain size, dislocation density, and the BET results of mesoporous TiO₂/RuO₂ and mesoporous TiO₂/RuO₂/CuO nanomaterials

^a average grain size calculated by applying the Scherrer equation

^b dislocation density calculated by using Williamson–Smallman’s formula

^c surface area determined by applying the Brunauer–Emmett–Teller (BET) equation to a relative pressure (P/P_0) range of 0.05–0.35 of the adsorption isotherm.

^dcalculated from the Barrett–Joyner–Halenda (BJH) equation using the desorption isotherm

4.3.3 BET analysis

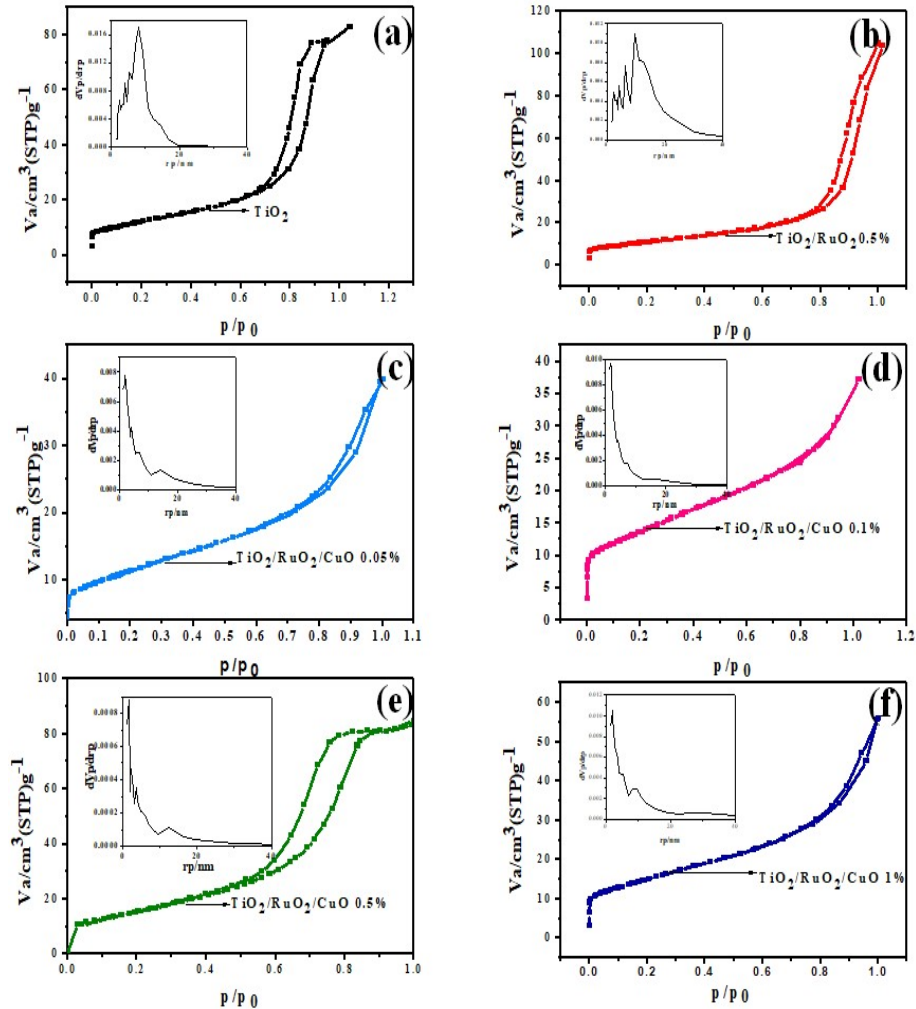


Figure 4.3 N_2 adsorption-desorption isotherms and BJH pore size distribution plots of mesoporous TiO_2 , mesoporous TiO_2/RuO_2 and mesoporous $TiO_2/RuO_2/CuO$ nanomaterials with different percentage composition of CuO (0.01, 0.05, 0.5 and 1 % respectively).

Figure 4.3 shows N₂ adsorption-desorption isotherms and Barret-Joyner-Halenda (BJH) pore size distribution plots of mesoporous TiO₂, mesoporous TiO₂/RuO₂ 0.5 % and mesoporous TiO₂/RuO₂/CuO 1 % nanomaterials. Both of the materials exhibited type IV adsorption-desorption isotherms. The hysteresis loop indicated that the material displays the characteristic feature of type IV isotherm with H3 type hysteresis for mesoporous material ⁵⁹. The N₂ adsorption-desorption isotherms of both materials showed a typical Type IV isotherm with monolayer adsorption at low values of relative pressures (P/P₀), followed by multilayer adsorption and capillary condensation step at a relative pressure of 0.62-1P/P₀ and 0.63-0.99 P/P₀ respectively. The presence of Type H3 hysteresis loop comprised of plate like particle aggregates forming slit like pores ⁶⁰⁻⁶¹.

The specific surface area calculated from the BET adsorption isotherm for TiO₂/RuO₂ is 40 m²/g. The incorporation of CuO on TiO₂/RuO₂ has dramatically influenced their surface area. The surface modification of the material with CuO has resulted in an increase of surface area. From textural property studies, it was evident that the average pore size of TiO₂, TiO₂/RuO₂, and TiO₂/RuO₂/CuO were in the mesoporous range. But there was a decrease in pore volume and average pore diameter of TiO₂/RuO₂/CuO nanomaterial. This shows that introduction of CuO has led to a remarkable change in the textural properties of the material. The textural properties, including specific surface area, pore volumes, and BJH pore diameters obtained for mesoporous TiO₂, TiO₂/RuO₂, TiO₂/RuO₂/CuO nanomaterials are summarized in Table .1

4.3.4 XPS studies

In photocatalysts, major contributions for its performance are essentially controlled by the electronic state or surface chemical state of ions in it, and in multicomponent compound systems, ionic substitution engenders variations in the valance state of each cation⁶². This has to be compared with similar elements features obtained from the x-ray photoelectron spectra (XPS). The XPS spectra were recorded and were further processed for the spectral components using CASA XPS and Peakfit41 software⁶³. The internal charge correction was depleted by setting C1s to 284.8 eV. The core level elemental spectra were detected for Ti2p, Ru3d, and O1s for the compound TiO₂/RuO₂ and Ti2p, Ru3d, Cu2p, and O1s for TiO₂/RuO₂/CuO compound respectively. The multiple oxidation states of these elements were investigated from the significant asymmetry of peak shapes of corresponding elements and those are fitted with a Gaussian/Lorentzian mixed function⁶⁴. Figures 4.4.1 and 4.4.2 represent the corresponding XPS spectra of elements Ti2p, Ru3d, and O1s distinguished from mesoporous TiO₂/RuO₂. As in figures, Ti2p spectra exhibited no significant peak asymmetry and hence are fitted with a single Gaussian-Lorentzian component. Meanwhile, Ru3d and O1s curves were fitted with their corresponding individual components. Similar features are recognized for Ti2p and Cu2p components in TiO₂/RuO₂/CuO with single components and multiple components for Ru3d and O1s. By recording a wide range survey scan the constituent elements are quantified in tables 2 and 3 as obtained from library results of CASA software. The atomic percentages of elements were

obtained from the area of curves under the different peak positions of prominent elements present in samples. These were tabulated and were well close to the composition we aimed to attain.

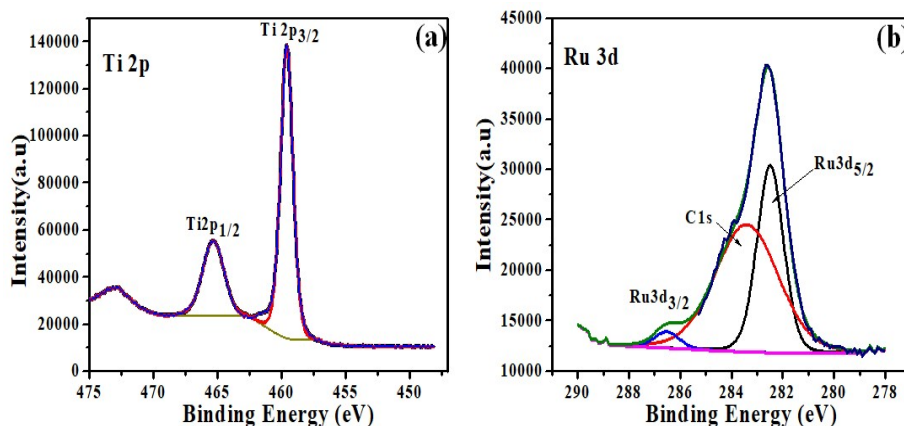


Figure 4.4 CoreLevel Elemental X-ray Photoelectron spectra of (a) Ti2p fitted with single Gaussian components showing valance stability (b) Ru3d in TiO₂/RuO₂ mesoporous nanomaterials

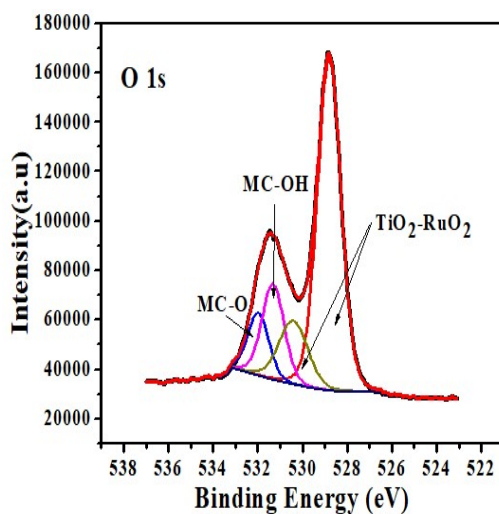


Figure 4.5 Core level Elemental X-ray Photoelectron spectra of O1s in TiO₂/RuO₂ mesoporous nanomaterials

Figure 4.4 enclosed two plots, strong and intense Ti2p emissions coupled with Ti2p_{3/2} and Ti2p_{1/2} components (Figure 4.4(a)) and a low-intensity Ru3d asymmetric curve fitted with Ru3d_{3/2} and Ru3d_{5/2} components (Figure 4.4(b)). The elemental photoelectron emissions Ti2p and Ru3d give rise to two different possible energy states for the same level established as the spin-orbit j-j coupling⁶⁴. Ti2p_{3/2} situated at 459.58 eV and Ti2p_{1/2} at 465.28 eV, were fitted with single Gaussian-Lorentzian established formation another chemical state or sub-oxides⁶⁵. Referring to previous results, the typical peak difference (ΔV) between Ti2p split states is 5.7 eV is exactly reproduced here⁶⁶. Pure TiO₂ exhibits peaks 458 and 464 eV⁶⁷. The variation in the TiO₂ peak implies the existence of the interaction and electron transfer between TiO₂ and RuO₂⁶⁸. Ru3d emission in the TiO₂/RuO₂ (Figure 4.4(b)) appeared between 278 eV to 287 eV is an integral peak inclusive of a minimum number of three emissions probably arise from Carbon (C1s) and the split components of Ru3d (Ru3d_{3/2} and Ru3d_{5/2}). As in figure Ru3d_{3/2} at 286.53 eV and Ru3d_{5/2} at 282.48 eV was resolved with spin-orbit split ($\Delta V=4.05$ eV), also consistent with references⁶⁹⁻⁷¹.

In multi-cation oxide systems, O1s spectra typically appear broad with visible peak shape asymmetry as a result of distinct ionic bonding with many cations, metal-carbonates, and hydroxyls that are naturally present in any compounds⁷². Figure 4.5, shows a broad O1s asymmetric curve obtained from TiO₂/RuO₂ system fitted with corresponding components. Herein, O1s pop up with a strong emission with shoulder peak. Both the emissions are considered as cumulative

and are well fitted with four components centered at 528.81 eV, 530.31 eV, 531.39 eV, and 532.03 eV. In TiO₂/RuO₂, the binding energy (B.E) positions 528.81 eV and 530.31 eV often correspond to the Metal-Oxygen (M-O) emissions and clearly here the only state is +4 state of cations with oxygen⁷³⁻⁷⁴. By virtue, carbonates will be present in all samples and the 532.03 eV component is assigned as metal-carbonate (M-C) bonded with oxygen and hydroxides (O-H) 531.39 eV⁷⁴. The presence of hydroxides is significant and this would create deviations in the calculated composition of compounds in a small fragment. TiO₂/RuO₂/CuO, narrow scan XPS maintain similar features to that of previous results with slightly shifted peak centers and an additional emission originated from copper. Figure 4a and 4b represents Ti2p and Ru3d emissions, as ascribed in the last paragraph both elements possess valance stability with symmetric doublets for Ti2p and well resolved doublets for Ru3d state. B.Es obtained here are located at 459.23 eV (Ti2p_{3/2}) and 465.13 eV (Ti2p_{1/2}) with meager stretch in j-j coupling constant ($\Delta V=5.9$ eV)⁷⁵. Meanwhile, Ru3d_{5/2} (281.73 eV) and Ru3d_{3/2} (285.77 eV) the coupling constant $\Delta V=4.04$ eV was well in agreement with other sample. The formation of the ternary nano-mesoporous compound slightly affected the B.E positions Ti and Ru ions.

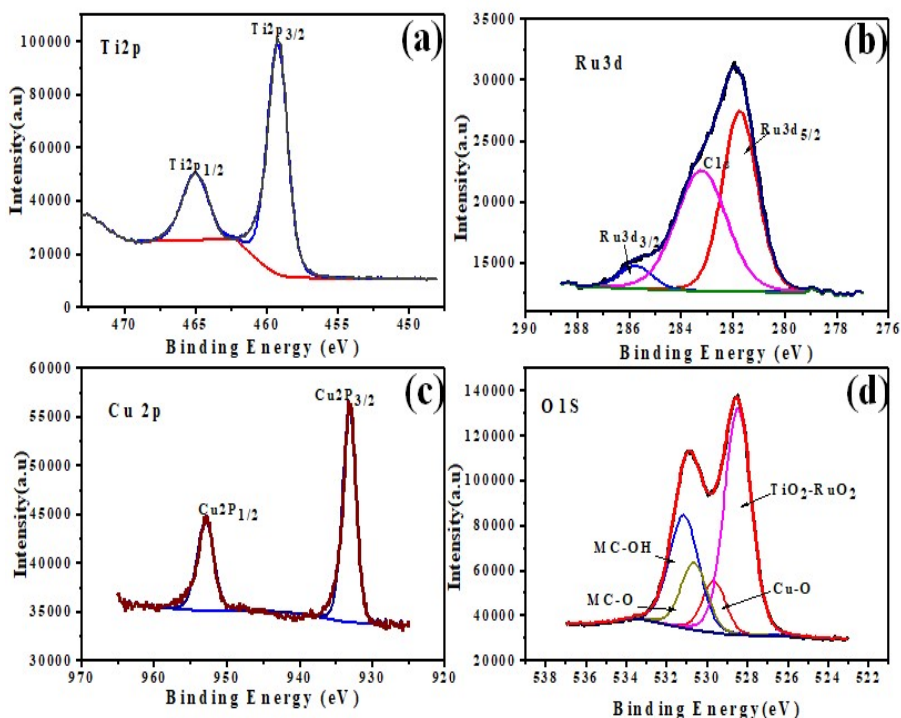


Figure 4.6 Core level Elemental X-ray Photoelectron spectra of (a) Ti2p fitted with single Gaussian components (b) Ru3d asymmetric curve fitted for multiple components (c) Cu2p fitted with single Gaussian components (d) O1s asymmetric peak fitted for multiple components in mesoporous TiO₂/RuO₂/CuO nanomaterial

Cu2p in Figure 4.6(c) the doublets in 933.16 eV and 952.94 eV, are respectively of Cu2p_{3/2} and Cu2p_{1/2} split ups with no trace of satellite peak. It can be a remark for the Cu²⁺ electronic state alongside the propitious peak-shape. $\Delta V=19.78$ eV, additionally a consistent result with other reports⁷⁶. In O1s spectra (Figure 4.6(d)), the shoulder peak turned stronger than the previous one, roughly O1s were an aggregate of two intense broad emissions. Lower binding energy position, 528.48 eV, and 529.69 eV assigned to 4⁺-O (Ti-Ru-O) bindings and Cu²⁺-O binding⁷⁶. The other two peaks were metal-carbonate (M-C) bonded with oxygen and hydroxides as discussed previously.

Name	Position (eV)	FWHM (eV)	At%
Ti2p	459.08	2.57	22.45
Ru3d	286.08	3.59	3.28
O1s	531.08	4.47	74.26

Table.2. XPS fitting parameter obtained from the survey scan of TiO₂/RuO₂ 0.5% and the atomic percentages obtained from it

Name	Position(eV)	FWHM(eV)	At%
Ti2p	459.08	2.57	20.46
Ru3d	286.08	3.59	2.92
O1s	531.08	4.47	75.37
Cu2p	933.08	2.85	1.25

Table.3. XPS fitting parameter obtained from the survey scan of TiO₂/RuO₂/CuO 1% and the atomic percentages obtained from it

4.3.5 SEM studies

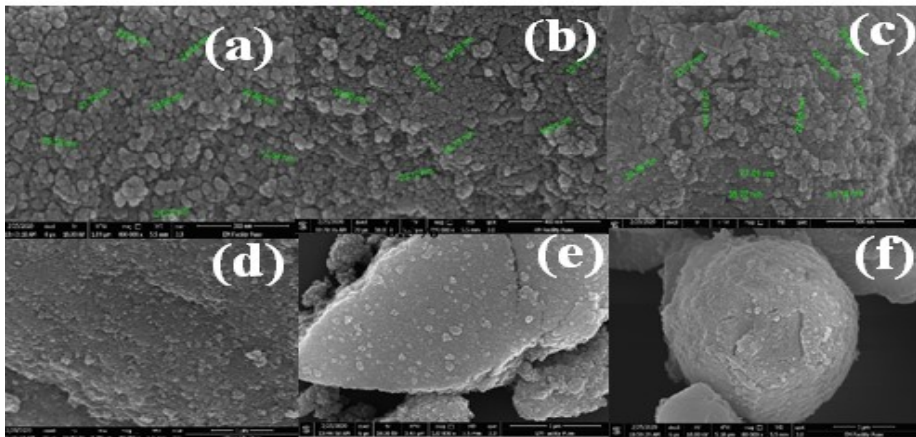


Figure 4.7 Low magnification SEM images of (a) mesoporous TiO₂ (b) SEM mesoporous TiO₂/RuO₂ 0.5 % (c) mesoporous TiO₂/RuO₂/CuO 1 % and higher magnification SEM images of (d) mesoporous TiO₂ (e) mesoporous TiO₂/RuO₂ 0.5 % (f) mesoporous TiO₂/RuO₂/CuO 1 %

In order to obtain information on morphology, structure, and mean particle size of the samples studied, FE-SEM analyses have been conducted. Figure 4.7 displays SEM micrographs of mesoporous $\text{TiO}_2/\text{RuO}_2$ and $\text{TiO}_2/\text{RuO}_2/\text{CuO}$ nanomaterials. Both the low magnification and high magnification SEM images have been displayed. The low magnification SEM analysis of $\text{TiO}_2/\text{RuO}_2$ (Figure 4.7(a)) and $\text{TiO}_2/\text{RuO}_2/\text{CuO}$ (Figure 4.7(b)) indicated the formation of huge spherical agglomerates which are of non-uniform size. The clustering seemed to be more pronounced in mesoporous $\text{TiO}_2/\text{RuO}_2$ and hence the structure appeared to be more compact. High magnification SEM image of $\text{TiO}_2/\text{RuO}_2$ (Figure 4.7(c)) and $\text{TiO}_2/\text{RuO}_2/\text{CuO}$ (Figure 4.7(d)) indicated the formation of flower-like nanospheres. The agglomeration of materials resulted in an irregular morphology. The SEM images revealed that both RuO_2 and CuO were grown homogeneously on the surface of mesoporous TiO_2 . The measurement of grain size was done through SEM analysis. All the samples consist of regular and irregular tiny spherical nanoparticles. The average particle size of spherical structures in mesoporous TiO_2 , $\text{TiO}_2/\text{RuO}_2$, and $\text{TiO}_2/\text{RuO}_2/\text{CuO}$ were 16 nm, 21 nm, and 35 nm respectively.

4.3.6 TEM studies

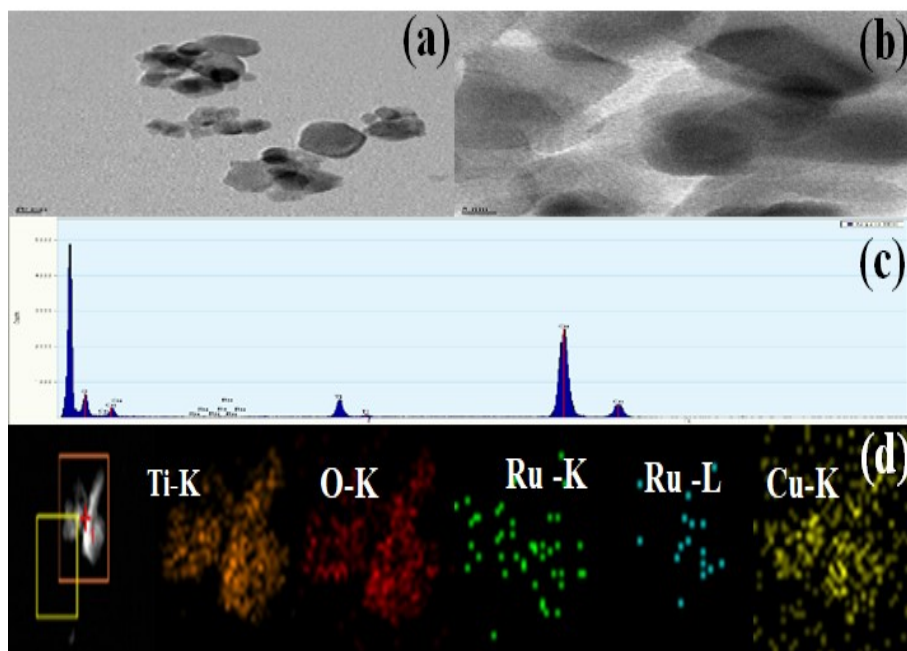


Figure 4.8 (a) and (b) HRTEM TEM images of mesoporous $\text{TiO}_2/\text{RuO}_2/\text{CuO}$ ternary nanosystem (c) EDS spectrum of mesoporous $\text{TiO}_2/\text{RuO}_2/\text{CuO}$ ternary nanosystem and (d) EDS elemental mapping images

The microstructural characteristics of the catalyst were investigated by transmission electron microscopy (TEM) using the energy dispersive x-ray spectroscopy (EDS). Figure 4.8 shows the TEM–EDS micrographs of the ternary mesoporous $\text{TiO}_2/\text{RuO}_2/\text{CuO}$ 1% nanosystem. The mapping of elements was performed on a randomly selected field. The results indicated the distribution states of Ti, O, Ru, and Cu elements for mesoporous $\text{TiO}_2/\text{RuO}_2/\text{CuO}$ 1% nanosystem. Several dark edges appeared on the $\text{TiO}_2/\text{RuO}_2/\text{CuO}$ substratum. They were believed to be the scattered form of RuO_2 ⁷⁷. Elemental mapping

of the $\text{TiO}_2/\text{RuO}_2/\text{CuO}$ further confirmed the existence of widely distributed Ru and Cu organisms on the surface of TiO_2 . The peaks of Ti, Ru, O are visible in the spectrum.

4.3.7 PL studies

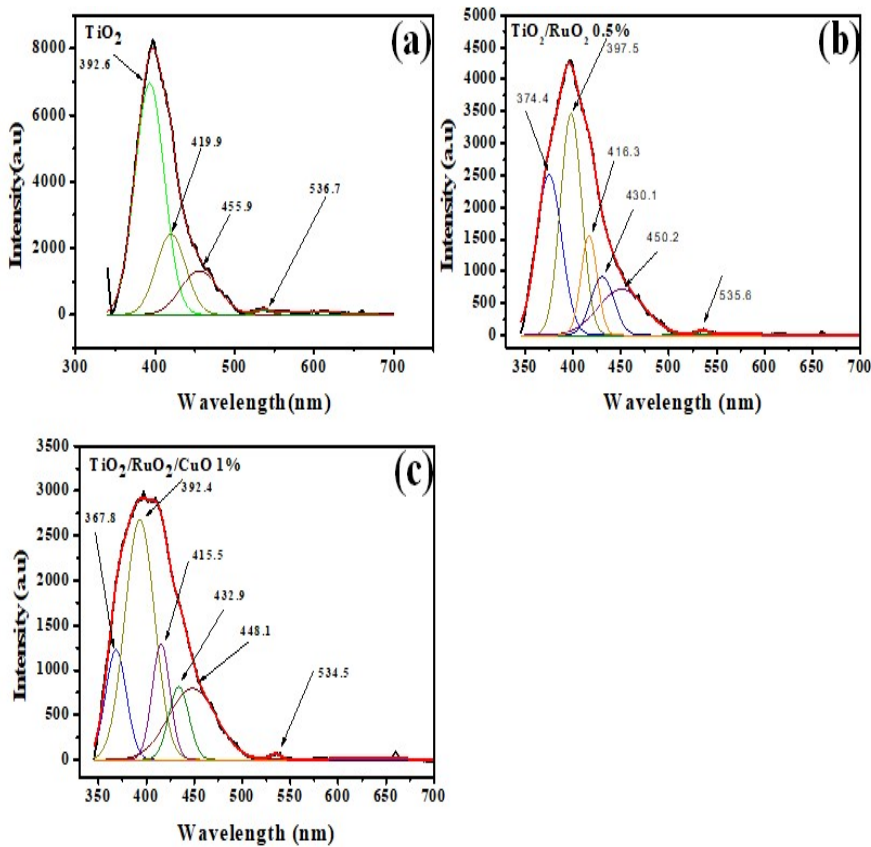


Figure 4.9 Photoluminescence spectra of mesoporous a) TiO_2 b) $\text{TiO}_2/\text{RuO}_2$ and c) $\text{TiO}_2/\text{RuO}_2/\text{CuO}$ 1 %

PL measurements were carried out with an excitation wavelength of 330 nm and the emission spectrum was monitored in the range from 345 to 700 nm (Figure 4.9). The initial task on the spectra was to fit the

broad intense emissions between 350-530 nm into corresponding emissions originated from various transitions of valence band to the conduction band and vice versa. The deconvolutions in PL illustrated corresponding bands. The surface modification of TiO₂ with RuO and CuO has resulted in an appreciable change in the PL emission spectra of TiO₂/RuO₂ and TiO₂/RuO₂/CuO nanomaterials. The deconvoluted PL spectra of TiO₂/RuO₂ analyses indicated the main PL emission peak at 398 nm and shoulder peaks at 374, 416, 430, 450 nm. In the case of TiO₂/RuO₂/CuO nanomaterial, the dominant peak was observed at 392 nm and the shoulder peaks were found at 368, 416, 433, and 448 nm. This indicated that the position of the PL peak is slightly shifted to the violet region. The emission of intermediate band transmission of titanium dioxide was responsible for the shoulder peak around 370 nm⁷⁸. The emission peak around 398 nm was obtained due to the direct transition of energy from the conduction to valence band⁷⁷⁻⁷⁹. The peak around 416 nm and 536 nm was due to the self-trapped excitons that are being located on TiO₆ octahedral⁸⁰. The emission peak around 430 nm can be attributed to the electron transmission being facilitated by defect levels in the band gap like the formation of oxygen vacancies during the synthesis of samples⁸¹. The shallow trap level due to the oxygen vacancy accounts for the emission peak around 450 nm⁸²⁻⁸³. The PL intensity of TiO₂/RuO₂/CuO is suppressed on comparison to TiO₂/RuO₂ and TiO₂. The introduction of Cu into the structure of TiO₂ doped with Ru has created changes in its electronic structure. The lower PL intensity for TiO₂/RuO₂/CuO nanocomposite suggested reduced recombination and efficient electron-hole separations in the compound.

4.4 Conclusion

We successfully synthesized mesoporous TiO₂, binary mesoporous TiO₂/RuO₂, and ternary mesoporous TiO₂/RuO₂/CuO nanomaterials by surfactant-assisted sol-gel method. The X-ray diffraction patterns are intact with the TiO₂ anatase phase with the presence of rutile TiO₂. Calculations on grain size affirm nano-crystalline growth in 3-dimensions and scanning electron micrographs complemented the results of XRD, besides the growth of dense particles in different shape well in the nano regime is distinguished from it. TEM images further revealed the presence of Ti, Ru, Cu, and O₂ in the nanostructure. Brunauer–Emmett–Teller (BET) adsorption-desorption technique results indicated the formation of mesoporous structure with surface area 53 m²/g, pore volume 0.08 cm³/g and average pore diameter 3.9 nm. X-ray photoemission survey spectroscopy elucidated the presence of constituent elements in the samples and that was in the expected composition. This supported the results of XRD depicting the substitution of Ru/Cu ions in the TiO₂ matrix without affecting the overall crystal symmetry. The elemental scan processed with surface analysis software recite the presence of elements as well as the possible chemical states, Ru⁴⁺, Ti⁴⁺, and Cu²⁺ ionic states were identified from the studies and peak analysis on O1s spectra delineate those interpretations on XPS elemental scan. The UV-Vis diffuse reflectance analysis showed that the introduction of RuO₂ and to the nanosystem resulted in the redshift of absorbance spectra. From PL studies it was clear that the introduction of RuO₂ and CuO to mesoporous TiO₂ promoted the separation of photogenerated charges.

REFERENCES

1. Nakata K, Fujishima A, *Journal of Photochemistry and Photobiology C: Photochemistry Reviews*, 2012, 13, 169-189.
2. Bhogaita M, Yadav S, Bhanushali A.U, Parsola A.A, Nalini R.P, *Materials Today: Proceedings*, 2016, 3, 2052-2061
3. Wang B, Shen S, Mao S.S, *Journal of Materiomics*, 2017, Doi: 10.1016/j.jmat. 2017. 02.001.
4. Dhakshinamoorthy A, Navalon S, Corma A, Garcia H, *Energy Environ. Sci.*, 2012, 5, 9217-9233
5. Tahir K, Ahmad A, Li B, Nazir S, Khan A.U, Nasir T, Khan Z.U.H, Naz R, Raza M, *Journal of Photochemistry and Photobiology B: Biology*, 2016, 162, 189-198
6. Karlsson K.B, Cornel A, Pettersson L.G.M, *Electrochimica Acta*, 2015, 180, 514-527
7. Khan M. I, Bhatti K. A, Qindeel, Althobaiti H. S, Alonizan N, *Results in Physics*, 2017, 7, 1437-1439
8. Hou H, Shang M, Gao F, Wang L, Liu Q, Zheng J, Yang Z, Yang W, *ACS Appl. Mater. Interfaces* 2016, 8, 20128–20137
9. Shang M, Hou H, Gao F, Wang L and Yang W, *RSC Adv*, 2017, 7, 30051-30059
10. Uddin M.T, Babot O, Thomas L, Olivier C, Redaelli M, Arienzo M.D, Morazzoni F, Jaegermann W, Rockstroh N, Junge H, Toupance T, *Journal of Physical Chemistry C*, 2015, 119, 7006-7015
11. Wang Y, Sun C, Zhao X, Cui B, Zeng Z, Wang A, Liu G, Cui H, *Nanoscale Res Lett*, 2016, 11, 529
12. Lin C, Song Y, Cao L, Chen S, *Journal of the Chinese Advanced Materials Society* 2013, 1, 188–199
13. Pal B, Sharon M, Nogami G, *Materials Chemistry and Physics* 1999, 59, 254-261
14. Meng A, Zhu B, Zhong B, Zhang L, Cheng B, *Applied Surface Science*, 2017, 422, 518-527

15. Srinivasan S.S, Wade J, Stefanakos E.K, Journal of Nanomaterials, 2006, DOI 10.1155/JNM/2006/87326
16. Deshapriya I.K, Kim C.S, Novak M.J, Kumar C.V, ACS Appl. Mater. Interfaces 2014, 6, 12, 9643–9653
17. Over H, Electrochimica Acta , 2013, 93, 314-333
18. Pascuzzi M.E.C, Goryachev A, Hofmann J.P, Emiel J.M, Hensen E.J.M, Applied Catalysis B: Environmental, 261, 2020, 118225
19. Lu P, He S, Li F.X, Jia Q.X, Thin Solid Films 1999, 340, 140–144
20. Colomer M.T, Jurado J.R, Chem. Mater, 2000, 12, 923–930
21. Over H, Chem. Rev, 2012, 112, 3356–3426
22. Zhitomirsky I, Journal of Materials Science, 1999, 34, 2441–2447
23. Kawai T, Sakata T, CHEMICAL PHYSICS LETTERS, 1980, 75, 341-344
24. Nada A.A, Hamed H.A, Barakat M.H, Mohamed N.R, Veziroglu T.N, International Journal of Hydrogen Energy, 2008, 33, 3264-326
25. Neupane S, Kaganas G, Valenzuela R, Kumari L, Wang X.W, Li W.Z, Journal of Materials Science , 2011, 46, 4803-4811
26. Lokhande C.D, Park B.O, Park H.S, Junga K.D, Joo O.S, 2005, 105, 267-274
27. Minero C, Lorenzi E, Pramauro E, Pelizzetti E, Inorganica Chimica Acta, 91, 1984, 301-305
28. Kuang M, Wang Y, Fang W, Tan H, Chen M, Yao J, Liu C, Xu J, Zhou K. Yan Q, Adv. Mater, 2020, 32, 2002189
29. Colon G, Maicu M, Hidalgo M.C, Navio J.A, Applied Catalysis B: Environmental, 2006, 67, 41–51
30. Ghadikolaie S.S, Hosseinzadeh K, Ganji D.D, Journal of Molecular Liquids, 2018, 272, 226-236
31. He X, Zhang G, Wang X, Hang R, Huang X, Qin L, Tang B, Zhang X, Ceramics International, 2017, 43, 16185-16195

32. Chauhan M, Sharma B, Kumar R, Chaudhary G.R, Hassan A.A and Kumar S, *Environmental Research*, 2019, 168, 85-95
33. Saif S, Tahir A, Asim T, Chen Y, *Nanomaterials*, 2016, 6, 205
34. Yang L, Jiang Z, Lai S, Jiang C, Zhong H, *International Journal of Chemical Engineering*, 2014, Doi.org/10.1155/2014/691562
35. Kim E. Y, Kim D.S, Ahn B.T, *Bull. Korean Chem. Soc.* , 2009, 30, 193-196
36. Zhou W, Li W, Wang J.Q, Qu Y, Yang Y, Xie Y, Zhang K, Wang L, Fu H, Zhao D, *J. Am. Chem. Soc.*, 136, 2014, 9280–9283
37. Bastakoti B.P, Salunkhe R.R, Jinhua Y, Yamauchi Y, *Phys. Chem. Chem. Phys.*, 2014, 16, 10425-10428
38. Rahimnejad S, Setayesh S.R, Gholami M.R, *J. Iran. Chem. Soc.*, 5, 2008, 367-374
39. Bardhan M, Misra T, Chowdhury J, *Chem Phys Lett* 2009, 481, 142–148
40. Ricardo N.M.P. S, Ricardo N.M.P. S, Costa F de M.L. L, Chaibundit C, Portale G, Merinod D.H, Burattinid S, Hamley I. W, Muryn C.A, Nixon S.K, Yeates S.G, *J Colloid Interface Sci* 2011, 353, 482–489
41. Chen R, Trieu V, Natter H, Stowe K, Maier W.F, Hempelmann R, Bulan A, Kintrup J, Weber R, *Chem. Mater*, 2010, 22, 6215–6217
42. Guglielmi M, Colombo P, Rigato V, *Electrochem. Soc*, 1992, 139, 1655-1661
43. Malek J, Watanabe A, Mitsuhashi T, *Journal of Thermal Analysis and Calorimetry*, 2000, 60, 699–705
44. Panic V, Dekanski A, *Materials and Manufacturing Processes*, 2005, 20, 89-103
45. Swider K.E, Merzbacher C.I, Hagans P.L, Rolison D.R, *Chem. Mater*, 1997, 9, 1248-1255
46. Mousli F, Chaouchi A, Jouini M, Maurel F, Kadri A, Chehimi M.M, *Catalysts*, 2019, 9, 578

47. Park S, Shin D, Yeo T, Seo B, Hwang H, Lee J, Choi W, *Chemical Engineering Journal*, 2020, 384, 123269
48. Shi Q, Ping G, Wang X, Xu H, Li J, Cui J, Abroshan H, Ding H and Li G, *J. Mater. Chem. A*, 2019, 7, 2253-2260
49. Perazolli L, Nunez L, Silva M.R.A, Pegler G.F, Costalonga A.G.C, Gimenes R, Kondo M.M, Bertochi M.A.Z *Materials Sciences and Applications*, 2011, 2, 564-571
50. Cui X, Zhou J, Ye Z, Chen H, Li L, Ruan M, Shi J, *Journal of Catalysis* 2010, 270, 310–317
51. Nguyen-Phan T.D, Luo S, Vovchok D, Llorca J, Sallis S, Shyam Kattel, Xu W, Piper L.F.J, Polyansky D.E, Senanayake S.D, Stacchiola D.J, and Rodriguez J.A, *Phys. Chem. Chem. Phys*, 2016, 18, 15972-15979
52. Ashok A, Raman K, Masilamani S.A, Bose R.S.C, *Rasayan J. Chem*, 2018, 11, 53-62
53. Yoong L.S, Chong F.K, Dutta B.K, *Energy*, 34, 2009, 1652–1661
54. Fernandes F.R.D, Pinto F.G.H.S, Lima E.L.F, Souza L.D, Caldeira V.P.S and Anne G. D. Santo, *Appl. Sci.* 2018, 8, 725
55. Paul S, Choudhury. A, *Appl Nanosci*, 2014, 4, 839–847
56. Liu G, Yang H.G, Pan J, Yang Y.Q, Lu G.Q, Cheng H.M, *Chem. Rev*, 2014, 114, 9559–9612
57. Samb-Joshi K.M, Sethi Y.A, Ambalka A.A, Sonawane H.B, Rasale S.P, Panmand R.P, Patil R, Kale B. B, Chaskar M.G, *J. Compos. Sci.* 2019, 3, 90
58. Begum A, Hussain A, Rahman A, Beilstein J. *Nanotechnol*, 2012, 3, 438–443.
59. Sing K.S.W, *Pure & Appl Chem*, 1985, 57, 603—619
60. Zhelin W, Xuwei J, Mao P and Yongmin S, *Minerals*, 2020, 10, 377
61. Leofanti G, Padovan M, Tozzola G, Venturelli B, *Catalysis Today*, 1998, 41, 207-219

62. <https://srdata.NIST.gov/XPS/Default.aspx>
63. Luo, *Nanotechnology*, 2016, 27, 434002
64. Biesinger M, C, Payne B.P, Grosvenor A.P, Lau L.W.M, Gerson A.R, *Applied Surface Science*, 2011, 257, 2717-2730
65. Bond G.C, Flamerz S, *Appl. Catalysis*, 1989, 46, 89-102
66. Gonbeau D, Guimon C, Pfister-Guillouzo G, Levasseur A, Meunier G, Dormoy R, *Surf. Sci*, 1991, 254, 81 -89
67. Jia T, Fu F, Yu D, Cao J, Sun G, *Applied Surface Science* 430, 2018, 438–447
68. Divya K. S, Xavier M.M, Vandana P. V, Reethu V. N, Suresh Mathew, *New J. Chem.*, 2017, 41, 6445-6454
69. Shen J.Y, Adnot A., Kaliaguine S, *Appl. Surf. Sci.* , 1991, 51, 47-60
70. Jayaram P, Pradyumnan P. P, Karazhanov S.Z, 2016, 501, 140-145
71. Felthouse T.R., Fraundorf P.B., Friedman R.M., Schosser C.L, *J. Catal.*, 1991, 127, 421-444
72. Venezia A.M., Bertoncello R, Deganello G. *Surf. Interface Anal.* 23, 1995, 239 -247
73. Taylor J.A., Perry D.L, *J. Vac. Sci. Technol. A*, 1984, 2, 771 -774
74. Sivastava S., Badrinarayanan S., Mukhedkar A.J, *Polyhedron*, 1985, 4, 409-414
75. Patscheider J, Mebrahtu T, Cocke D.L, Wright R.B, Naugle D.G, *Appl. Surf. Sci.* , 1992, 59, 69-78
76. Baddorf A.P., Wendelken J.F, *Surf. Sci.* 1991, 256, 264-271
77. Shi J, Hui F, Yuan J, Yu Q.W, Mei S, Zhang Q, Li J, Wang W, Yang J, Lu J, *Catalysts* 2019, 2, 108
78. Giahi M, Pathania D, Agarwal S, Alid G.A.M, Chong K.F, Gupta V.K, *Studia Ubb Chemia*, 2019, 1, 7-18
79. Sinthiya M.M.A, Kumaresan N., Ramamurthi, K, *Bull Mater Sci*, 2019, 42, 127

80. Chang Y.M, Ming J, 2010, 10, 1647-1651
81. Zhao Y, Li C, Liu X, Gu F, Jiang H, Shao W, Zhang L, He Y, Materials Letters, 2010, 61, 79-83
82. Saha A, Moya A, Kahnt A, Iglesias D, Marchesan S, Wannemacher R, Prato M, Vilatel J.J, Guldi D.M, Nanoscale, 2017, 9, 7911-7921
83. Wu Z, Wang Y, Sun L, Mao Y, Wang M, Lin C, J. Mater, J. Mater. Chem. A, 2014, 2, 8223-8229

CHAPTER 5

PHOTOCATALYTIC H₂ EVOLUTION USING TiO₂/RuO₂/CuO TERNARY NANOSYSTEM

Contents

5.1 Introduction

5.2 Experimental methods

5.3 Results and discussion

5.4 Photocatalytic water splitting studies

5.4.1 Parameter effects

5.4.1.1 Effect of catalyst

5.4.1.2 Effect of catalyst weight

5.4.1.3 Effect of concentration of CuO

5.4.1.4 Effect of amount of sacrificial agent

5.4.1.5 Effect of chain length of alcohols

5.4.1.6 Effect of different sacrificial agents

5.5 Recycling experiments

5.7 Mechanism of photocatalytic water splitting reaction

5.8 Conclusion

5.1 Introduction

For the last few decades, the energy demand of human beings has been completely satisfied by fossil fuels. The depletion of the world's nonrenewable energy resources like coal and petroleum has led to the need for an alternative for energy production. H₂ is a promising candidate of fuel for future generation because of the interesting features like plentifulness of sources, different storage facilities, conversion into various other fuel forms, ease of transportation to long-distance, free of pollution etc¹⁻². It was Honda and Fujishima who have done the pioneering work on the production of H₂ by photodecomposition of water using electrolysis cell³. There are various approaches for H₂ production starting from water i.e., electrolysis⁴, thermochemical water splitting⁵, photoelectrolysis⁶, and photocatalytic water splitting⁷. Photocatalytic water splitting seems to be one of the most efficient methods for H₂ generation. Many factors account for the preference of photocatalytic water splitting process over thermochemical and photobiological water splitting process. The cost effectiveness, high efficiency, separation of H₂ and O₂ streams, and appropriate size of the reactor make the photocatalytic water splitting process dominant over the other processes⁸⁻⁹. As sunlight and water are renewable energy sources their conversion into H₂ seems to be an effective solution for the existing energy crisis. Thus, H₂ production from the photocatalytic water splitting process proves to be an ecofriendly process, H₂ being produced from sunlight and water that are renewable sources.

Nanostructured TiO₂ plays a prominent role in H₂ production through photocatalytic water splitting process in a cost effective and ecofriendly approach¹⁰. On illuminating the semiconducting photocatalyst with light, initially, electron-hole pairs are generated which is being followed by separation of charges and consequent surface reaction resulting in the production of H₂ and oxygen. Though TiO₂ possesses various attractive features like excellent chemical resistance, low cost, nontoxicity, availability, and resistance to photochemical corrosion, some of the limitations like rapid electron-hole recombination, incapability to utilize visible light because of large band gap restricts its application in visible light region¹¹⁻¹³. Many efforts have been tremendously taken by scientists to make TiO₂ sensitive to visible light. Doping TiO₂ with metals or nonmetals is one among them. The dopant helps to reduce the electron-hole recombination and lower the band gap by increasing the valence band edge without lowering the conduction band¹⁴⁻¹⁶. The photocatalytic activity can also be improved by modifying the structure of TiO₂ using structure-directing agents that enables light harvestment, adsorption of reactant molecule on the surface and intraparticle transfer of molecules through the ordered mesopore channels¹⁷⁻¹⁹. Another approach for improving the photoresponse of TiO₂ to the visible region is the sensitization of conventional TiO₂ with organic dyes²⁰⁻²¹. The limitation of photocatalyst caused by the electron-hole recombination and narrow photoresponse range can also be overcome by coupling with low band gap semiconductor²²⁻²³. The sacrificial agents also play a key role in improving the efficiency of photocatalyst²⁴.

A great deal of studies have been reported on binary semiconducting photocatalyst for water splitting and degradation of organic pollutants²⁵⁻²⁹. The formation of the potential gradient is responsible for the improvement of photocatalytic efficiency in such systems³⁰⁻³³. Further studies have reported the enhancement of photocatalytic activity by using ternary system³⁴⁻³⁶. In ternary nanocomposites efficiency of the photocatalyst is being improved by the formation of two heterojunctions that prevents electron-hole recombination by charge transfer between each semiconductors³⁷. Combining TiO₂ with Cu is one of the most promising strategies in the development of efficient photocatalytic systems³⁸⁻³⁹. Various researches have been conducted to explore the utilization of TiO₂/RuO₂ for improving the electrical and photocatalytic properties in the nanoscale⁴⁰⁻⁴³. In the previous chapter, we explored the synthesis and characterization of mesoporous TiO₂, mesoporous TiO₂/RuO₂, and mesoporous TiO₂/RuO₂/CuO nanosystem. Herein we report the photocatalytic water splitting application of mesoporous ternary TiO₂/RuO₂/CuO nanosystem in which a high-pressure 450W Hg lamp was used as the light source for irradiation.

The present study can be considered to be much effective for H₂ generation. Based on knowledge extension of TiO₂/RuO₂/CuO ternary nanosystem for photocatalytic water splitting has not yet been realized. Nevertheless, from our water splitting studies, it is established that the ternary mesoporous nanosystem TiO₂/RuO₂/CuO is highly efficient in energy generation via photocatalytic water splitting.

5.2 Experimental methods

The chemicals used for the preparation of mesoporous TiO₂, mesoporous TiO₂/RuO₂, and mesoporous TiO₂/RuO₂/CuO nano-materials, their suppliers, and the synthetic procedures were well explained in chapter 2. The various characterization measures that we have adopted were discussed in chapter 4.

5.3 Results and Discussion

The catalysts mesoporous TiO₂, mesoporous TiO₂/RuO₂, and mesoporous TiO₂/RuO₂/CuO were used for photocatalytic water splitting experiments under a 450 W high-pressure mercury lamp. The characterization techniques adopted are discussed in chapter 4.

5.4 Photocatalytic water splitting studies

We have performed a series of photocatalytic water splitting experiments using the prepared photocatalysts. The procedure of the hydrogen evolution via photocatalytic water splitting reaction was described in chapter 2. H₂ evolution was recorded by gas chromatogram. The experiment on water splitting reaction was conducted for 6 hours.

5.4.1 Parameter effects

5.4.1.1 Effect of Catalyst

The plot of photocatalytic H₂ evolution against time for TiO₂, TiO₂/RuO₂ 0.5%, TiO₂/RuO₂/CuO 1% mesoporous catalysts are represented in Figure 5.1. The H₂ production rate was found to

increase with time in all cases. Both the catalysts mesoporous TiO₂/RuO₂ 0.5 % and mesoporous TiO₂/RuO₂/CuO 1 % had greater photocatalytic activity than mesoporous TiO₂. The highest rate of H₂ production was found in mesoporous TiO₂/RuO₂/CuO 1 % nanocomposite. A maximum of 2.8 mmol of hydrogen was evolved with 5 mg of TiO₂/RuO₂/CuO 1 % mesoporous nanosystem. In the case of mesoporous TiO₂, H₂ evolution was comparatively lower due to the high electron-hole recombination. The introduction of RuO₂ and CuO on TiO₂ increased the rate of photocatalytic H₂ evolution as RuO₂ and CuO promoted electron-hole separation. The order of PL intensity was as follows, mesoporous TiO₂ > mesoporous TiO₂/RuO₂ 0.5 % > mesoporous TiO₂/RuO₂/CuO 1 %. The results of photocatalytic water splitting were consistent with this PL measurement. Mesoporous TiO₂/RuO₂ system showed better photocatalytic performance than TiO₂ but their performance was far inferior to that of mesoporous TiO₂/RuO₂/CuO 1%. The enhanced photocatalytic activity of mesoporous TiO₂/RuO₂/CuO 1 % can also be attributed to the reduction of the band gap. This argument was supported by the UV result. The UV results indicated the narrowing of the band gap on introducing CuO and RuO₂ on TiO₂ that enabled them to utilize the visible light. The band gap of mesoporous catalysts i.e., TiO₂, TiO₂/RuO₂ 0.5 % and TiO₂/RuO₂/CuO 1 % was 3, 2.9 and, 2.5 respectively. The increased surface area of mesoporous TiO₂/RuO₂/CuO 1 % was another factor that led to enhanced photocatalytic activity.

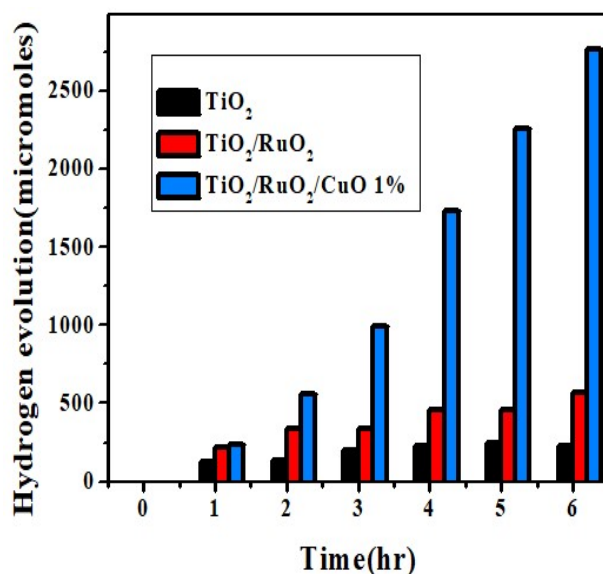


Figure 5.1: Performance of different photocatalysts towards water splitting

5.4.1.2 Effect of catalyst weight

The effect of catalyst weight on photocatalytic H₂ evolution was carried out by taking mesoporous TiO₂/RuO₂/CuO 1% in different amounts (0.0005 g, 0.005 g, 0.025 g, and 0.05 g) using 5 mL methanol as a sacrificial agent and 20 mL water. From Figure 5.2 shown below, it was observed that the photocatalytic H₂ evolution was found to increase on increasing the catalyst weight up to 0.025 g. Then there was a decrease in H₂ production on increasing the catalyst weight to 0.050 g. The maximum evolution of H₂ gas was observed when the catalyst weight was 0.025 g. About 105.15 mmol of H₂ evolution was observed with 0.025 g of the photocatalyst. The initial increase in H₂ evolution on increasing the weight of catalyst was due to the increase

Photocatalytic H₂ Evolution Using TiO₂/RuO₂/CuO Ternary Nanosystem
of photoexcitation centers. But the decrease in H₂ production on further increasing the weight of the photocatalyst was due to the opaqueness of the reaction mixture. The increase of mass of the catalyst resulted in the increase of scattering of light that consequently led to the loss of transparency of the reaction mixture. This resulted in the decrease of photocatalytic activity with increase in amount of catalyst loading.

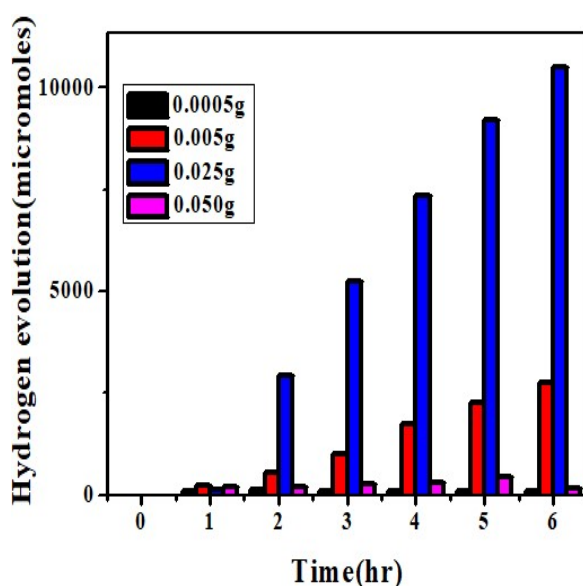


Figure 5.2: Effect of catalyst weight on H₂ evolution using mesoporousTiO₂/RuO₂/CuO 1% catalyst

5.4.1.3 Effect of concentration of CuO

The photocatalytic performances of catalysts were analyzed by conducting the experiments using different concentrations of CuO (0.05 %, 0.1 %, 0.5 % and 1 %) and keeping all other parameters constant. The results are provided in Figure 5.3. These results indicated that on increasing the concentration of CuO there was an increase in

photocatalytic H₂ evolution. The best photocatalytic performance was shown by mesoporous TiO₂/RuO₂/CuO 1 %. From the studies of the effect of concentration of CuO, it is confirmed that the presence of CuO is beneficial for the photocatalytic performance of ternary TiO₂/RuO₂/CuO nanosystem as doping with CuO improved visible light efficiency and reduced the electron-hole recombination. Both these factors contributed to the higher rate of H₂ production. These arguments are being supported by the UV and PL results.

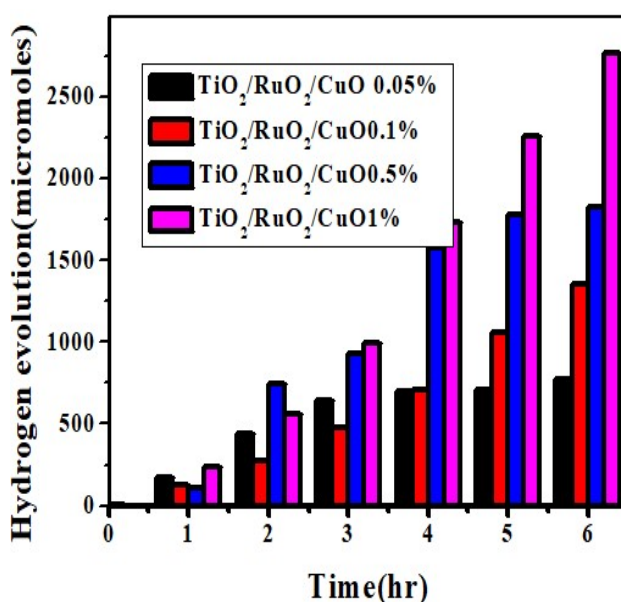


Figure 5.3: Effect of concentration of CuO on H₂ evolution

5.4.1.4 Effect of amount of sacrificial agent

The effect of the amount of sacrificial agents was studied by performing the photocatalytic water splitting reaction with 0.005 g mesoporous TiO₂/RuO₂/CuO 1 % varying the water-methanol ratio. The results obtained are summarized in Figure 5.4. A decrease in H₂

evolution was observed when the methanol, water ratio was increased from 1:4 to 4:1. When the concentration of the sacrificial agent increased the surface of active sites of the photocatalyst available for oxidation or reduction reactions may get blocked. Thus, increasing the concentration of the sacrificial agent resulted in the surface blocking of the catalyst that ultimately led to the decrease in photocatalytic performance. The enhanced H₂ evolution was observed when the water and methanol were maintained in the ratio 1:4.

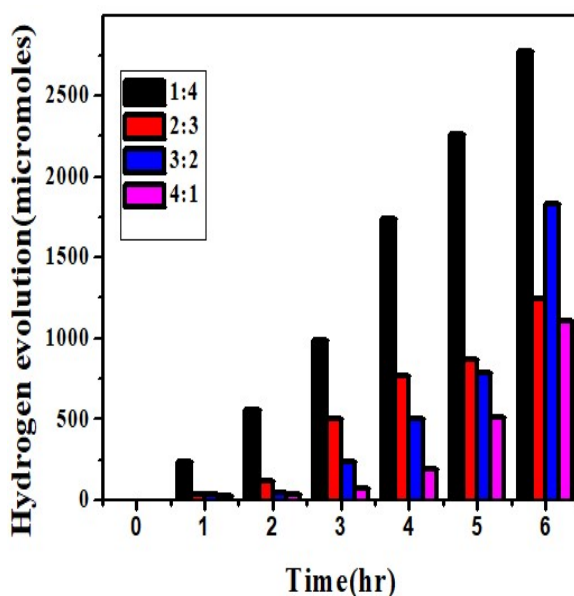


Figure 5.4: Effect of amount of sacrificial agent on H₂ evolution

5.4.1.5 Effect of chain length of alcohols

The photocatalytic water splitting reactions were carried out by varying the chain length of the sacrificial agent keeping all the other parameters constant (Figure 5.5). The H₂ production experiment was

Photocatalytic H₂ Evolution Using TiO₂/RuO₂/CuO Ternary Nanosystem
conducted by dispersing 0.005 g of mesoporous TiO₂/RuO₂/CuO 1% in 5 mL of various sacrificial agents (methanol, ethanol, propanol, and butanol) and 20 mL water. A decrease in photocatalytic H₂ evolution was observed on increasing the chain length of the sacrificial agent. The results on the effect of varying chain lengths of sacrificial agents are illustrated in Figure 5.5. The length of the carbon chain is one of the important features that decide the efficiency of H₂ production. In the case of short carbon chain sacrificial agents, CO is the main intermediate that gets adsorbed on the active site of the photocatalyst. The chemisorbed CO prevents further alcohol adsorption on the surface of TiO₂/RuO₂/CuO. The number of alpha hydrogens of the sacrificial agent decides the rate of conversion of CO to CO₂. Hydroxy radical by abstracting alpha hydrogen from the alcohol creates RCH₂-OH• radical that is oxidized into an aldehyde, carboxylic acid, and CO₂⁴⁴. The increase in chain elongation and the complexity of the higher alcohols results in steric hindrance that creates difficulty in carbon-carbon bond breaking. As formaldehyde formation involves carbon-carbon bond breaking, there was a profound decrease in photocatalytic activity on increasing the chain length of the sacrificial agent.

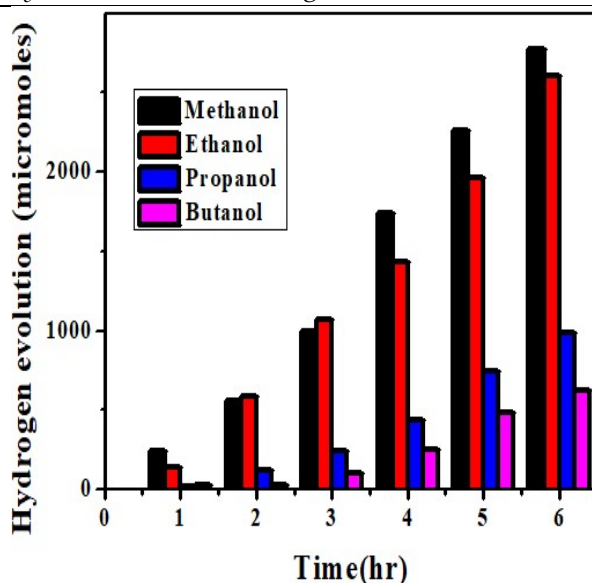


Figure 5.5: Effect of chain length on H₂ evolution

5.4.1.6 Effect of different sacrificial agents

The photocatalytic H₂ evolution was evaluated by carrying out the experiment using different sacrificial agents keeping all other parameters constant. The H₂ production was maximum when methanol was used as a sacrificial agent. This result can be attributed to the current doubling effect taking place when methanol is used as a sacrificial agent⁴⁵. The results obtained are provided in Figure 5.6. The higher photocatalytic activity in the case of ethylene glycol than triethanolamine is due to the faster charge transfer reaction that is being taking place in the TiO₂/RuO₂/CuO ethylene glycol system compared to the recombination of photogenerated electrons and holes.

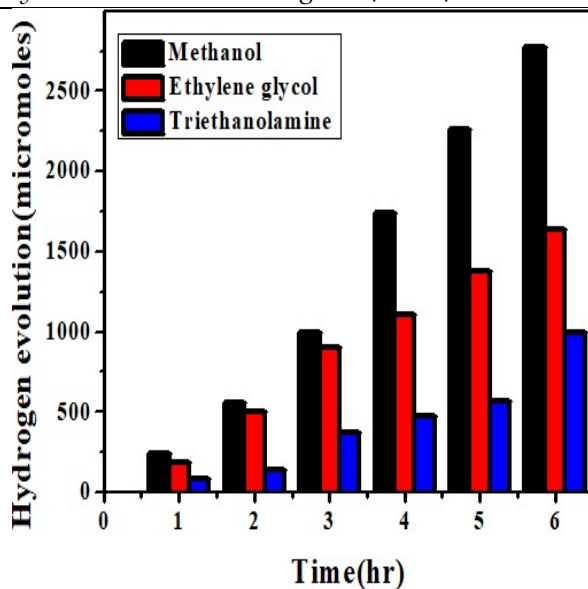


Figure 5.6: Effect of the different sacrificial agent on H₂ evolution

5.5 Recycling experiments

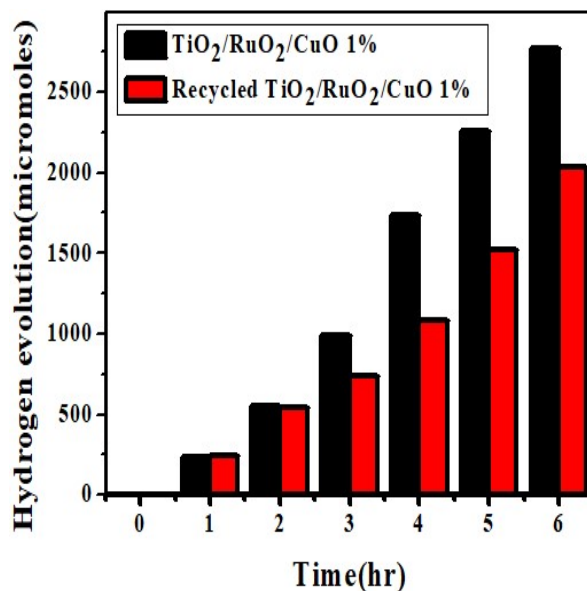


Figure 5.6: Recycling experiment using the photocatalyst mesoporous TiO₂/RuO₂/CuO 1 %

Photocatalytic water splitting experiments were performed for six hours by taking 5 mg of mesoporous TiO₂/RuO₂/CuO 1% and keeping all other parameters constant. The results obtained are illustrated in Figure 5.7. After that, the photocatalyst was centrifuged, washed with methanol, and dried. The evaluation of photocatalytic performance was done for the next six hours using the dried catalyst. For the first two hours, the results were concomitant with the previous results. But a gradual decrease in H₂ evolution was observed for the next four hours. This variation can be attributed to weight loss during the recycling experiment. A maximum evolution of 2.8 mmol of hydrogen was evolved in the first sixth hour and 2 mmol of H₂ was evolved in the next sixth hour.

5.6 Evaluation of H₂ evolution continuously for 18hrs

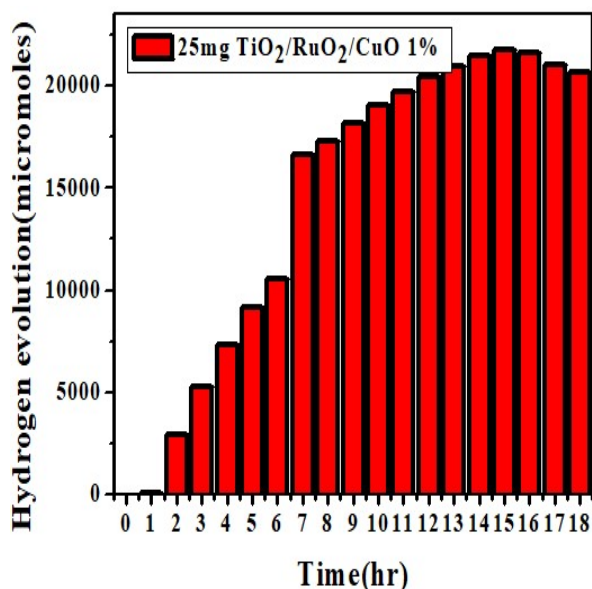


Figure 5.7: Photocatalytic water splitting experiment conducted continuously for 18 hours

Photocatalytic water splitting experiments were monitored continuously for 18 hours using 25 mg of TiO₂/RuO₂/CuO 1 %. The results obtained are presented in Figure 5.7. A maximum of 10.5, 20.4, and 20.7 mmol H₂ was evolved in the sixth, twelfth and eighteenth hours respectively. The H₂ production kept on increasing till the fifteenth hour, thereafter it started to decrease negligibly. The results of XPS and TEM of the photocatalyst before and after the water splitting reaction are represented in Figure 5.8 and 5.9. TEM images revealed the retention of the layered morphology in which Ru and Cu are homogeneously distributed on the surface of TiO₂ after the water splitting experiment. The X-ray photoelectron spectroscopy measurements of TiO₂/RuO₂/CuO before and after photocatalysis showed almost no shift in the peak position. This result ensures the retainment of catalyst composition before and after the photocatalytic water splitting reaction.

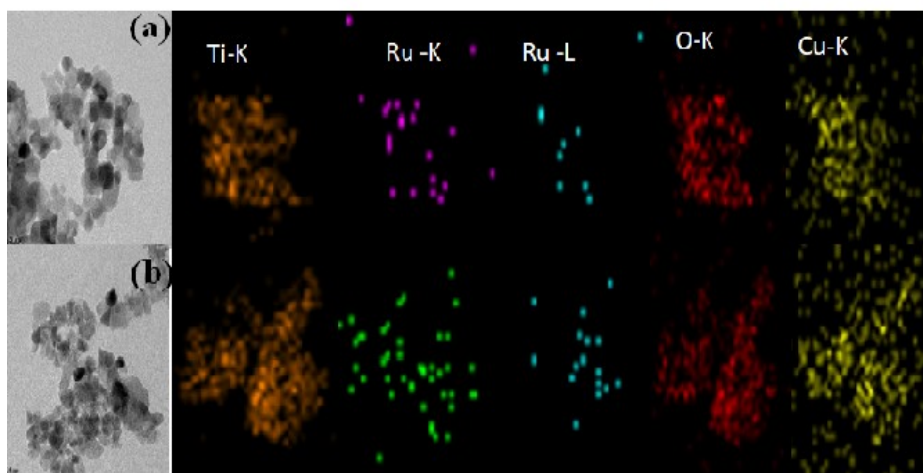


Figure 5.8: TEM results (a) before and (b) after photocatalytic water splitting reaction

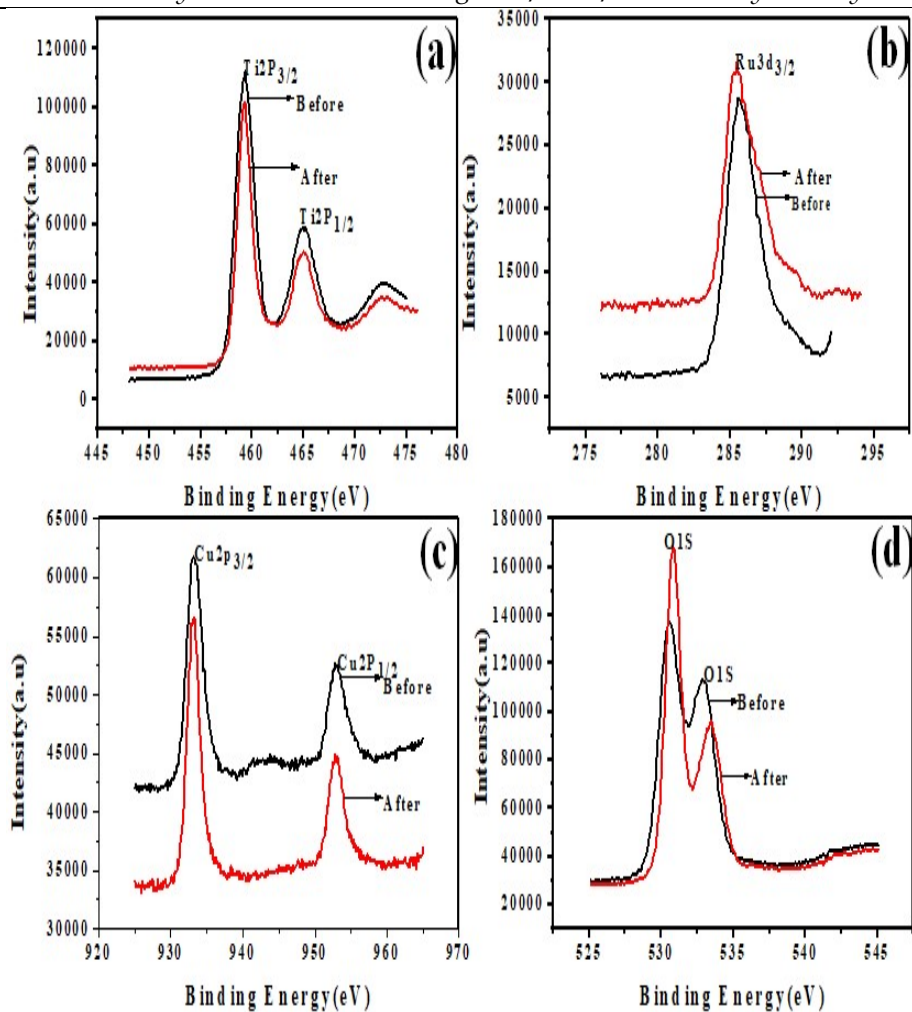


Figure 5.9: XPS results before and after photocatalytic water splitting reaction

5.7 Mechanism of photocatalytic water splitting reaction

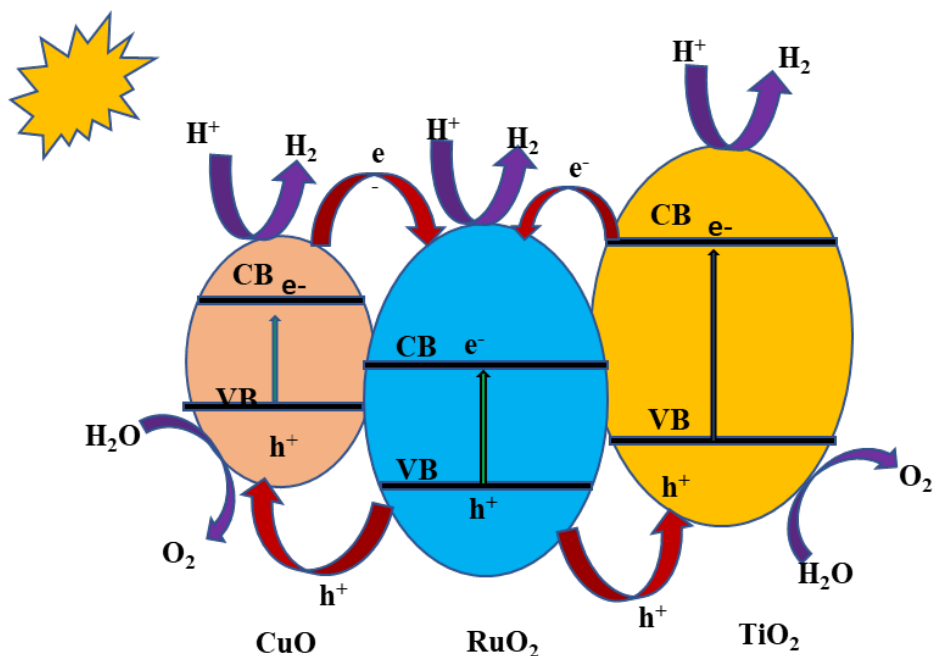


Figure 6: Mechanism of photocatalytic water splitting reaction using the catalyst mesoporous TiO₂/RuO₂/CuO 1 %

To understand the mechanism taking place in the Photocatalytic water splitting reaction the band edge positions of CuO, RuO₂, and TiO₂ were determined from previous reports⁴⁶⁻⁴⁷. It was observed that the appropriate position of valence band edge and conduction band edge of the photocatalysts allowed the easy transfer of charges between the photocatalysts. The interfacial charge transfer mechanism taking place in the mesoporous TiO₂/RuO₂/CuO ternary nanosystem is illustrated in Figure 6.

On irradiation with a high-pressure 450 W Hg lamp, photoexcitation occurs to TiO₂, CuO, and RuO₂ as they possess a narrow band gap. The

Photocatalytic H₂ Evolution Using TiO₂/RuO₂/CuO Ternary Nanosystem
photoexcitation creates holes in the valence band of CuO and RuO₂ and TiO₂. The conduction band edge potential of TiO₂ and CuO is more negative than that of RuO₂. Hence electrons are transferred from CuO and TiO₂ to RuO₂. At the same time holes are transferred from RuO₂ to CuO and TiO₂. This results in effective charge separation of the ternary system. Thus, the photocatalytic activity is improved to a large extent on the introduction of CuO and RuO₂ due to the suppression of electron-hole recombination. It is evident from the PL results. The conduction band edge position of RuO₂ and CuO is more positive than that of H₂. This disables RuO₂ and CuO to function as H₂ production centers. But the excess electrons produced on the conduction band of RuO₂ shifted their Fermi level towards negative potential⁴⁸. Thus, the surplus electrons at the surface of RuO₂ and CuO and TiO₂ reduce H⁺ to produce hydrogen. At the same time, hydroxyl radicals produced at the conduction band oxidizes water molecules to produce oxygen.

5.8 Conclusion

In our present work, we attempted to generate H₂ by photocatalytic water splitting process using mesoporous TiO₂, mesoporous TiO₂/RuO₂, and mesoporous TiO₂/RuO₂/CuO as photocatalyst under 450 W high-pressure mercury lamp irradiation. We have conducted water splitting studies by varying various parameters like the weight of the catalyst, concentration of CuO, amount of sacrificial agent, etc. We have also conducted water splitting recycling experiment with mesoporous TiO₂/RuO₂/CuO 1 %. The photocatalyst was irradiated continuously for 18 hrs and the hydrogen evolution rate was evaluated.

Photocatalytic H₂ Evolution Using TiO₂/RuO₂/CuO Ternary Nanosystem

We attained a maximum evolution of 20.7 mmol after 18 hours. The TEM and XPS results recorded before and after the water splitting reaction indicated that no change has occurred in the morphology and composition of the photocatalyst. The studies proved mesoporous TiO₂/RuO₂/CuO to be an efficient photocatalytic system for enhanced water splitting reaction

REFERENCES

1. Acar C, Dincer I and Natterer G.F, *Int. J. Energy Res.* 2016, 40, 1449–1473
2. Melo M.O, Silva L.A, *Journal of the Brazilian Chemical Society*, 2011, [Doi.org/10.1590/S0103-50532011000800002](https://doi.org/10.1590/S0103-50532011000800002)
3. Matsuoka M, *Catalysis Today*, 2007, 122, 51–6
4. Zhou H, Yu F, Zhu Q, Sun J, Qin F, Yu L, Bao J, Yu Y, Chen S, Ren Z, *Energy Environ. Sci.*, 2018, 11, 2858-2864
5. Safari F, Dincer I, *Energy Conversion and Management*, 2020, 205, 112182
6. Nozik A, *Nature* 1975, 257, 383–386
7. Leung D.Y.C, Fu X, Wang C, Ni M, Leung M.K.H, Wang X, Fu X, *Chem Sus Chem* , 2010, 3, 681–694
8. Jafari T, Moharreri E, Amin A. S, Miao R, Song W, Suib SL, *Molecules*, 2016, [Doi:10.3390/molecules21070900](https://doi.org/10.3390/molecules21070900)
9. Xiang Q, Yu J, Jaroniec M, *J. Phys. Chem. C* 2011, 115, 7355–7363
10. Meng Ni, Michael K.H. Leung, Dennis Y.C. Leung, K. Sumathy, M. Ni et al, *Renewable and Sustainable Energy Reviews*, 2007, 11, 401–425
11. Hou H, Shang M, Gao F, Wang L, Liu Q, Zheng J, Yang Z, Yang W, *ACS Appl. Mater. Interfaces*, 2016, 8, 20128–20137
12. Gillespie P.N.O, Martinsovich N, *ACS Appl. Mater. Interfaces* 2019, 11, 31909–31922
13. Nakata K, Fujishima A, *Journal of Photochemistry and Photobiology C: Photochemistry Reviews*, 2012, 13, 169-189
14. Kuvarega A.T, Krause R.W.M, Mamba B.B, *J. Phys. Chem. C* 2011, 115, 22110–22120
15. Wang S, Bai L, Ao X, *RSC Adv*, 2018, 8, 36745-36753
16. Dozzi M.V, Sellì E, *Journal of Photochemistry and Photobiology C*, 2013, 14, 13-28

17. Bian Z, Zhu J, Wang S, Cao Y, Qian X, Li H, J. Phys. Chem. C 2008, 112, 6258-6262
18. Petronella F, Truppi A, Dell Edera M, Agostiano A, Curri M.L and Comparelli R, Materials , 2019, 12, 1853
- 19., Jiang Z, Kong L, Alenazey F.S, Qian Y, France L, Xiao T, Edwards P.P, Nanoscale, 2013, 5, 5396-5402
20. Robert D, Catalysis Today, 2007, 122, 20-26
- 21 Diaz-Angulo J, Gomez-Bonilla I, Jimenez-Tohapanta C, Mueses M, Pinzona M, Machuca-Martinez F, Photochem. Photobiol. Sci., 2019, 18, 897-904
22. Suarez-Parra R, Hernandez-Perez I, Rincon M.E, Solar Energy Materials & Solar Cells , 2003, 76, 189-199
23. Mazumdar S, Bhattacharyya A, J, RSC Adv, 2015, 5, 34942-34948
24. Sabate J, Cervera-March S, Simarro R, Gimenez J, j. hydrogen energy, 1990, 15, 115-124
25. Cheng P, Yang Z, Wang H, Cheng W, Chen M, Shangguan W, Ding G, International Journal of Hydrogen Energy, 2012, 37, 2224-2230
26. Kubiak A, Swinska-Ciesielczyk K, Bielan Z, Adsorption, 2019, 25, 309–325
27. Aminia M, Ashrafia M, Nano. Chem. Res., 2016, 1, 79-86
28. Ahmed M.A, El-Katori E.E, Gharni Z.H, Journal of Alloys and Compounds, 2013, 553, 19-29
29. Nasirian M, Bustillo-Lecompte C.F, Mehrvar M, Journal of Environmental Management, 2017, 196, 487-498
30. Chan L, Yang S, Lixin C, Shaowei C, Journal of the Chinese Advanced Materials Society, 2013, 1, 188–19
31. Chen K, Ma L, Wang J.H, Cheng Z.Q, Yang D.J, Li Y.Y, Ding S.J, Zhou L, Wang Q.Q, RSC Adv, 2017, 7, 26097-26103
32. Kasem K.K, Finley A, Bull Mater Sci, 2015, 38, 303–308
33. Qian S, Wang C, Liu W, Zhu Y, Yao W, Lu, X, J. Mater. Chem, 2011, 21, 4945-4952

34. Tian H, Wan C, Xue X, Hu X, Wang X, *Catalysts* 2017, 7, 156.
35. Golzad-Nonakaran B, Habibi-Yangjeh A, *Materials Chemistry and Physics* 2016, 184, 210-221
36. Sabzehmeidani M.M, Karimi H, Ghaedi M, *New J. Chem*, 2020, 44, 5033-5048
37. Taufik A, Albert A, Saleh R, *Journal of Photochemistry and Photobiology A: Chemistry*, 2017, 344, 149-162
38. Colon G, Maicu M, Hidalgo M.C, Navio J.A, *Applied Catalysis B: Environmental*, 67, 2006, 41-51
39. Zhang P, Song T, Wang T, Zeng H, *RSC Adv.*, 2017, 7, 17873-17881
40. Ismail A.A, Robben L, Bahnemann D.W, *Chem Phys Chem*, 2011, 12, 982-991
41. Wang Z, Liu B, Xie Z, Li Y, Shen Z.Y, *Ceramics International*, 2016, 42, 13664-13669
42. Adel A. Ismail, Robben L, Bahnemann D.W, *Chem Phys Chem* 2011, 12, 982 – 991
43. Mousli F, Chaouchi A, Jouini M, Maurel, F, Kadri A, Chehimi, M.M, *Catalysts* 2019, 9, 578.
44. Kumaravel V, Imam M.D, Badreldin A, Krishna R.K, Do J.Y, Kang M, Abdel-Wahab A, *Catalysts* 2019, 9, 276
45. Ahmad H, Kamarudin S.K, Minggu L.J, Kassim M, *Renewable and Sustainable Energy Reviews*, 2015, 43, 599-610
46. Tian J, Hu X, Wei N, Zhou Y, Xu X, Cui H, Liu H, *Solar Energy Materials & Solar Cells*, 2016, 151, 7-13
47. Taufik A, Albert A, Saleh R, *Journal of Photochemistry and Photobiology A*, 2017, 344, 149-162
48. Hou H, Shang M, Gao F, Wang L, Liu Q, Zheng J, Yang Z, Yang W, *ACS Appl. Mater. Interfaces*, 2016, 8, 20128-20137

CHAPTER 6

PHOTOCATALYTIC DEGRADATION of CEFIXIME USING $\text{TiO}_2/\text{RuO}_2/\text{CuO}$ UNDER SUNLIGHT IRRADIATION

Contents

6.1 Introduction

6.2 Experimental Methods

6.3 Accumulated light energy calculation

6.4 Results and discussion

6.5 Photocatalytic studies

6.5.1 Photocatalytic degradation of cefixime antibiotic

6.5.1.2 Effect of different catalyst

6.5.1.3 Effect of catalyst loading

6.5.1.4 Effect of concentration of cefixime

6.5.1.5 Effect of concentration of CuO

6.5.1.6 Effect of H_2O_2 Addition

6.5.1.7 The degradation kinetics of cefixime

6.6 Mechanism of cefixime degradation

6.7 Conclusion

6.1 Introduction

One of the consequences of rapid industrialization is the excessive accumulation of hazardous pollutants in the environment. Water bodies are contaminated by a vast variety of pollutants. Pharmaceutical pollutants play a keen role in disrupting the life of aquatic organisms. Antibiotics are one of the major pharmaceutical compounds that cause a serious threat to humanity for the future generation. Antibiotics are natural, semisynthetic, or synthetic organic compounds that can either eradicate or hinder the growth of microorganisms, used to treat infectious diseases caused to plants animals, or humans, and also used as a food additive for the promotion of growth of animals and fishes^{1,2}. They get into the environment from various sources like pharmaceutical companies, hospital sewages, municipality effluents, etc. The excessive consumption and release of these antibiotics to the aquatic environment make them an emerging environmental issue that ultimately results in creating antibiotic-resistant microbes^{3, 4}. The large-scale accumulation of antibiotics in the aquatic environment results in the generation of bacterial strains that are resistant to the wide spectrum of antibiotics^{5, 6, 7}. Despite their low concentration in the aquatic life, it's too difficult to remove the non-biodegradable antibiotics from the environment by conventional wastewater treatment. So, an alternative for the harmless and economical abatement of the drugs released to the surroundings is one of the thought-provoking subjects in the area of research. Scientists have adopted numerous methods for the removal of antibiotics from aquatic bodies like sonochemical, adsorption, ion exchange, reverse osmosis,

etc^{8, 9}. The advanced oxidative process is a suggestive method for the mineralization of antibiotics. In this method, the catalyst on irradiation with light having energy greater than the band gap of the semiconducting photocatalyst results in the production of electrons and holes, which on reacting with water and dissolved oxygen produces hydroxyl radicals (OH[·]) and superoxide anions(O₂^{·-}). These hydroxyl radicals and superoxide anions produced will degrade the pollutants to CO₂ and H₂O^{10, 11}.

The advanced oxidative process is a preferred technique for the degradation of antibiotics as it achieves the complete oxidation of the pollutants. Based on the mode of generation of hydroxyl radicals, the advanced oxidative process can be classified into chemical¹², electrochemical¹³, sonochemical¹⁴, photochemical processes¹⁵, etc. whereas based on the phase of the catalyst and reaction mixture it can be classified into homogenous¹⁶ and heterogenous photocatalysis¹⁷. Among the various advanced oxidative techniques, photocatalysis is the most desirable method for the mineralization of antibiotics. As the name suggests photocatalysis is the acceleration of a reaction using a catalyst in the presence of light. Herein we have attempted the methodology of heterogeneous photocatalysis for the degradation of the antibiotic cefixime.

Penicillin was the first β -lactam antibiotic that was discovered in the twentieth century. The core part in the penicillin synthesis was the β -lactam nucleus, i.e. 6-aminopenicillanic acid. The modification of the β -lactam nucleus gave rise to more than 20 derivatives of antibiotics

like penicillin V, methicillin, carbenicillin, etc. The β -lactam antibiotics can be classified into cephalosporins, clavams, carbapenems, and monobactams. The cephalosporins are a group of β -lactam that showed a wide spectrum of activity against bacteria and are widely used¹⁸. Cephalosporins work by inhibiting the transpeptidases that are the structural component of bacterial cell wall¹⁹. Cephalosporins are classified into four generations based on their antimicrobial activity. Cefixime is a third-generation, oral cephalosporin antibiotic that belongs to the beta-lactam family of antibiotics^{20, 21}. The chemical formula of cefixime is (6*R*, 7*R*)-7-[[[(2*Z*)-2-(2-amino-1, 3-thiazol-4-yl)-2-(carboxymethoxyiminoacetyl] amino]-3-ethenyl-8-oxo-5-thia-1-azabicyclo [4.2.0] oct-2-ene-2-carboxylic acid. The structure is presented in Figure 6.1. Cefixime is effective against the broad spectrum of bacteria like *Neisseria gonorrhoeae*, *Haemophilus influenzae*, *Moraxella catarrhalis*, *Escherichia coli*, etc²². The antibiotic cefixime is used to treat the infections like pneumonia, bronchitis, syphilis, etc.

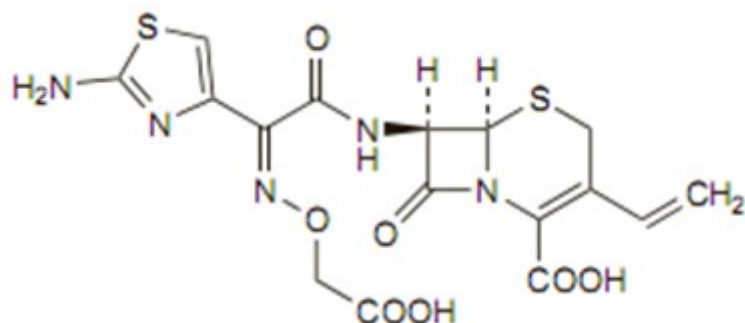


Figure 6.1: Structure of cefixime

Various studies have been conducted on the photocatalytic degradation of cefixime using semiconducting metal oxides. Yisalakshi et al achieved complete mineralization of cefixime using nanocrystalline ZnO in the presence of UV light²³. Mohsen Sheydaei et al successfully degraded 80% cefixime by photocatalytic ozonation process in visible light²⁴. Roqiyeh Mostafaloo et al synthesized BiFeO₃/Magnetic nanocomposites and underwent photocatalytic degradation of cefixime from aqueous solutions in the presence of visible light²⁵. Nawal Minab Shoostari et al used the hydrothermally prepared α -Fe₂O₃/ZnO for photocatalytic degradation of cefixime under UV and Visible lamp simultaneously²³. The present work explores the possibility of the ternary system TiO₂/RuO₂/CuO as a suitable photocatalyst for the degradation of the antibiotic cefixime.

TiO₂ is the most widely used catalyst that has been used for decades because of the facile synthesis, cost effectiveness, availability, stability etc^{26, 27}. But certain drawbacks like inability to utilize the visible light and large band gap restricts its application in photocatalytic degradation of the antibiotic cefixime²⁸. So, to improve the photocatalytic efficiency of TiO₂ various methods like the addition of sacrificial agents²⁹, dye sensitization³⁰, doping with transition metals³¹, noble metals³², and nonmetal element³³, coupling with metal³⁴, etc. are adopted²⁹⁻³⁶.

As discussed in chapter 4 several studies have been conducted on the binary system TiO₂/RuO₂ and TiO₂/CuO³⁷. Both of these binary systems serve to be efficient photocatalytic systems. For the further

improvement of the photocatalytic properties here we are dealing with the ternary mesoporous system $\text{TiO}_2/\text{RuO}_2/\text{CuO}$ that has not been reported so far. Scientists have reported studies in which the ternary system acts as an efficient photocatalytic system. Su et al. used the ternary system $\text{Ag-SrTa}_2\text{O}_6/\text{g-C}_3\text{N}_4$ for the photocatalytic degradation of the dye methyl orange in the presence of visible light⁴¹. Chenzuan Zhou et al reported the photocatalytic mineralization of the dye Rhodamine Blue using the ternary photocatalyst (CNNS/CdS/rGO) under visible light⁴². Zhanget al developed $\text{TiO}_2/\text{Ag}/\text{SnO}_2$ system by one step reduction process and evidenced the significant enhancement in the photocatalytic degradation of methylene blue in comparison with the bare TiO_2 or the binary composite (TiO_2/Ag or $\text{TiO}_2/\text{SnO}_2$).

It is expected that the combination of TiO_2 with RuO_2 and CuO is an ideal choice for the improvement of photocatalytic efficiency. Because it has already been reported in previous studies that the combination of TiO_2 with RuO_2 or CuO results in enhanced charge separation and reduced the band gap. The conduction and valence band edge position of TiO_2 , RuO_2 , and CuO are in an appropriate position that enables effective charge transfer and enhances the photocatalytic performance. In the present study, we report the application of the mesoporous ternary system $\text{TiO}_2/\text{RuO}_2/\text{CuO}$ synthesized by the sol-gel method for degradation of the antibiotic cefixime in the presence of sunlight. The present study reveals the ternary nanosystem $\text{TiO}_2/\text{RuO}_2/\text{CuO}$ to be an efficient system for photocatalytic wastewater purification using solar energy.

6.2 Experimental Methods

The chemicals used for the preparation of the photocatalysts TiO₂, TiO₂/RuO₂, TiO₂/RuO₂/CuO nanosystems, their suppliers, and the synthetic methods adapted are described in chapter 2.

6.3 Accumulated light energy calculation

We measured the intensity of sunlight at an interval of 5 minutes using a luxmeter (LX-103). The conversion of the intensity of sunlight to accumulated light energy is presented in the Table.1

Irradiation time(min)	In hours	Light intensity (LUX)	Integrated area of Intensity× time graph(A)	Wh/m ² A*0.0094444	Wh (*exposed area of the reaction mixture)	KWh
0	0	179000	62935	594.38	656.96	.66
5	0.083	179000				
10	0.167	195000				
15	0.250	195000				
20	0.333	195000				
25	0.417	190000	125980	1189.81	1315.07	1.32
30	0.500	190000				
35	0.583	180000				
40	0.667	195000				
45	0.750	195000	187455.5	1770.40	1956.79	1.96
50	0.833	180000				
55	0.917	180000				
60	1	146080				
65	1.083	186000	261986.32	2474.30	2734.79	2.73
70	1.167	170000				
75	1.250	179000				
80	1.333	193000				

Table.1 Accumulated light energy calculations for the study on photocatalytic degradation of cefixime

6.4 Results and discussion

We have employed $\text{TiO}_2/\text{RuO}_2/\text{CuO}$ nanosystems for the photocatalytic degradation of antibiotic cefixime under sunlight irradiation. The results obtained on catalyst characterization are mentioned in chapter 4.

6.5 Photocatalytic studies

All the experiments of photocatalytic degradation of the antibiotic cefixime were conducted in natural sunlight. The absorbance of the solution was measured using JASCO Spectrofluorometer (FP-8300) in the wavelength range of 200 to 800 nm.

6.5.1 Photocatalytic degradation of cefixime antibiotic

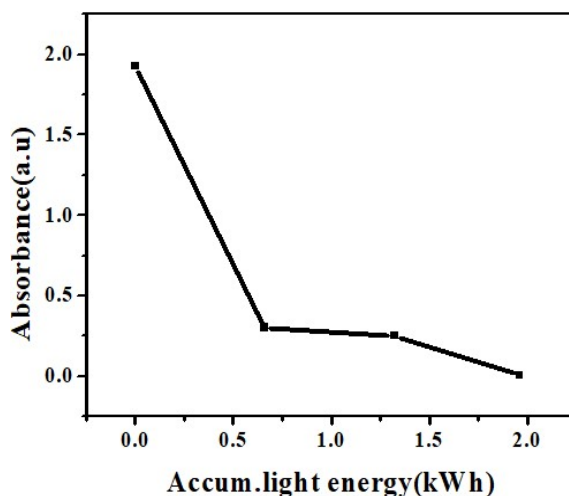


Figure 6.1 UV-Vis Spectra of the Reaction Mixtures after Catalyst removal, collected after sunlight irradiation of 0, 30, 45, 60 minutes of 100 mL reaction mixture with 250 mg/L cefixime and 0.0125 g mesoporous $\text{TiO}_2/\text{RuO}_2/\text{CuO}$ 0.05 % Catalyst

UV-Visible spectra of the photocatalytic degradation of cefixime were taken at an interval of 20 minutes of sunlight irradiation. The results obtained are illustrated in Figure 6.1. The effect of irradiation time was analyzed by performing a photocatalytic experiment with 0.0125 g mesoporous $\text{TiO}_2/\text{RuO}_2/\text{CuO}$ 0.05 % and 250 mg/L cefixime. It was found that on increasing the time there was an increase in photocatalytic efficiency. There was a profound increase in the rate of photocatalysis in the first twenty minutes. This might be due to the large-scale production of free radicals in the initial stage. After this degradation was found to occur at a slower rate. This was due to the consumption of free radicals by the intermediates that are produced during the mineralization process⁴⁶. The complete degradation of cefixime was achieved at a period of 60 minutes.

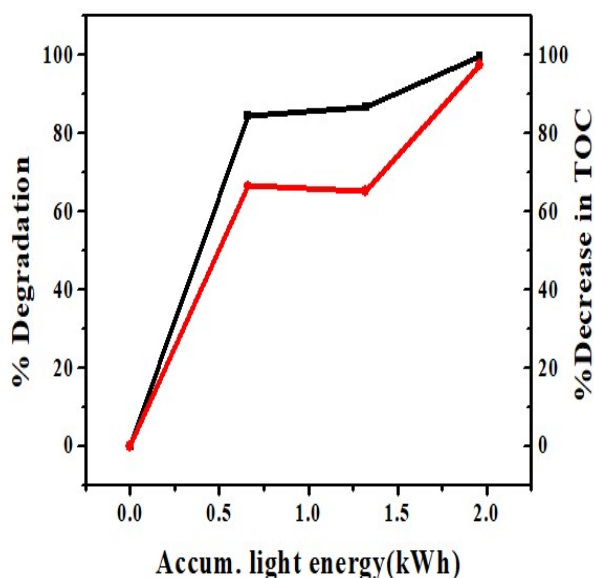


Figure 6.2 % Degradation obtained from the Absorbance measurement and % Decrease in TOC against Accumulated light energy

For the effective evaluation of the sunlight-assisted degradation of cefixime, we have conducted total organic carbon analysis and the results obtained are summarized in Figure 6.2. There was a difference in the percentage degradation obtained in TOC value and that of absorbance value of cefixime at the initial 20 and 40 minutes of sunlight irradiation. The difference in percentage degradation values obtained can be attributed to the formation of transient intermediates during the degradation process. After 60 minutes of irradiation process, the values obtained from TOC analysis was found to be in close proximity to that of absorbance obtained from the UV spectra indicating the complete degradation of cefixime

6.5.1.2 Effect of different catalyst

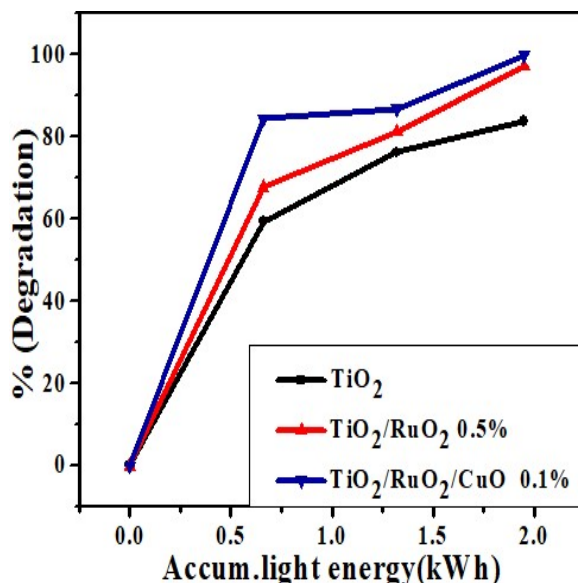


Figure 6.3: Performance of different photocatalysts towards the oxidative degradation of cefixime under sunlight irradiation for 60 minutes.

The plot of photocatalytic degradation of cefixime using the catalysts mesoporous TiO_2 , mesoporous $\text{TiO}_2/\text{RuO}_2$, and mesoporous $\text{TiO}_2/\text{RuO}_2/\text{CuO}$ is shown in Figure 6.3. The highest rate of photocatalytic activity was observed with the ternary system i.e., mesoporous $\text{TiO}_2/\text{RuO}_2/\text{CuO}$. The least activity was observed with the bare TiO_2 . The photocatalytic activity results suggest that surfactant has a prominent role in enhancing the photocatalytic activity. One of the factors that contributed to the highest activity in the case of mesoporous $\text{TiO}_2/\text{RuO}_2/\text{CuO}$ was the low band gap of the ternary system that requires only low source energy for the photoexcitation process. The interfacial transfer of electrons through the ternary system is another contributing factor for the enhanced degradation efficiency. The results reveal that the surface area, band gap modification, and charge separation have a significant role in the photocatalytic process. The BET, UV, and PL results support this argument.

6.5.1.3 Effect of catalyst loading

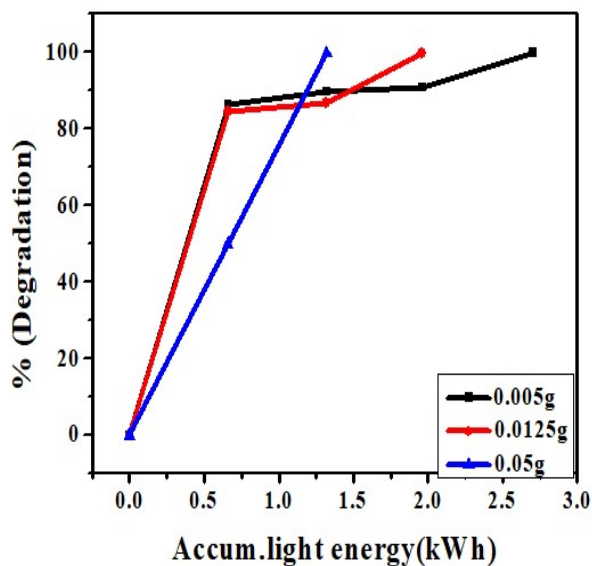


Figure 6.4 Optimization studies of catalyst weight carried out under irradiation with sunlight

The effect of the mass of catalyst on the photocatalytic degradation of cefixime was studied by varying the mass of $TiO_2/RuO_2/CuO$ 0.05% (Figure 6.4). All the parameters excluding the mass of the photocatalyst mesoporous $TiO_2/RuO_2/CuO$ 0.05% were kept constant. The results demonstrated that on increasing the mass of the catalyst from 0.005 to 0.05 g, the rate of degradation of cefixime increased. The relationship between rate and photocatalytic degradation of cefixime was found to vary linearly. This presence of more amount of catalysts resulted in the corresponding increase of the photoexcitation centers which in turn increased the number of hydroxyl radicals ($OH\cdot$)

and superoxide anions($O_2^{\cdot-}$) that are the key elements for the cefixime degradation^{43, 44}.

6.5.1.4 Effect of concentration of cefixime

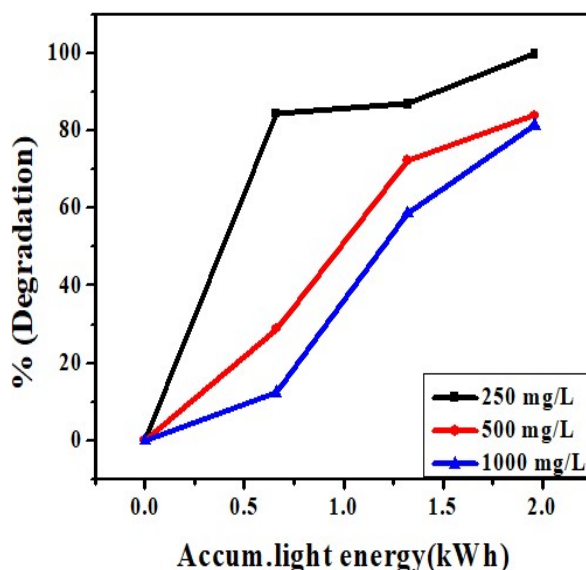


Figure 6.5 Effect of initial antibiotic concentration

The effect of concentration on the degradation of antibiotics was studied by keeping all the parameters fixed and varying the mass of cefixime (250 mg/L, 500 mg/L, and 1000 mg/L). From the figure, it is revealed that an increase in cefixime concentration leads to a decrease in the photocatalytic rate. The maximum photocatalytic efficiency was observed when the mass of cefixime was 250 mg/L further increase in a mass led to a decrease in photocatalytic efficiency. On increasing the mass of cefixime, a fraction of light might be absorbed by the cefixime instead of catalyst⁴⁵. And also the accumulation of cefixime at the

surface-active sites of the catalyst might inhibit the penetration of light to the catalyst surface. This will lead to a decrease in photoexcitation centers which leads to a reduction in the production of hydroxyl radicals and superoxide ions that are required for the degradation of cefixime.

. 6.5.1.5 Effect of concentration of CuO

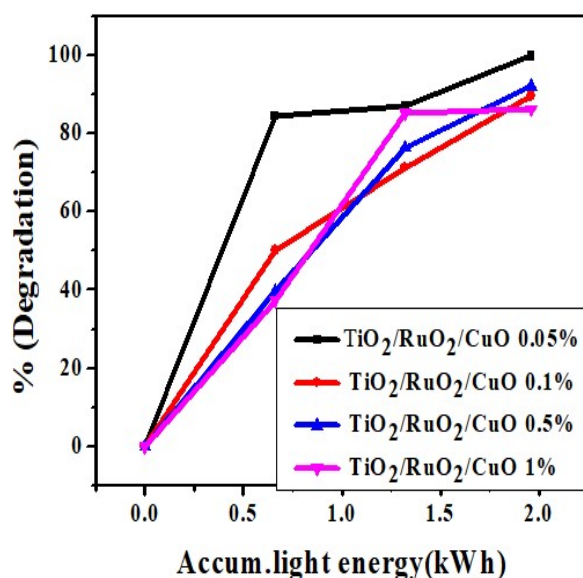


Figure 6.6 Effect of concentration of CuO

Figure 6.6 shows the effect of CuO content on the photocatalytic degradation of cefixime as a function of irradiation time. The photocatalytic performance of TiO₂/RuO₂/CuO was found to decrease with the increase in the concentration of CuO. The excess amount of CuO formed might cover the catalyst surface that is exposed to the sunlight⁴⁷. Thus, there was a reduction in the photocatalytic activity

when CuO was present beyond a certain limit. The excess CuO might have masked the surface-active site of the photocatalyst which ultimately resulted in the lowering of photocatalytic degradation of cefixime. The photocatalytic activity was found to decrease in the order TiO₂/RuO₂/CuO 0.05 % > TiO₂/RuO₂/CuO 0.1 % > TiO₂/RuO₂/CuO 0.5 % > TiO₂/RuO₂/CuO 1 %. Hence the optimum concentration of CuO for the maximum photocatalytic performance was 0.05 %.

.6.5.1.6 Effect of H₂O₂ Addition

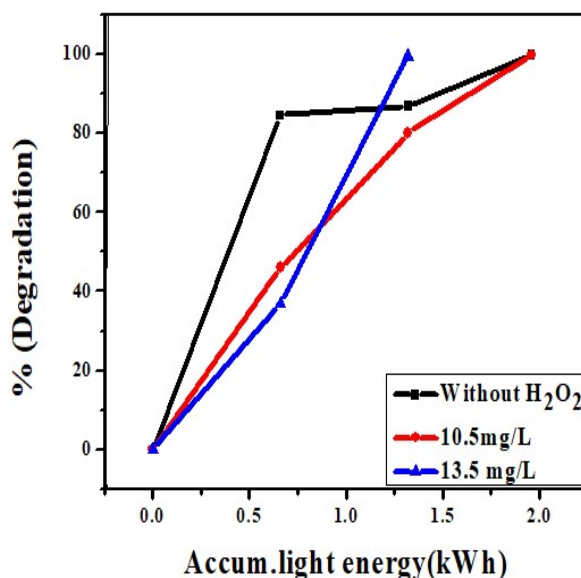
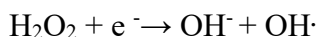


Figure 6.7 Effect of H₂O₂ addition

The effect of H₂O₂ on the photocatalytic degradation of cefixime with varying amounts of H₂O₂ was studied in the presence of the catalyst mesoporous TiO₂ /RuO₂/CuO 0.05 % keeping all the other parameters fixed (Figure 6.7). It is reported that H₂O₂ accelerates the

photocatalytic reaction by generating hydroxyl radicals in two ways i.e., by accepting a photogenerated electron from the semiconducting catalyst and reacting with superoxide anions^{48, 49}.



The efficiency of the photocatalytic reaction increased as the concentration of H₂O₂ increased. Comparing the results obtained using 0.0125 g of photocatalyst mesoporous TiO₂/RuO₂/CuO, the addition of 13.5 mg/L of H₂O₂ resulted in the complete mineralization of cefixime within 40 minutes.

6.5.1.7 The degradation kinetics of cefixime

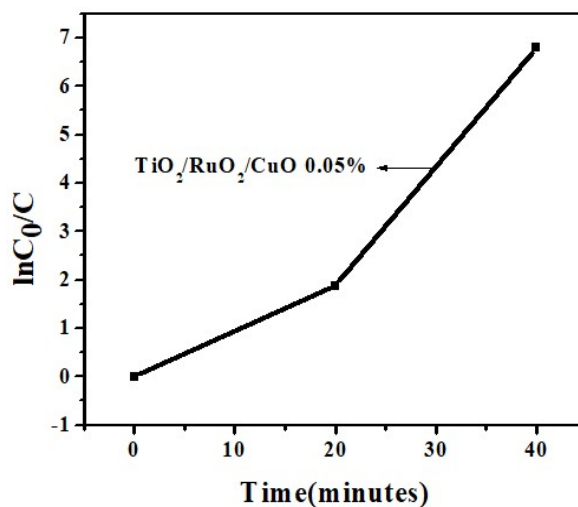


Figure 6.8 Plot of lnC₀/C versus time of cefixime degradation under sunlight irradiation

The degradation of cefixime was subjected to kinetic analysis (Figure 6.8). The apparent rate constant and correlation coefficient of the cefixime degradation is summarized in Table.2. The photocatalytic degradation of the antibiotic cefixime can be expressed in terms of the Langmuir-Hinshelwood model⁵⁰. After the attainment of equilibrium, the rate of the degradation reaction can be represented as,

$$\ln C_0/C = K_{app} \times t$$

where C_0 is the initial concentration of the antibiotic cefixime, C is the concentration of cefixime at time t , K_{app} is the apparent rate constant. A plot of $\ln C_0/C$ against time gives a straight line with slope k . The rate constant and correlation coefficient were calculated from the plot. We obtained an apparent rate constant of 0.17 from the slope. The value of correlation coefficient (R^2) obtained from regression analysis (0.88) suggests the kinetics of antibiotic degradation to be first order. From the above facts, it can be concluded that the degradation followed first-order kinetics.

Photocatalyst	Regression coefficient(R^2)	$K_{app}(\text{min})^{-1}$
TiO ₂ /RuO ₂ /CuO 0.05 %	0.88	0.17

Table. 2 Value of regression coefficient and apparent rate constant

6.6 Mechanism of cefixime degradation

The sunlight-assisted degradation of cefixime is believed to occur by the hydroxyl free radicals that are formed in the series of reactions³³.

Hence the hydroxyl radicals seem to be the most crucial factor determining the fate of the antibiotic degradation efficiency. In the case when TiO₂ was used alone low activity was observed due to the structural imperfections that lead to recombination of photogenerated electrons and holes. Previous studies report that coupling the semiconductor catalyst is one of the most advanced strategies to expand the visible light sensitivity, suppress the electron-hole recombination, enable the interfacial charge transfer, and consequently, increase the photocatalytic efficiency⁵¹. To reduce the band gap and the electron-hole recombination, in the present study we used the ternary mesoporous nanosystem TiO₂/RuO₂/CuO for the photocatalytic degradation of cefixime under sunlight.

The schematic illustration of the mechanism of photocatalytic degradation of cefixime is elucidated in Figure 6.9. On irradiation with sunlight having energy greater than threshold energy, the photoexcited electrons in the valence band get excited to the conduction band leaving behind holes in the valence band. The conduction band edge potential of TiO₂ is higher than that of RuO₂ and that of CuO is higher than RuO₂. The matching band structure promotes the transfer of photogenerated electrons in the conduction band of TiO₂ to RuO₂ and simultaneously from CuO to RuO₂ preventing the charge accumulation in the semiconductor. At the same time holes will migrate from the valence band of RuO₂ to the valence band of TiO₂ and CuO because of the more positive valence band edge of RuO₂ than that of TiO₂ and CuO. Thus, the photoinduced electrons and holes are effectively separated in the ternary system. The adsorbed oxygen reacts with

electrons accumulated in the conduction band producing superoxide anions meanwhile the holes react with the water molecules at the surface of the catalyst producing hydroxyl radicals. Finally, the holes, superoxide anions, and hydroxyl radicals that possess enough oxidation potential decompose the antibiotic cefixime to nontoxic products. The enhanced photocatalytic activity of the ternary system is attributed to the improved lifetime of the charge carriers due to the interfacial charge transfer.

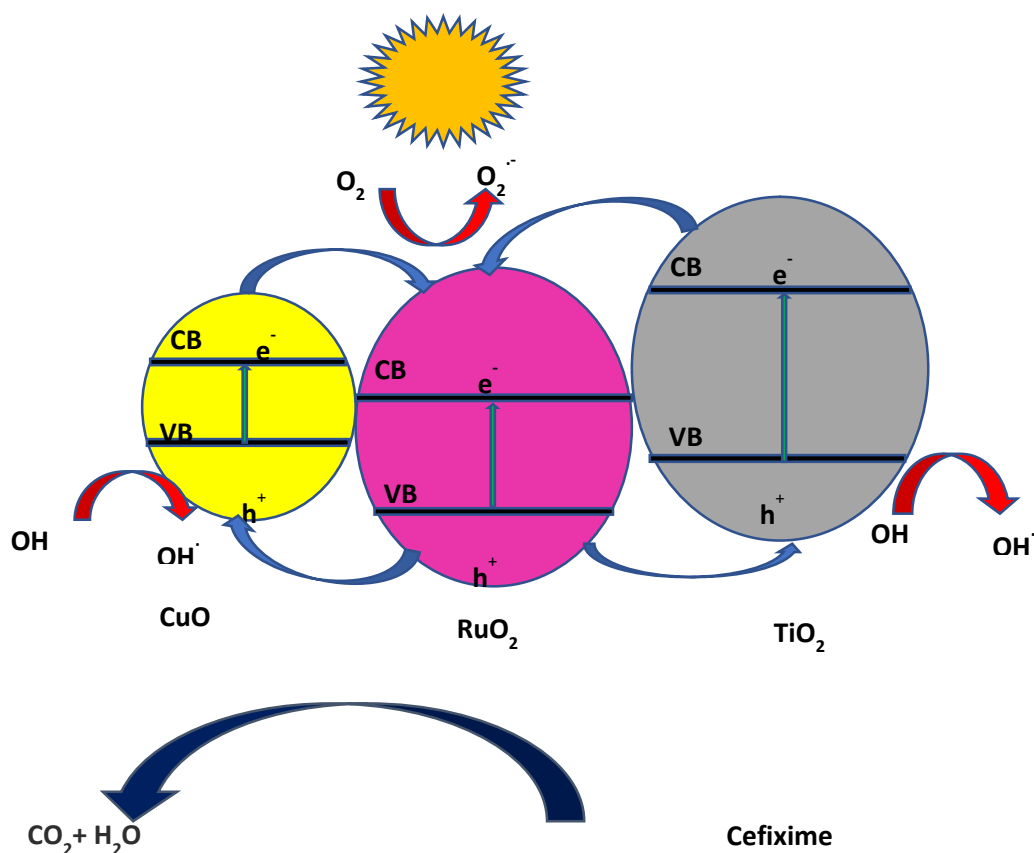


Figure 6.9: Mechanism of cefixime degradation

6.7 Conclusion

As reported in the previous chapter a simple surfactant-assisted sol-gel method is established for the successful synthesis of mesoporous TiO₂/RuO₂/CuO nanosystem. Herein we report the utilization of mesoporous TiO₂/RuO₂/CuO nanomaterial for the photocatalytic degradation of cefixime which acts as an effective tool for the protection of the environment from the accumulation of drugs and simultaneous production of antibiotic-resistant bacteria. A comparative study on the mineralization process was performed using mesoporous TiO₂, mesoporous TiO₂/RuO₂ and TiO₂/RuO₂/CuO were performed under sunlight irradiation and the ternary system proved to be the most efficient one. The optimization studies revealed that various factors like the concentration of antibiotics, irradiation time, mass of the catalyst, etc. have a pronounced influence on the mineralization of the antibiotic cefixime. From the kinetic studies, photocatalytic degradation of cefixime was found to obey first-order kinetics. The mesoporous TiO₂/RuO₂/CuO nanomaterial proved to be a better photocatalytic system for the effective degradation of the antibiotic cefixime under sunlight light.

REFERENCE

1. Du L, Liu W, Agron Sustain. Dev, 2012, 32, 309–327
2. Mehdi Y, Letourneau-Montminy M.P, Gaucher M.L, Chorfi Y, Suresh G, Rouissi T, Brar S.K, Cote C, Ramirez A.A, Godbout S, Animal Nutrition, 2018, 4, 170-178
3. Lofrano G, Libralato G, Adinolfi R, Siciliano A, Iannece P, Guida M, Giugni M, Ghirardini A.V, Carotenuto M, Ecotoxicology and Environmental Safety, 2016, 123, 65-71
4. Kumar M, Jaiswal S, Sodhi K.K, Shree P, Singh D.K, Agrawal P.K, Shukla P, Environment International, 2019, 124, 448-461
5. Shaniba C, Akbar M, Ramseena K, Raveendran P, Narayanan B.N, Ramakrishnan R.M, Journal of Environmental Chemical Engineering, 2020, 8, 102204
6. Derakhshan Z, Mokhtari M, Babaei F, J Environ Health Sustain Dev. 2016, 1, 43-62.
7. Li J, Xie S, Ahmed S, Wang F, Gu Y, Zhang C, Chai X, Wu Y, Cai J, Cheng G, Front Pharmacol. 2017, DOI: 10.3389/far.2017.00364
8. Homem V, Santos L, Journal of Environmental Management, 2011, 92, 2304-2347
9. Adams C, Asce M, Loftin W, Meyer M, J. Environ. Eng. 2002, 128, 253-260
10. Haddad MEI, Regti A, Laamari M.R, Mamouni R, Saffaj N, J. Mater. Environ. Sci, 2014, 5, 667-674
11. Deng Y, Zhao R, Current Pollution Reports, 2015, 1, 167–176
12. N. Azbara T, Yonar, K. Kestioglu, Chemosphere, 2004, 55, 35-43
13. Sires I, Brillas E, Oturan M.A, Rodrigo M.A, Panizza M, Environ Sci Pollut Res , 2014, 21, 8336–8367
14. Khataee A, Soltani R.D.C, Karimi A, Joo S.W, Ultrasonics Sonochemistry, 2015, 23, 219-230

15. Wols B.A, Hofman-Caris CHM, Water Research , 2012, 46, 2815-2827
16. Alaton I.A, Dyes and Pigments, 2004, 167-176
17. Ibhaddon A.O, Fitzpatrick P, Catalysts, 2013, 3, 189-218;
18. Hue T.T.T, Son D.C, Anh N.T.L, Anh N.T.K, Phong T.K, Hiramatsu K, J. Fac. Agr, Kyushu Univ, 2014, 59, 169–175
19. Georgopapadakou N.H, Bertasso A, Chan K.K, Chapman J.S, Cleeland R, Cummings L.M, Dix B.A, Keith D.D, Antimicrob Agents Chemother, 1989, 33, 1067-1071
20. Cefixime-induced nonconvulsive status epilepticus Anzellotti F, Ricciardi L, Monaco D, Ciccocioppo F, Borrelli I, Zhuzhuni H, Onofri M, Neurol Sci , 2012, 33, 325–329
21. Brogden R.N, Campoli-Richards D.M, Cefixime. Drugs , 1989, 38, 524–550
22. Elsabawy K.M, International Journal of Chemical Concepts, 2015, 01, 38-43
23. Shooshtari N.M, Ghazi M.M, Chemical Engineering Journal, 2017, 315, 527-536
24. Sheydaei M, Shiadeh H.R.K, Ayoubi-Feiz B, Ezzati R, Chemical Engineering Journal, 2018, 353, 138–146
25. Mostafaloo R, Mahmoudian M.H, Ghalhari M.A, Journal of Photochemistry & Photobiology A: Chemistry, 2019, 382, 111926
26. Li H, Zhang P, Yin S, Wang Y, Dong Q, Guo C, Sato T, J. Phys.: Conf. Ser, 2012, 339 , 012013
27. Vu A.T, Nguyen Q.T, Bui T.H.L, Tran M.C, Dang T.P, Tran T.K.H, Adv. Nat. Sci.: Nanosci. Nanotechnol., 2010 , 1, 015009
28. Khairy M, Zakaria W, Egyptian Journal of Petroleum, 2014, 23, 419-426
29. Vasileia M. Daskalaki, Antoniadou M, Li Puma G, Kondarides D.I, Lianos P, Environ. Sci. Technol. 2010, 44, 19, 7200–7205

30. Qin J, Huo J, Zhang P, Zeng J, Wang, Zeng H, *Nanoscale*, 2016, 8, 2249
31. Hameed A, Gondal M.A, Yamani Z.H, *Catalysis Communications*, 2004, 5, 715–719
32. Singh N, Prakash J, Gupta R.K, *Mol. Syst. Des. Eng*, 2017, 2, 422-439
33. Jiang L, Yuan X, Pan Y, Liang J, Zeng G, Wu Z, Wang H, *Applied Catalysis B: Environmental*, 2017, 217, 388–406
34. Yu G, Qian J, Zhang P, Zhang P, Zhang W, Yan W, Liu G, *Nat Commun*, 2019, 10, 4912
35. Gupta S.M, Tripathi M, *Chinese Sci Bull*, 2011, 56, 1639–1657
36. Shivaraju H.P, Midhun G, Anil Kumar K.M, Pallavil S, Pallavil N Shahmoradi B, *Appl Water Sci* , 2017, 7, 3937–3948
37. Mousli F, Chaouchi A, Jouini M, Maurel F, Kadri A, Chehimi M.A, *Catalysts*, 2019, 9, 578
38. Park. S, Shin. D, Yeo. T, Seo B, Hwang H, Lee J, Choi W, *Chemical Engineering Journal*, 2020, 384, 123269
39. Shi Q, Ping G, Wang X, Xu H, Li J, Cui J, Abroshan H, Ding H, Li G, *J. Mater. Chem. A*, 2019, 7, 2253-2260
40. Perazolli L, Nunez L, Silva M.R.A, Pegler G.F, Costalonga A.G.C, Gimenes R, Kondo M.M, Bertochi M.A.Z , 2011, 2, 564-571
41. Zhou C, Yan J, Chen B, Li P, Dong X, Xi F, Liu J, *RSC Ad.*, 2016, 6, 108955 –108963
42. Hameed B.H, Akpan U.G, Wee K.P, 2011, 27 204-209
43. Fabiyi M.E, Skelton R.L, *Journal of Photochemistry and Photobiology A, Chemistry*, 2000, 132, 121–128
44. Sahraeian S, Alipour V, Rahmanian O, *Hormozgan Medical Journal*, 2017, 21, 159-167
45. Farzadkia M, Rahmani K, Gholami M, Esrafil A, Rahmani A, Rahmani H, *Korean J. Chem. Eng.*, 31, 2014, 2014-2019

46. Zhou B, Zhao X, Liu H, Qu J, Huang C.P, Zhou B, Applied Catalysis B: Environmental, 2010, 99, 214–221
47. Elmolla E, S, Chaudhuri M, Desalination 2010, 252 , 46–52
48. Poullos I, Makri D, Prohaska X, Global Nest: the Int. J, 1999, 1, 55-62
49. Liao D.L, Badour C.A, Liao B.Q, Journal of Photochemistry and Photobiology A: Chemistry, 2008, 194, 11–19
50. Pan D, Ge S, Zhao J, Shao Q, Guo L, Zhang X, Lin J, Xu G, Guo Z, Dalton Trans, 2018, 47, 9765-9778
51. Sabzehmeidani M.M, Karimi H, Ghaedi M, New J. Chem., 2020, 44, 5033-5048

CHAPTER 7

SYNTHESIS OF $\text{TiO}_2/\text{ZnO}/\text{Fe}_2\text{O}_3$ NANOCOMPOSITE FOR PHOTOCATALYTIC DEGRADATION OF METHYLENE BLUE

Contents

7.1 Introduction

7.2 Experimental method

7.3 Photocatalytic methylene blue degradation studies

7.4 Results and Discussions

7.4.1 UV-Visible DRS analysis

7.4.2 XRD analysis

7.4.3 BET analysis

7.4.4 XPS studies

7.4.5 TEM studies

7.4.6 PL studies

7.4.7 Photocatalytic activity

7.4.8 Mechanism

7.1 Introduction

For the last few decades, we are under the threat of serious ecological imbalance that is being created by environmental pollution¹. Toxic materials have accumulated in the environment to such a large extent that there needs a destructive mineralization process that roots out the pollutants from the ecosystem. Among the various toxic materials that are being discharged into nature, the dyes released from the textile industry occupy the forefront position²⁻⁴. Methylene blue is a heterocyclic aromatic compound which when released to the aquatic environment harms the aquatic organisms by depleting the content of oxygen and releasing toxic substances⁴⁻⁵. There are various harmful effects of methylene blue. Scientists have reported various methods for the remediation of methylene blue from the ecosystem⁶⁻⁹. Heterogeneous photocatalysis is one of the most prominent methods for the degradation of hazardous materials in the environment¹⁰⁻¹³. In this method, the irradiation of photocatalyst results in the production of excitons. These excitons on reacting with water and oxygen produce hydroxyl radicals and superoxide anions that are capable of oxidizing pollutants. Various researches have been conducted by scientists to find an effective photocatalyst for performing degradation of these hazardous materials.

TiO₂ has great potential for various applications like water purification, drug degradation, solar cells, water splitting, etc. TiO₂ serves to be an efficient photocatalyst for the degradation of methylene blue¹⁴. Though there are many factors like cost-effectiveness, nontoxic nature,

resistance to corrosion, stability, etc. that attract TiO₂ as a good photocatalyst, the wide band gap, and visible light inactivity renders the scientist to modify the structural properties of TiO₂¹⁵⁻¹⁶. Scientists use various approaches like doping with metals and non-metals, photosensitization, coupling with organic and inorganic material, etc. to increase the performance of TiO₂ as a photocatalyst¹⁷⁻¹⁸.

ZnO is also found to be an active photocatalyst as the band gap of ZnO (3.37 eV) is comparable to that of TiO₂. ZnO is a prominent photocatalyst with unique properties like nontoxicity, stability, low price, electro-optical, catalytic properties etc¹⁹⁻²⁰. The attractive features of ZnO make it suitable for various applications like solar cells, diodes, antireflection coatings, sensors etc²¹⁻²³. One way to improve the property of TiO₂ is to couple it with a suitable semiconducting metal oxide. Scientists have conducted various studies on the binary system TiO₂/ZnO. The studies prove that coupling enhances the charge separation and modifies the electronic properties of the catalyst material.^{24, 25} Abinash et al synthesized hierarchical ZnO-TiO₂ nano heterojunction via the hydrothermal method that exhibited high photocatalytic performance towards the degradation of methylene blue²⁶. Very recently Zulfikar et al have studied in detail the degradation of humic acid (HA) from aqueous solutions under visible light irradiation using TiO₂/ZnO nanocomposite synthesized via the sol-gel method and observed high photocatalytic activity²⁷.

For the past years efforts have been taken by researchers to develop a ternary photocatalytic system. The photocatalytic activity of binary

systems can be improved by the introduction of a third system to the binary material. This further suppresses the electron-hole recombination and improves the photocatalytic efficiency of the system²⁸⁻³⁰. Nguyen et al synthesized TiO₂/ZnO/rGO (TZR) composites via the hydrothermal method and observed high photocatalytic performance towards the degradation of methylene blue, methyl orange, and rhodamine B³¹. Vinit et al observed high photocatalytic performance in the degradation of crystal violet dye when ternary reduced graphene oxide (rGO)-ZnO-TiO₂ nanocomposite prepared via sonochemical method was used as photocatalyst³². In the present study, we tried the effectiveness of the ternary photosystem TiO₂/ZnO/Fe₂O₃ system for the photocatalytic degradation of methylene blue. Studies have reported that the doping of TiO₂ with Fe increases the visible light sensitivity of TiO₂³³⁻³⁵. There are different preparative methods for the synthesis of metal oxides i.e., dip coating method, ball milling process, electrochemical method, sol-gel method, etc. The sol-gel method is a low-cost method for the synthesis of nanomaterials with high purity and homogeneity³⁶⁻³⁹.

As there is a lack of studies on photocatalytic degradation of methylene blue by TiO₂/ZnO/Fe₂O₃ we have focused our studies on this area. In our work, we have adopted the sol-gel method for the synthesis of TiO₂/ZnO/Fe₂O₃ ternary photocatalytic nanosystem. To elucidate the properties we report the structural, morphological, and optical properties of the compounds.

$TiO_2/ZnO/Fe_2O_3$ can be considered as a superior catalyst for photocatalytic degradation of methylene blue. Some reports on photocatalytic degradation are presented in Table .1.

Photocatalyst		Dye		Energy source	% Degradation		Reference
Name	Catalyst dosage(g)	Name	Concentration (mg/L)		Value	Time(minutes)	
Fe/FeS	0.5	Methylene blue	5	Visible light	96	200	40
Co alloyed CdZnS	0.03	Methylene blue	25	UV light	83	100	41
Degussa P25	0.2	Methylene blue	11.5	Visible light	40	120	42
CuO	0.1	Methylene blue	10	UV light	96.18	360	43
Degussa P25	0.2	Methylene blue	11.5	Laser, 150 mJ pulse energy	34	120	44
N-TiO ₂ /FACs	1.8	Methylene blue	20	Visible light	58	540	45
TiO₂/ZnO/Fe₂O₃	0.2	Methylene	31.98	Sunlight	100	170	Present work

Table. 1 Degradation characteristics of various materials

7.2 Experimental methods

The chemicals used for the preparation of TiO₂, TiO₂/ZnO, and TiO₂/ZnO/Fe₂O₃, nanomaterials, their suppliers, and the synthetic procedures are well explained in chapter 2.

7.3 Photocatalytic methylene blue degradation studies

Photocatalytic activities of synthesized samples were evaluated by the degradation of methylene blue dye (MB) in sunlight. The absorbance of the solution was measured using JASCO V-750 Spectrophotometer in the wavelength range 200 to 800 nm.

7.4 Accumulated light energy calculation

The intensity of sunlight was measured at an interval of 5 minutes using LUXMETER (LX-103). The conversion of the intensity of sunlight to accumulated light energy is presented in Table .2.

Table.2 Accumulated light energy calculations for the study on photocatalytic degradation of cefixime

Irradiation time(min)	In hours	Light intensity(LUX)	Integrated area of Intensity× time graph(A)	Wh/m ² A*0.0094444	Wh(*exposed area of the reaction mixture)	KWh
0	0	186000				
5	0.083	184000				
10	0.167	188500				
15	0.250	188500	62291	588.011	650.2375	.65
20	0.333	188500				
25	0.417	193000			1302.97	
30	0.500	172000	124821	1178.86		1.3
35	0.583	193000				
40	0.667	193000				
45	0.750	193000				
50	0.833	188000				
55	0.917	180000	187047.5	1766.551	1952.53	1.9
60	1	180000				
65	1.083	192000				
70	1.167	192000				
75	1.250	185000	249904.5	2360.198	2608.679	2.6
80	1.333	192000*				
85	1.417	185000				
90	1.500	185000	312408			
95	1.583	185000		2950.511	3261.14	3.3
100	1.667	182000				

7.5 Results and Discussions

TiO₂/ZnO/Fe₂O₃ nanocomposite was synthesized via the sol-gel method. The photocatalytic activity of prepared catalysts was evaluated by photocatalytic degradation of methylene blue under UV

and sunlight irradiation. The prepared nanocatalysts were characterized by UV-Visible DRS, XRD, BET, XPS, TEM, and PL analysis.

7.5.1 UV-Visible DRS analysis

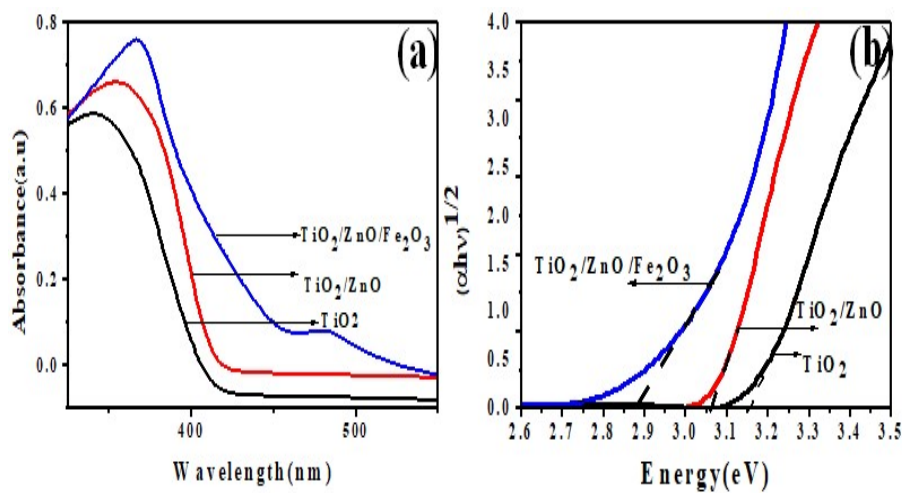


Figure 7.1 (a) UV-Vis DRS Spectra TiO₂, TiO₂/ZnO, TiO₂/ZnO/Fe₂O₃ nanocomposites (b) Kubelka-Munk plot of TiO₂, TiO₂/ZnO TiO₂/ZnO/Fe₂O₃ nanocomposites

The UV-Visible DRS of TiO₂, TiO₂/ZnO, and TiO₂/ZnO/Fe₂O₃ nanosystem was represented in Figure 7.1(a). The UV-Visible spectra of TiO₂/ZnO were slightly red-shifted in comparison to the spectra of bare TiO₂. This was further red-shifted in the ternary nanocomposite⁴⁶. The optical band gap energies were estimated from the Kubelka-Munk plot (Figure 7. 1(b)) and the corresponding values were 3.17 eV, 3.07 eV, and 2.9 eV for TiO₂, TiO₂/ZnO, and TiO₂/ZnO/Fe₂O₃ respectively. The reduction of band gap may be explained by relating the structural deformation of the compounds, as the novel composite structure was formed as depicted by XRD. However, the incorporation of iron

enhanced the visible light absorption power of the catalyst. The narrowing of the band gap of TiO₂/ZnO/Fe₂O₃ was expected to bolster the photocatalytic activity.

7.5.2 XRD analysis

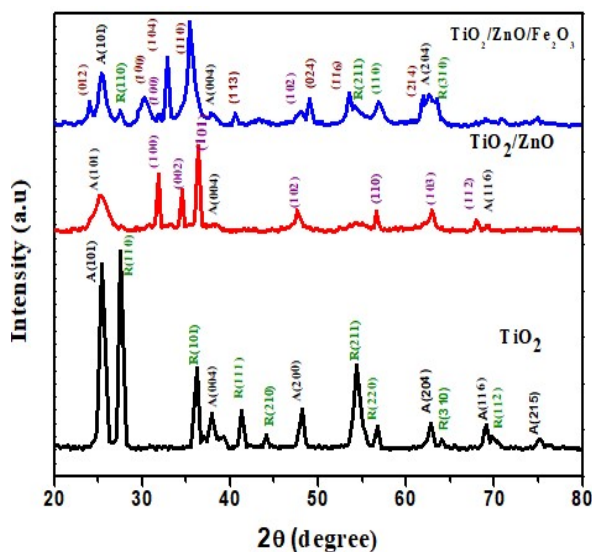


Figure 7.2 X-ray diffraction pattern of TiO₂, TiO₂/ZnO, TiO₂/ZnO/Fe₂O₃ nanocomposites

The nanocomposites formation was initially assessed by recording the XRD pattern indicated in Figure 7.2. The diffraction peaks 2θ at 25.39° , 37.85° , 48.11° , 62.76° , 69.05° , and 74.98° , respectively are the reflections of the (101), (004), (200), (204), (116), and (215) planes that originated from the anatase phase of TiO₂. While, 2θ at 27.5° , 36.14° , 41.3° , 44.16° , 54.37° , 56.69° , 64.12° and 69.87° corresponds to the (110), (101), (111), (210), (211), (220), (310) and (312) plane of rutile phase of TiO₂⁴⁷. The mixed-phase growth of TiO₂/ZnO was identified with the wurtzite hexagonal planes originated from points

31.8⁰, 34.5⁰, 36.2⁰, 47.6⁰, 6.8⁰, 62.9⁰, and 68.1⁰ along with the prominent TiO₂ phase⁴⁸. Apaced with TiO₂/ZnO planes, reflections at 23.99⁰, 30.3⁰, 32.87⁰, 35.42⁰, 40.53⁰, 49.05⁰, and 61.9⁰ originated due to the hematite phase of Fe₂O₃⁴⁹⁻⁵¹. These peaks confirmed the formation of TiO₂/ZnO/Fe₂O₃ nanocomposites and the broad intense peaks are substantiating evidence of the growth of nano-sized grains. This speculation is established with the grain size calculations performed by Scherrer equation and are displayed in Table.1. Employing Williamson and Smallman's formula we were able to calculate the dislocation density and presented in Table.2.

Compound	Average Grain Size (nm)	Dislocation Density $\times 10^{16} \text{m}^{-2}$	BET surface area (m ² /g)	Pore volume (cm ³ /g)	Regression coefficient (R ²)	K _{app} (min ⁻¹)
TiO ₂	22.53	0.20	29.1	0.029	0.99	0.007
TiO ₂ /ZnO	22.80	0.19	43.7	0.049	0.99	0.01
TiO ₂ /ZnO/Fe ₂ O ₃	24.26	0.17	78.5	0.1335	0.93	0.02

Table.3. Average grain size calculated from the Scherrer equation and dislocation density from Williamson-Smallman's formula as well as the BET results, regression coefficient and rate constant of TiO₂, TiO₂/ZnO and TiO₂/ZnO/Fe₂O₃

7.5.3 BET analysis

Surface characteristics of the catalyst were studied using Nitrogen adsorption analysis. The BET results of the catalysts are shown in Table.1. As the results presented, the BET surface area of TiO₂, TiO₂/ZnO, and TiO₂/ZnO/Fe₂O₃ were 29.1, 43.7, and 78.5 m²/g respectively. Specific surface areas have a pronounced effect on

photocatalytic activity. The BET results revealed the presence of Zn²⁺ and Fe³⁺ ion significantly increased the surface area of the samples. This is expected to activate more sites on the surface of the catalyst and thus improved the photocatalytic activity⁵²

7.5.4 XPS studies

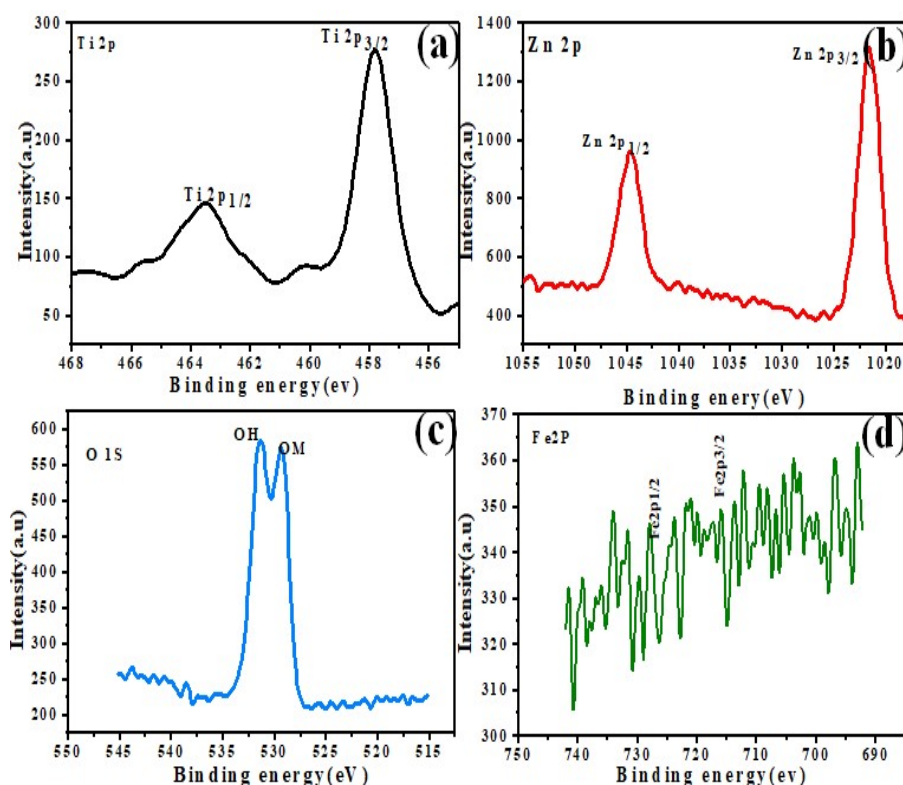


Figure 7.3 High-resolution XPS data of TiO₂/ZnO/Fe₂O₃ (a) Ti 2p region, (b) Zn 2p region, (c) O 1s region, (d) Fe 2p region respectively.

We investigated the elemental composition of the prepared samples by X-ray photoelectron spectroscopy (XPS). Figure 7.3 shows the XPS spectra of TiO₂, TiO₂/ZnO, and TiO₂/ZnO/Fe₂O₃. The XPS spectrum of

Ti binding energy regions was shown in Figure 7.3(a). The peaks around 457.8. and 463.55 eV can be attributed to Ti 2p_{3/2} and Ti 2p_{1/2} respectively⁵³⁻⁵⁵. The difference in the binding energy of 5.8 eV explains the valency of Ti as Ti⁴⁺. The peaks at binding energy values 1021.7 and 1044.6 eV indicated in Figure 7.3(b) were attributed to Zn 2p_{3/2} and 2p_{1/2} in which Zn is present in 2⁺ oxidation state⁵⁶. The XPS spectrum of Oxygen in Figure 7.3(c) shows two main peaks at 529.5 and 531.5 eV. The binding energy 529.5 and 531.5eV shown in Figure 7.3(d) is attributed to the lattice oxygen and surface adsorbed oxygen respectively⁵⁷. The weak peak of Fe 2p confirms the low content of Fe₂O₃ in the composite. The results of XPS analysis confirm the successful synthesis of TiO₂/ZnO/Fe₂O₃ nanocomposite. The atomic percentages of elements obtained from the area of curves are presented in Table.3.

Name	Position(eV)	FWHM (eV)	At%
Ti2p	456	4.1	22.8
Fe2p	716	3.1	0.4
O1s	529	4.7	42.8
Zn2p	1020	4.7	36.0

Table .4 XPS parameter obtained from the survey scan of TiO₂/ZnO/Fe₂O₃ nanocomposite and the atomic percentages obtained from it

7.5.5 TEM studies

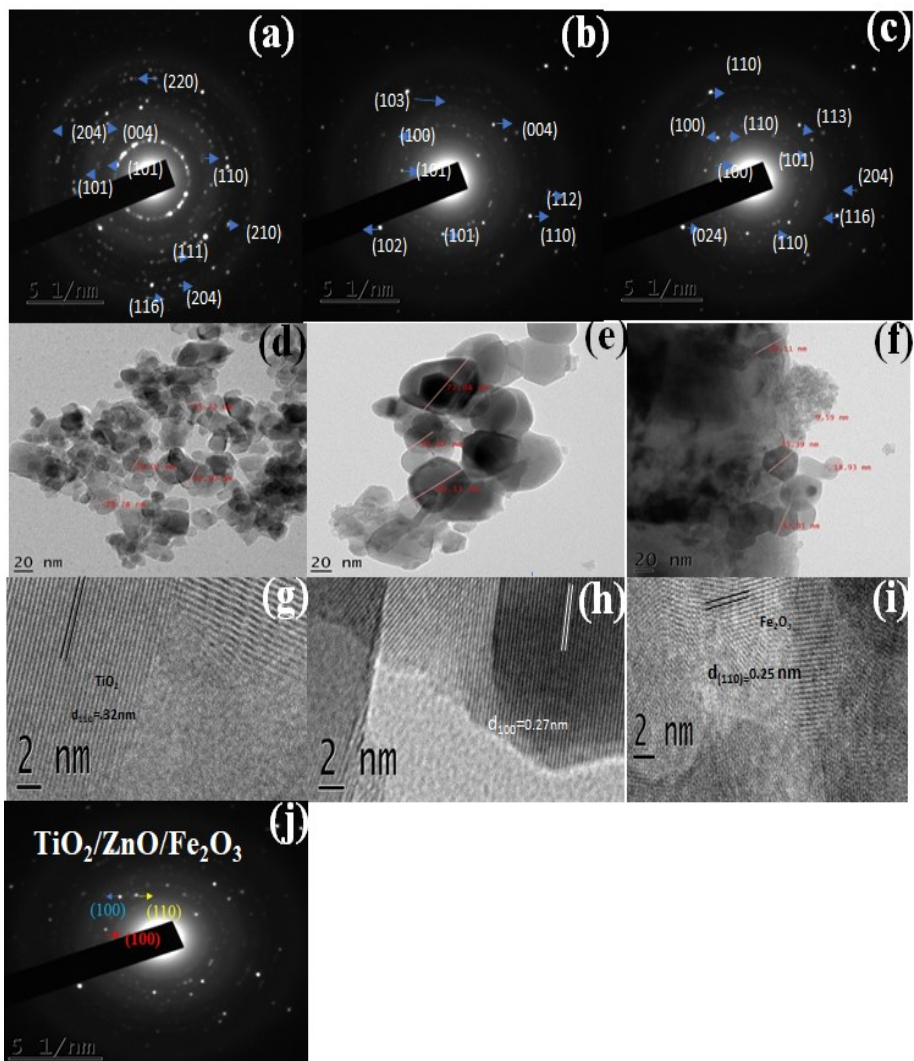


Figure 7.4 (a), (b) and (c) SAED patterns of TiO_2 , TiO_2/ZnO and $\text{TiO}_2/\text{ZnO}/\text{Fe}_2\text{O}_3$ (d), (e) and (f) TEM images of TiO_2 , TiO_2/ZnO and $\text{TiO}_2/\text{ZnO}/\text{Fe}_2\text{O}_3$ (g), (h) and (i) HRTEM images of TiO_2 , TiO_2/ZnO and $\text{TiO}_2/\text{ZnO}/\text{Fe}_2\text{O}_3$ (j) SAED patterns of TiO_2 , TiO_2/ZnO and $\text{TiO}_2/\text{ZnO}/\text{Fe}_2\text{O}_3$

The surface topography of TiO₂, TiO₂/ZnO, and TiO₂/ZnO/Fe₂O₃ are displayed in Figure 7.4, comprising TEM, HRTEM images, and SAED ring patterns. The images divulge aggregated growth of particles in semi-globular shapes. In binary and ternary composites, the shapes of particles were unaltered with roughly spherical. However, the average particle size obtained for TiO₂, TiO₂/ZnO, and TiO₂/ZnO/Fe₂O₃ was 19.1, 54.4, and 26 nm respectively. From the high-resolution TEM image the gap between two fringes in TiO₂, TiO₂/ZnO and TiO₂/ZnO/Fe₂O₃ were 0.32, 0.27, and 0.25 nm, which can be indexed to (110), (100) and (111) planes corresponding to TiO₂, ZnO and Fe₂O₃ respectively (Figure 7.4(g), (h) and (i)). The measurements obtained from the SAED rings for the three samples were consistent with the results of the XRD pattern. From the TEM image, it is evident that an interfacial contact exists in the ternary nanocomposite.

7.5.6 PL studies

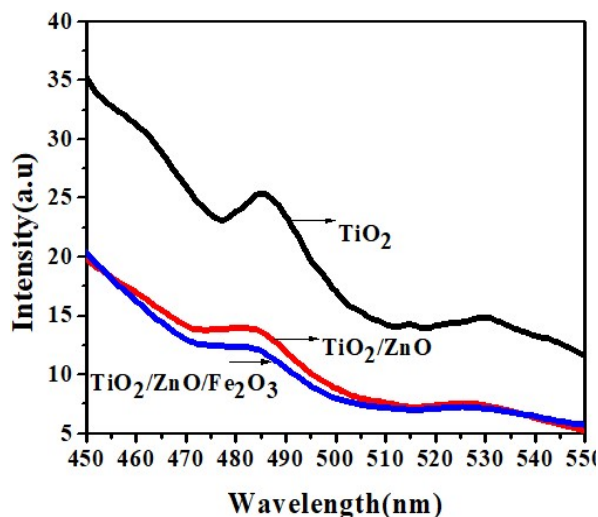


Figure 7.5 Relative photoluminescence emission of TiO₂, TiO₂/ZnO, and TiO₂/ZnO/Fe₂O₃ nanocomposite

In Figure 7.5, the PL spectrum of TiO₂, TiO₂/ZnO, and TiO₂/ZnO/Fe₂O₃ are displayed. PL emission intensity is directly related to the electron-hole recombination, the higher the PL intensity photocatalytic rate will be lower. The materials exhibited two broad PL emission signals at 485 and 525 nm, the signal at 485 was due to the surface oxygen vacancies and emission at 525 was due to the localized F⁺ centers on the surfaces of compounds⁵⁸⁻⁵⁹. The surface oxygen vacancies will act as a charge trapping center and prevent electron-hole recombination. The emission intensity of the PL spectra was obtained in the following order TiO₂ > TiO₂/ZnO > TiO₂/ZnO/Fe₂O₃. The decrease of PL intensity indicated the lower recombination rate of photogenerated electron-hole pairs. The presence of ZnO and Fe₂O₃ in the crystal symmetry of TiO₂ has obviously resulted in the lowering of PL intensity. The results propound the photocatalytic activity can be higher in TiO₂/ZnO/Fe₂O₃ as it can suppress the combination between the photogenerated electrons and holes.

7.6 Photocatalytic activity

Ultraviolet and sunlight irradiation on a 10⁻⁴ M methylene blue solution was used to test the photocatalytic dye degradation activity. The complete degradation of methylene blue under UV irradiation using TiO₂/ZnO/Fe₂O₃ catalyst occurred within a period of 130 minutes (Figure 7.6(a)). However, on sunlight irradiation using the same catalyst the complete mineralization was achieved within 170 minutes, and its corresponding absorption spectra are indicated in Figure 7.6(b). Evaluation of the photocatalytic dye degradation experiment was

performed using the equation $\ln C_0/C = kt$. The photocatalysis followed the first-order kinetics. The values of rate constant and regression constant is presented in Table.4. The degradation percentage was calculated using the following equation.

$$\text{Degradation percentage} = ((A_0 - A_t)/A_0) \times 100\%$$

Where A_0 and A_t represents the absorbance of methylene blue at the time 0 and t respectively. The order of photocatalytic activity of the catalyst was as follows, $\text{TiO}_2 < \text{TiO}_2/\text{ZnO} < \text{TiO}_2/\text{ZnO}/\text{Fe}_2\text{O}_3$. This affirms the formation of ternary composites has resulted in a significant enhancement in photocatalytic activities. The improved photocatalytic activity of $\text{TiO}_2/\text{ZnO}/\text{Fe}_2\text{O}_3$ nanocomposite can be mainly attributed to the reduction in the band gap of the ternary nanocomposite. Alongside, as observed from the surface studies, the higher surface area of the ternary composite is a contributing factor to the high photocatalytic efficiency. PL intensity of $\text{TiO}_2/\text{ZnO}/\text{Fe}_2\text{O}_3$ was lowered in comparison to the other two samples indicating the slow rate of electron-hole recombination taking place in the samples in this category⁶⁰. All these facts account for the highest photocatalytic activity of $\text{TiO}_2/\text{ZnO}/\text{Fe}_2\text{O}_3$ nanocomposites.

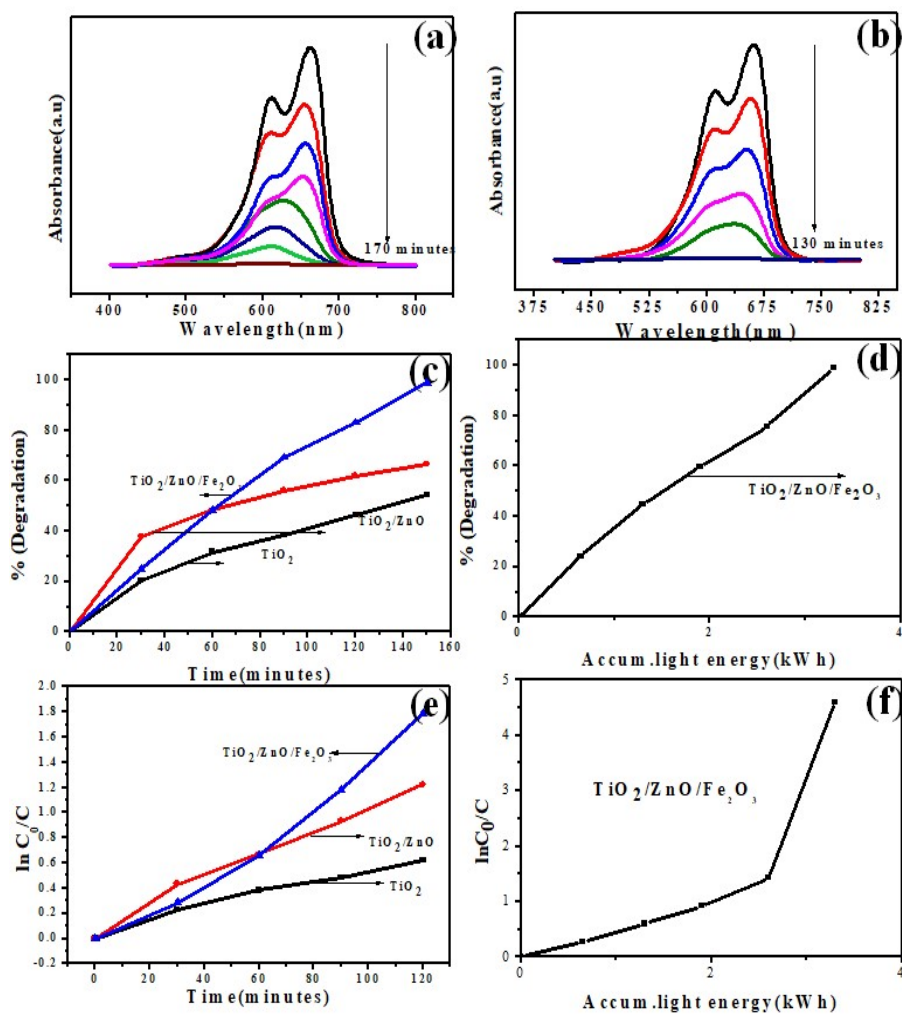


Figure 7.6 UV absorption Spectra of photocatalytic degradation of methylene blue in the presence of (a) UV light irradiation (b) sunlight irradiation (c) percentage of degradation of methylene blue under UV irradiation and (d) percentage of degradation of methylene blue under sunlight irradiation (e) $\ln C_0/C$ versus time of methylene blue degradation under UV irradiation (f) $\ln C_0/C$ versus time of methylene blue degradation under sunlight irradiation

Photocatalyst	Regression coefficient(R^2)	Kapp(min) ⁻¹
TiO ₂	0.99	0.007
TiO ₂ / ZnO	0.99	0.01
TiO ₂ / ZnO/Fe ₂ O ₃	0.93	0.02

Table.5 Value of regression coefficient and rate constant

7.7 Mechanism

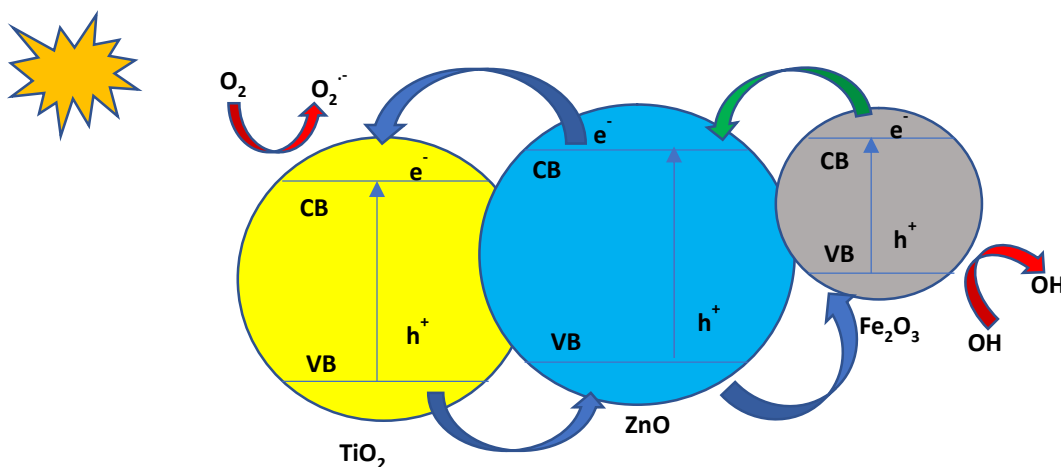


Figure 7.7 Mechanism of methylene blue degradation

The matching band structure of TiO₂, ZnO, and Fe₂O₃ is a favorable condition for the effective charge transfer⁶¹. The coupling of semiconductors helped in improving the visible light sensitivity and suppressing the electron-hole recombination and promoting the interfacial charge transfer⁶². To describe the mechanism of

photocatalytic dye degradation a prior knowledge on the band edge position of the conduction band and valence band of TiO₂, ZnO and Fe₂O₃ should be acquired. Before the formation of the ternary system, both the conduction band edge and valence band edge level of Fe₂O₃ were placed in between that of ZnO⁶³. As Fe₂O₃ comes in contact with ZnO, there occurs a shift in the energy bands of ZnO and Fe₂O₃ till the Fermi level attain equilibrium⁶⁴⁻⁶⁶. So, on irradiation, the electrons continue to transfer from the conduction band of Fe₂O₃ to that of ZnO and TiO₂. The conduction band edge and valence band edge of ZnO are slightly higher than that of TiO₂⁶⁷⁻⁶⁸. At the same time, the holes from the valence band of TiO₂ are transferred to the valence band of Fe₂O₃ and ZnO enhancing the effective spatial charge separation. Both the electrons and holes play a vital role in methylene blue degradation. The holes react with water molecules adsorbed on the surface to produce hydroxyl radicals whereas the photogenerated electrons on reacting with the adsorbed oxygen produce superoxide anions. The hydroxyl radicals and superoxide anions have the ability to decompose the dyes. Thus, the ternary system act as an efficient photocatalytic system by inhibiting the electron-hole recombination.

7.8 Conclusion

The study can be summarized as follows, binary and ternary metal oxide nanocomposites have been successfully synthesized incorporating TiO₂, ZnO, and Fe₂O₃ metal oxides through a facile sol-gel method. The synthesized samples were subjected to various studies in order to depict their photocatalytic performance in methylene blue

degradation. X-ray diffraction study confirmed the mixed growth of metal oxide powders in the multiphase composite category. The measurements obtained from SAED patterns were consistent with planes calculated from XRD. Brunauer–Emmett–Teller analysis revealed a predominant increase of surface area in TiO₂/ZnO/Fe₂O₃ composite in comparison to that of TiO₂ and TiO₂/ZnO. It was inferred from the study that TiO₂/ZnO/Fe₂O₃ nanocomposite possesses visible light sensitivity, enhanced charge separation, and high surface area than the other two compound systems. The aforesaid factors shaped TiO₂/ZnO/Fe₂O₃ nanocomposite, a far superior candidate than the bare TiO₂ and TiO₂/ZnO in the photocatalytic performance of methylene blue degradation. The complete mineralization of the dye in the presence of UV light was achieved within a period of 130 minutes is one of the major findings of the study alongside the degradation of the same concentration of the dye in direct sunlight within 170 minutes.

REFERENCE

1. Pathak C, Mandalia H.C, Journal of Environmental Pollution, 2011, 2, 08-10
2. Ehrampoush M.H, Moussavi G.H.R, Ghaneian M.T, Rahimi S, Ahmadian M, 2010, 9, 4279-4285
3. Dargo H, Gabbiye N, Ayalew A, International Journal of Innovation and Scientific Research, 2014, 9, 317-325
4. Sangpour P, Hashemi F, Moshfegh A.Z, J. Phys. Chem. C , 2010, 114, 13955–13961
5. Alkaykh S, Mbarek A, Ali-Shattle E.E, Heliyon, 2020, 6, 2020
6. Abbasi M, Asl N.R, J. Hazard. Mater. , 2008, 153, 942–947
7. Zaghbani N, Hafiane A, Dhahbi M, Desalination , 2008, 222 , 348–356
8. Sarria V, Deront M, Peringer P, Pulgarin C, Appl. Catal. B , 2003, 40, 231–246.
9. Rafatullah M, Sulaiman O, Hashim R, Ahmad. A, Rafatullah M, 2010, 177 , 70–80
10. Ibhaddon A.O, Fitzpatrick P, Catalysts , 2013, 3, 189-218
11. Beldjoudi Y, Atilgan A, Weber J.A, Roy I, Young R.M, Yu J, Deria P, Enciso A.E, Wasielewski M.R, Hupp, Stoddart J.F, Advanced Materials, 2020, 32, 2001592
12. Gisbertz S, Pieber B, ChemPhotoChem, 2020, 4, 456-475
13. Ibhaddon A.O, Fitzpatrick P, Catalysts 2013, 3, 189-218
14. Haque M.M, Muneer M, Dyes and Pigments, 2007, 75, 443-448
15. Jaihindh D.P, Chen C.C, Fu Y.P, RSC Adv, 2018, 8, 6488
16. Wei M, Peng X.L, Liu Q.S, Li F, Yao M.M, Molecules , 2017, 22, 950

17. Sridharan K, Jang E, Park T.J, Applied Catalysis B: Environmental , 2013, 142, 718-728
18. Khan S.B, Faisal, Rahman M.M, Jamal A, Science of The Total Environment , 2011, 409, 2987-2992
19. Sin J.C, Lam S.M, Lee K.T, Mohamed A.R, Materials Letters 2013, 91, 1-4
20. Diaz-Angulzo J, Porras J, Mueses M, Torres-Palma R.A, Hernandez-Ramirez A, Machuca-Martinez F, Journal of Photochemistry and Photobiology A: Chemistry, 2019, 383, 112015
21. Li M, Bala H, Lv X, Ma X, Sun F, Tang L, Wang Z, Materials Letters , 2007, 61, 690 -693
22. Cimitan S, Albonetti S, Forni L, Peri F, Lazzari D, Journal of Colloid and Interface Science , 2009, 329, 73-80
23. Huang J, Yin Z , Zheng Q, Energy & Environmental Science , 2011, 10, 3861-3877
24. Janitabar-Darzi S, Mahjoub A.R, Journal of Alloys and Compounds , 2009, 486, 805-808
25. Marc G, Augugliaro V, Lopez-Munoz M.J, Martı C, Palmisano L, Rives V, Schiavello M, Tilley R.J.D, Venezia A.M, J. Phys. Chem. B , 2001, 105, 1033-1040
26. Das A, Kumar P.M, Bhagavathiachari M, Nair R.G, Applied Surface Science, 534, 2020, 147321
27. Zulfikar M.A, Chandra A.D, Rusnadi N.M, Setiyanto H, Handayani N, Wahyuningrum D, Songklanakarin J. Sci. Technol, 2020, 42, 439-446
28. Keller V, Garin Catalysis Communications, 2003, 4, 377-383
29. De La Garza-Galvan M, Zambrano-Robledo P, Vazquez-Arenas J, Romero-Ibarra I, Ostos C, Peral J, García-Pérez U.M, Applied Surface Science, 2019, 487, 743-754
30. .Liu C, Xu Li, Wu Y, Sun L, Zhang L, Chang X, Zhang X, Wang X, Ceramics International, 2019, 45, 17163-17172

31. Nguyen C.H, Tran M.L, Van Tran T.T, Juang R.S, Separation and purification technology, 2020, 232, 115962,
32. PoteV.D, ShirsathS.R, Bhanvase B.A, Saharan V.K, Optik, 2020, 208, 164555
33. Chen, XQ, Yang, JY, Zhang, JS, J Cent. South Univ. Technol. , 2004, 11, 161–165
34. .Volfova L, Plizingrova E, Ecorchard P, Motlochova M, Klementova M, Janosikova P, Bezdicka P, Kupcik J, Krysa J, Lancok A, Subrt J, J. Phys. Chem. C (2020) 12, 6669–6682
35. .Mei Q, Zhang F, Wang N, Yang Y, RSC Adv, 2019, 9, 22764-22771
36. .Estrada-Flores S, Martinez-Luevanos A, Perez-Berumen C.M, Garcia-Cerda L.A, Flores-Guia T.E, BoletIn De La Sociedad Espanola De Ceramica Y Vidrio, 2020, 59, 209-218
37. .Pino-Sandoval D, Villanueva-Rodriguez M, Cantu-Cardenas M.E, Hernandez-Ramirez A, Journal of Environmental Chemical Engineering, 2020, 8, 2213-3437
38. .Wiranwetchayan O, Promnopat S, Thongtem T, Chaipanich A, Thongtem S, Materials Chemistry and Physics, 2020, 240, 122219
39. . Reda K. S.M, Khairy M, Mousa M.A, Arabian Journal of Chemistry, 2020, 13, 86-95
40. Esmaili H, Kotobi A, Sheibani S, Rashchi F, Int. J. Min. Met. Mater, 2018, 25, 244–252
41. .Horoz S, Baytar O, Sahin O, Kilicvuran H, J. Mater. Sci. Mater. Electron. , 2018, 29, 1004–1010.
42. Yamani Z.H, Arab. J. Sci.Eng. , 2018, 43, 423–432
43. Aly H.M, Moustafa M.E, Nassar M.Y, Abdelrahman E.A, J. Mol. Struct. , 2015, 1086, 223-231
44. Yamani Z.H, Arab. J. Sci.Eng., 2018, 43, 423–432
45. Li C, Wang B, Cui H, Zhai J, Li Q, Journal of Materials Science & Technology, 2013, 29, 835-840

46. Xia Y, Yin L, Phys. Chem. Chem. Phys, 2013, 15, 18627-18634
47. He J, Du Y, Bai Y, An J, Cai X, Chen Y, Wang P, Yang X, Feng Q, Molecules , 2019, 24, 2996
48. Lin L, Yang Y, Men L, Wang X, He D, Chai Y, Zhao B, Ghoshroy S, Tang Q, Nanoscale, 2013, 5, 588-593
49. Sharma B, Boruah P.K, Yadav A, Das M.R, Journal of Environmental Chemical Engineering , 2018, 6, 134-145
50. Bouhjar F, Mari B, Bessais B, J Anal Pharm Res , 2018, 7, 315–321
51. Xin Li, Yu H, Xiangxin Xu, Procedia Environmental Sciences , 2016 , 31, 582 – 588
52. Mazinani B, Masrom A.K, Beitollahi A, Luque R, Ceramics International, 2014, 40, 11525-11532
53. Tiantian C, Peng H, Kaichen Z, Ziqi S, Kai Z, Ligang Y, Kang C, Nin. C, Yongfang L, J. Mater. Chem. A , 2018, 6 , 435–3443
54. Yuan M, Zhengjie W, Haiwang W, Guanqi W, Yukai Z, Pengcheng H, Yuanming L, Dekua G, Hongqin P, Bingzhu W, Xiwei Q, Cryst Eng Comm, 2019, 21 , 3982-3992
55. Wang L, Qi T, Wang J, Zhang S, Xiao H, Ma Y, Journal of Hazardous Materials, 2018, 342, 579-588
56. Hui A, Ma J, Liu, Bao Y, Zhang J, Hui A, Journal of Alloys and Compounds , 2017, 696, 639-647
57. Kovalevsky.AV, Populoh S, Patricio SG, Thiel P, Ferro MC, Fagg DP, Frade JR, Weidenkaff.A, J. Phys. Chem. C , 2015, 9, 4466–4478
58. Wen L, Liu B, Zhao X, Nakata K, Murakami T, Fujishima A, International Journal of Photoenergy, 2012, doi.org/10.1155/2012/368750
59. Jaihindh D.P, Chen C.C, Fu Y.P, RSC Adv., 2018, 8, 6488-6501
60. Yu J.C, Ho W, Lin J, Yip H, Wong P.K, Environ. Sci. Technol., 2003, 7 , 2296

61. Shwetharani R, Sakar M, Fernando C.A.N, Binas V, Geetha R, Catal. Sci. Technol. , 2019, 9, 12 –46
62. Munawar K, Mansoor M.A, Basirun W.J, Misran M, Huang N.M, Mazhar M, RSC Adv., 2017, 7, 15885 –15893
63. Gao J, Luan X, Wang J, Wang B, Li K, Li Y, Kang P, Han G, J. Desalination , 2011, 268, 68 –75
64. Angkita Mistry Tama, Subrata Das, Dutta S, Bhuyan M.D.I, Islam M.N, Basith M.A, RSC Adv , 2019, 9, 40357–40367
65. Kaneti Y.V, Zakaria Q.M.D, Zhang Z, Chen C, Yu J, Liu M, Jiang X, Yu A, J. Mater. Chem A , 2014, 2, 13283-13292
66. Tama A.M, Das S, Dutta S, Bhuyan M.D.I, Islam M.N, Basith M. A, RSC Adv, 2019, 9, 40357-40367
67. Liu X, Pan L, Lv T, Sun Z, Journal of Colloid and Interface Science , 2013, 394 , 441–444
68. Janitabar -Darzi S, Mahjoub A.R, Journal of Alloys and Compounds , 2009, 486, 805–808

CHAPTER 8

COMPARATIVE STUDY ON PHOTOCATALYTIC DEGRADATION OF METHYLENE BLUE USING STRONTIUM TITANATE SYNTHESIZED IN THE PRESENCE AND ABSENCE OF PLURONIC P123

Contents

- 8.1 Introduction*
 - 8.2 Experimental methods*
 - 8.3 Photocatalytic degradation studies*
 - 8.4 Results and discussions*
 - 8.4.1 UV-Visible DRS analysis*
 - 8.4.2 FT-IR analysis*
 - 8.4.3 XRD analysis*
 - 8.4.4 BET analysis*
 - 8.4.5 XPS studies*
 - 8.4.6 SEM and TEM studies*
 - 8.4.7 PL studies*
 - 8.5 Photocatalytic activity*
 - 8.6 Mechanism*
 - 8.7 Conclusion*
-

8.1 Introduction

One of the major achievements of this 21st century is the rapid growth of industrialization. The recent advancement in the industrial sector has become a major source for the rupture of ecological balance. Currently, we are looking forward for an effective method to alleviate the environmental issue. Complete mineralization of hazardous pollutants using photocatalysis is a proficient method to scale down the environmental impacts of industrialization¹. Strontium titanate (SrTiO₃) forms a versatile material with interesting properties like high stability, high corrosion resistance, large nonlinear optical coefficient, which finds its application in optical, electronic, electrooptical, and electromagnetic devices²⁻⁵. Strontium is a large band gap semiconductor that can absorb light more effectively than that of germanates, tantalates, and niobates⁶. The photocatalytic performance of a catalyst is dependent upon the effectiveness of charge separation and absorption of light.

Strontium titanate can be considered as an effective photocatalyst for various purposes like degradation of pollutants, dyes, antibiotics, water splitting, and CO₂ reduction⁷. The superior characteristics of strontium titanate like stability in chemical and structural aspects, resistance to heat, and corrosion have triggered the application of this material in the field of photocatalysis⁸.

Liang et al synthesized strontium titanate via sol-gel route for the photocatalytic degradation of nitrogen oxides (NO_x) and observed that calcination temperature and light condition have a pronounced

influence in the photocatalytic activity⁹. Henrique et al developed a conventional method for the synthesis of strontium titanate microsphere to undergo pH-dependent degradation of methylene blue and Rhodamine B¹⁰. Macaraig et al conducted a comparative study on photocatalytic H₂ generation using strontium titanate nanoparticles and nanofibers and reported that strontium titanate mesoporous nanofibers showed the highest photocatalytic activity¹¹. The ability of porous strontium titanate spheres to degrade Rhodamine B via photocatalysis was reported by Wenjun et al and the prepared sample exhibited complete degradation of the dye within 20 minutes under UV illumination. Lea et al conducted a comparative study on photocatalytic H₂ generation by strontium titanate nanoparticles and nanofibres¹². Their study indicated that the strontium titanate nanofibers synthesized at 700 °C showed the highest photocatalytic activity that can be attributed to the mesoporous structure, low band gap, and high crystallinity of the nanofibers.

Colour is the most attractive part of the material. Dyes are colouring substances that impart color and have a high affinity to the substance in which it is being applied. They are used in various sectors of life such as textiles, medicines, food, cosmetics, and utensils. With the advent of the industrial revolution and the growth of the textile industry there arose an era of synthetic dyes. It was William J. Perkin who discovered synthetic dye in 1856. Even a minute amount of dye can impart serious toxic effects to life¹³. Organic dyes constitute one of the major sources of wastewater pollutant¹⁴. By evaluating the volume and effluent composition textile industry seems to be the leading

source of pollutants rather than other industrial sectors¹⁵. Being aromatic and non-biodegradable, the removal of dye is a tedious task¹⁶.

Methylene blue, Congo red, methyl orange, rhodamine is the most widely used textile dyes. Among this methylene blue (methyl thionine chloride) is the most common one which is used in various fields like medical, chemical, pharmaceutical, and solar cells. Methylene blue is a cationic thiazine dye that was discovered by Caro in 1876. It is a heterocyclic compound with the chemical formula $C_{16}H_{18}ClN_3S$. The absorption maximum of methylene blue was observed at 663 nm. The accumulation of methylene blue results in serious disorders like headache, mental confusion, abdominal pain, fever, and sore throat. In this regard, attempts have been done by various scientists for the degradation of this dye¹⁷⁻¹⁸.

There are numerous methods employed for the synthesis of mesoporous strontium titanate nanomaterials¹⁹⁻²¹. A facile solvothermal method for the synthesis of the mesoporous film of strontium titanate for photosensitized solar devices was reported by Burnside et al¹⁹. Zheng et al synthesized mesoporous Nd-doped strontium titanate nanospheres and nanoplates with high specific surface areas and excellent photocatalytic activity via microwave-assisted solvothermal method²⁰. Kayaalp et al reported the synthesis of mesoporous strontium titanate for methylene blue degradation by using the cooperative assembly of metal chelate complexes and alkoxysilanes²¹. However, the sol-gel combustion method is one of the cost-effective methods for the synthesis of pure, homogenous, and

crystalline oxide powder²²⁻²³. Bhagwat et al synthesized cobalt ferrite nanoparticles via the sol-gel combustion method in the presence of various fuels such as ethylene glycol, glycine, and urea and studied the influence of these fuels on the structural, morphological, and magnetic properties of cobalt ferrite²⁴. From the results obtained, it was inferred that the particle size of the synthesized material was influenced by the fuel employed during sol-gel combustion.

Studies reveal that the mesoporous structures can enhance the photocatalytic activity of catalysts. Tarawipa et al employed mesoporous strontium titanate nanocrystals via the surfactant-assisted sol-gel method for the degradation of methyl orange²⁵. From the observations, it was evident that surface area, crystallinity, and pore characteristics have a pronounced effect on photocatalytic activity. Wei et al reported the application of mesoporous strontium titanate spheres for the photocatalytic degradation of rhodamine B²⁶. The catalyst showed high photocatalytic activity that was found to be dependent on reaction time and PVA concentration. Jian et al employed Nd-doped mesoporous strontium titanate nanospheres and nanoplates for the photocatalytic generation of H₂ under visible light²⁷.

Notably to our best of knowledge, synthesis of mesoporous strontium titanate using pluronic polymer or other carbonaceous source is rarely reported. Existing literature lacks 1) sol-gel combustion strategy for the preparation of mesoporous strontium titanate using carbonaceous sources (2) influence of mesoporosity of strontium titanate on the

photocatalytic degradation of methylene blue in comparison with non-mesoporous strontium titanate materials.

In our present work, we demonstrated the preparation of strontium titanate (STO) and mesoporous strontium titanate (MSTO) by the sol-gel combustion method in the presence and absence of nonionic triblock co-polymer pluronic P123 as a structure-directing agent. The materials were well characterized by various experimental techniques. The photophysical properties of the material were studied by the photodegradation of methylene blue under UV light irradiation. Influences of pore size, crystallinity, surface area, band gap, morphology, luminescent properties, and elemental composition on the surface of the materials were well studied. The photodegradation ability of the MSTO and STO was studied by using methylene blue as a model pollutant.

8.2 Experimental methods

The chemicals used for the preparation of STO and MSTO, their suppliers, and synthetic procedures are mentioned in chapter 2.

8.3 Photocatalytic degradation studies

To study the photocatalytic efficiencies of the MSTO and STO materials, photocatalytic degradation studies were conducted using methylene blue on a photoreactor of model LZC-4X-Luzchem photoreactor with UV light intensity 600 lux. The experimental procedures are explained in detail in chapter 2.

8.4 Results and discussions

We have synthesized SrTiO₃ nanocatalysts and performed various characterization techniques. The photocatalytic activity of the catalyst was evaluated by the degradation of methylene blue under UV irradiation.

8.4.1 UV-Visible DRS analysis

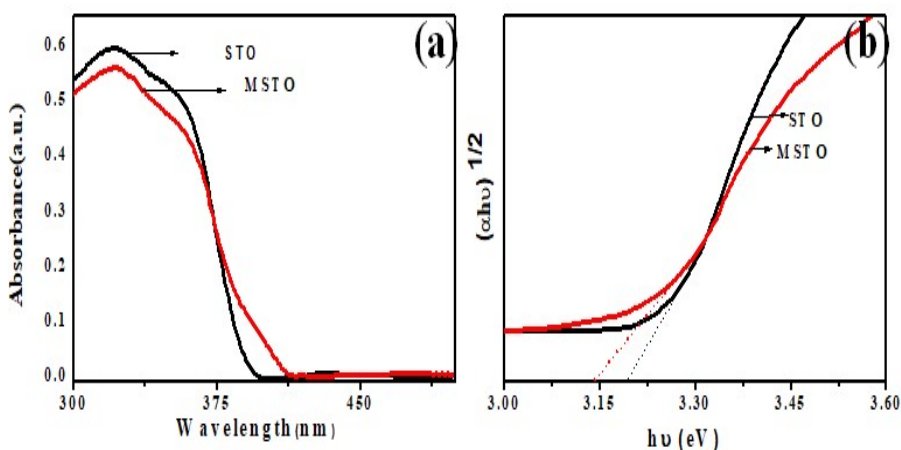


Figure 8.1 (a) UV-Vis DRS Spectra of STO and MSTO materials (b) Kubelka-Munk plot of STO and MSTO materials respectively.

The UV-Visible diffuse reflectance absorption spectrum was shown in Figure 8.1(a). The spectra of STO showed a cut-off wavelength at 319 nm whereas MSTO showed an absorption edge at 414 nm. The absorption spectra of MSTO showed a slight red shift in comparison with the spectra of STO due to the mesoporous nature of the material. The band gap energy was estimated from the Kubelka-Munk plot (Figure 8.1 (b)) and the band gap energy decreased from 3.21 eV to 3.14 eV for MSTO compared to that of STO. Therefore, the MSTO

thus extended the absorption edges to the visible regions. The reduction in the band gap could be attributed to the attenuated light scattering by the mesoporous structure²⁸.

8.4.2 FT-IR analysis

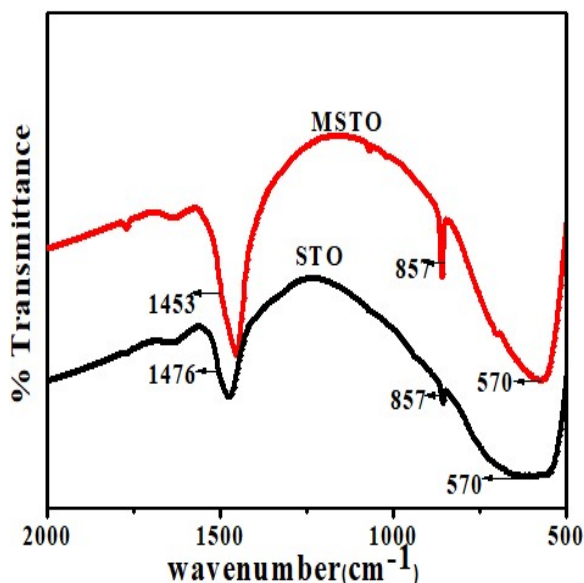


Figure 8.2 FT-IR spectra of the samples STO and MSTO

FT-IR spectra obtained for STO and MSTO were shown in Figure 8.2. The bands at 857 and 570 cm^{-1} were ascribed to the stretching vibration of Sr-O and Ti-O bond²⁹. The peak at 570 cm^{-1} was broadened for STO. The peak at 1453 arises from CO_3^{2-} vibration³⁰. The intensity of this peak was high in MSTO indicating the presence of more carbonate species on this material. The vibrational band 1453 cm^{-1} was slightly blue-shifted compared to STO. The blue shift of the

peak in MSTO might have aroused due to the adsorption of carbonate species on the surface of MSTO³¹.

8.4.3 XRD analysis

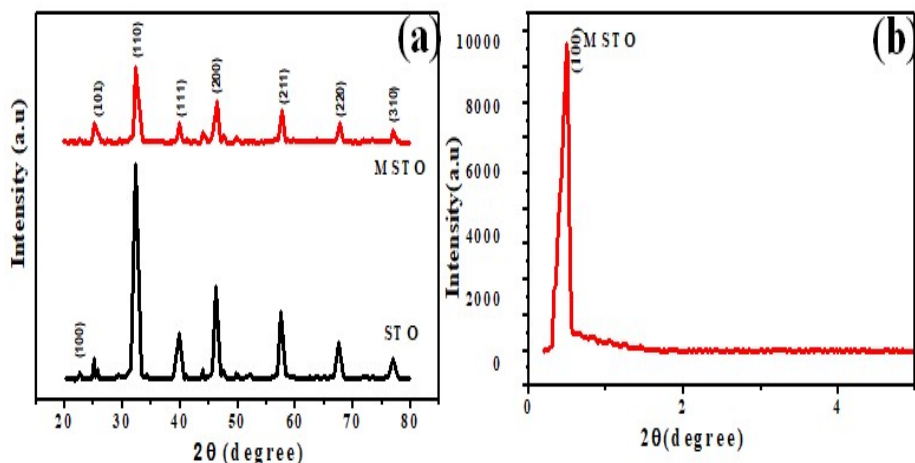


Figure 8.3 (a) high angle powder XRD patterns and (b) low angle powder XRD patterns of STO and MSTO materials

High angle and low angle XRD patterns of STO and MSTO samples were presented in Figure 8.3 (a) and (b) respectively. The peaks at 2θ angles 22.60° , 32.30° , 39.90° , 46.40° , 52.20° , 57.60° , 67.60° , and 76.90° can be indexed to (100), (110), (111), (200), (210), (211), (220) and (310) planes of strontium titanate with cubic perovskite structure³²⁻³⁴. The peak at 25.10° can be indexed to (101) plane of SrCO_3 formed during heat treatment process³⁵. The average crystalline size of the material was determined using the Debye-Scherrer equation and shown in Table 1. Williamson and Smallman's formula was used to calculate the dislocation density. The average crystalline size calculated for STO and MSTO was found to be 27.6 nm and 25.4 nm respectively. The

dislocation densities of STO and MSTO were 0.13 and 0.15 respectively. The low angle XRD patterns (Figure 8.3(b)) indicated strong diffraction peak corresponding to (100) plane, characteristics of two-dimensional mesoporous structure with spatial group P6mm, typical of structures organized in a hexagonal array³⁶

Compound	Average Grain Size^a (nm)	Dislocation Density $\delta \times 10^{16} \text{m}^{-2}$^b	Specific surface area m^2/g^c	Pore diameter (nm)^d
STO	27.6	0.13	17	-
MSTO	25.4	0.15	13	21

Table.1 Average grain size, dislocation density and the BET results of STO and MSTO samples

^aAverage grain size calculated from the Scherrer equation

^bdislocation density from Williamson-Smallman's formula

^ccalculated from BET adsorption isotherms

^dcalculated from Barrett–Joyner–Halenda (BJH) equation using the desorption isotherm

8.4.4 BET analysis

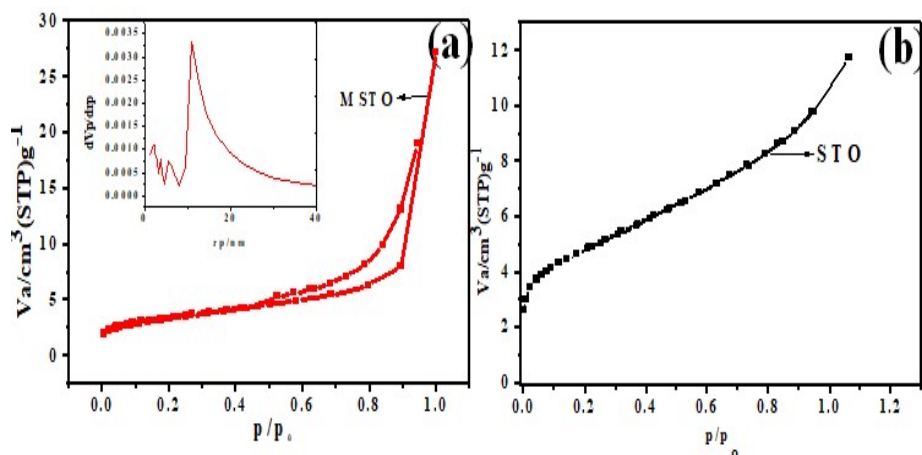


Figure 8.4 N_2 -sorption isotherms of (a) MSTO and (b) STO. The corresponding pore size distribution plot for MSTO is also shown in the inset.

The effect of pluronic P123 on the surface area of the MSTO and STO was studied by N_2 adsorption-desorption isotherms. The isotherms are shown in Figure 8.4(a) and Figure 8.4(b) respectively. The isotherm of MSTO shown in Figure 8.4(a) indicated the presence of type IV pattern with H3 type hysteresis loop. This might be due to the existence of well-developed mesopores with slit-like pores with non-uniform sizes and shape^{37, 38}. The isotherms of MSTO indicated a typical type IV curve with monolayer adsorption at low values of relative pressures (P/P_0), followed by multilayer adsorption and capillary condensation at a relative pressure of $0.46-0.94P/P_0$. The material STO showed in Figure 8.4(b) indicated the presence of type II adsorption-desorption isotherm, which is typically characteristic of nonporous materials. The specific surface area calculated from the BET adsorption isotherms of MSTO and STO were 12 and 17 m^2/g respectively.

8.4.5 XPS studies

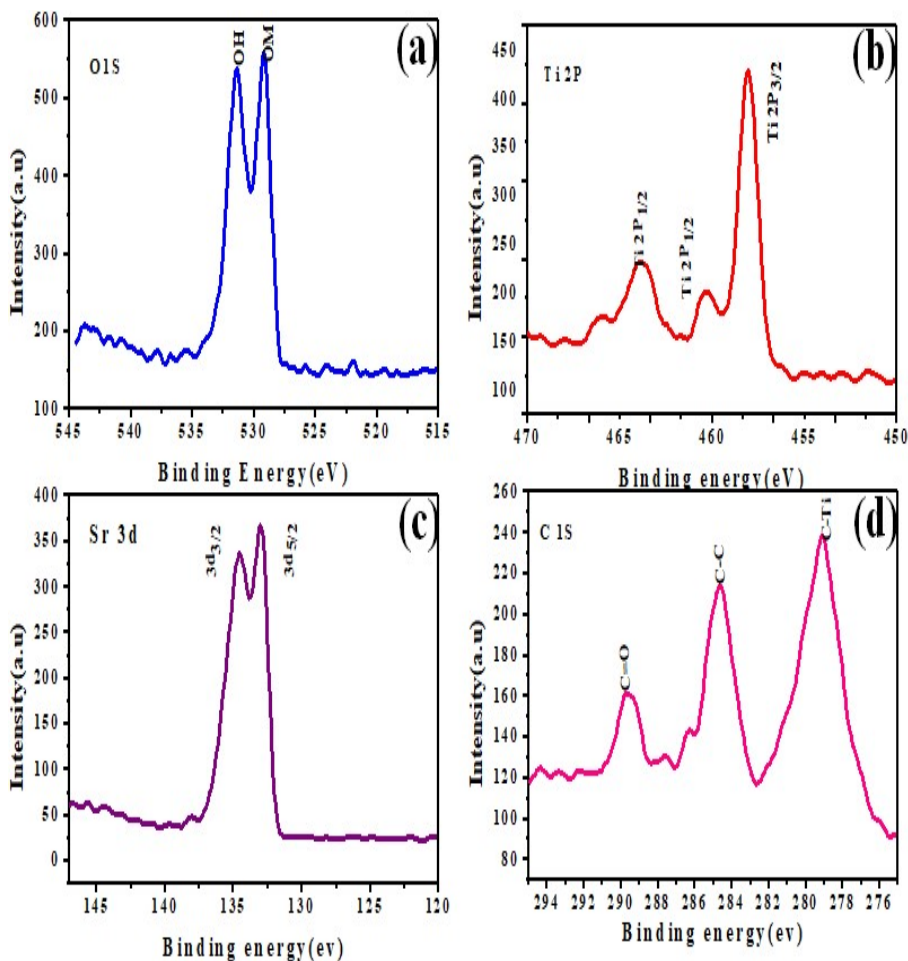


Figure 8.5 High-resolution XPS data of MSTO. (a) O 1s region, (b) Ti 2p region, (c) Sr 3d region, (d) C 1s region respectively.

We investigated the elemental composition of the prepared materials by X-ray photoelectron spectroscopy (XPS). The XPS spectrum of oxygen binding energy regions shown in Figure 8.5(a) indicated two main peaks at 529.2 and 531.4 eV corresponding to the lattice oxygen and surface adsorbed oxygen respectively³⁹. The peaks in the XPS

spectra of MSTO in Figure 8.5(b) around 458.05 and 463.8 eV are attributed to Ti 2p_{3/2} and Ti 2p_{1/2} respectively⁴⁰. The difference in the binding energy of 5.8 eV explains the valency of Ti as Ti⁴⁺. The Ti2p_{1/2} component located at 460.35eV corresponds to the C-Ti-O_x bond⁴¹. In Figure 8.5(c), the peaks at binding energy values 133.05 and 134.45 eV corresponds to Sr3d_{5/2} and Sr3d_{1/2} in which Sr is present in Sr⁺² oxidation state⁴¹. The C 1s peaks in Figure 8.5(d) at 279.5 eV, 284.6 eV, and 289.6 eV corresponds to characteristics bands of C-Ti, C-C, and C=O respectively^{41, 42}. The results of the XPS analysis confirmed the successful synthesis of SrTiO₃.

8.4.6 SEM and TEM studies

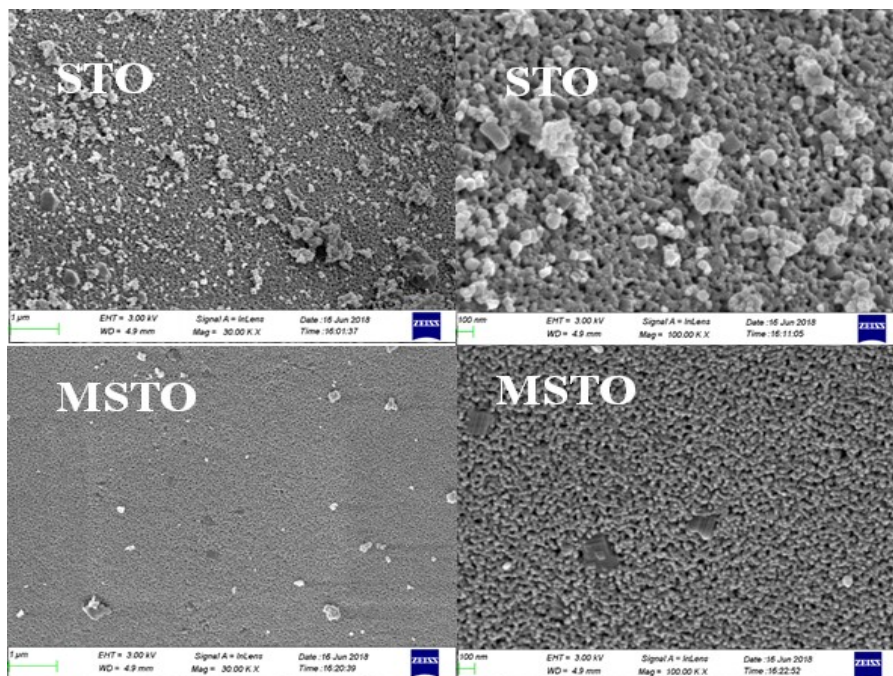


Figure 8.6 SEM images of STO and MSTO samples

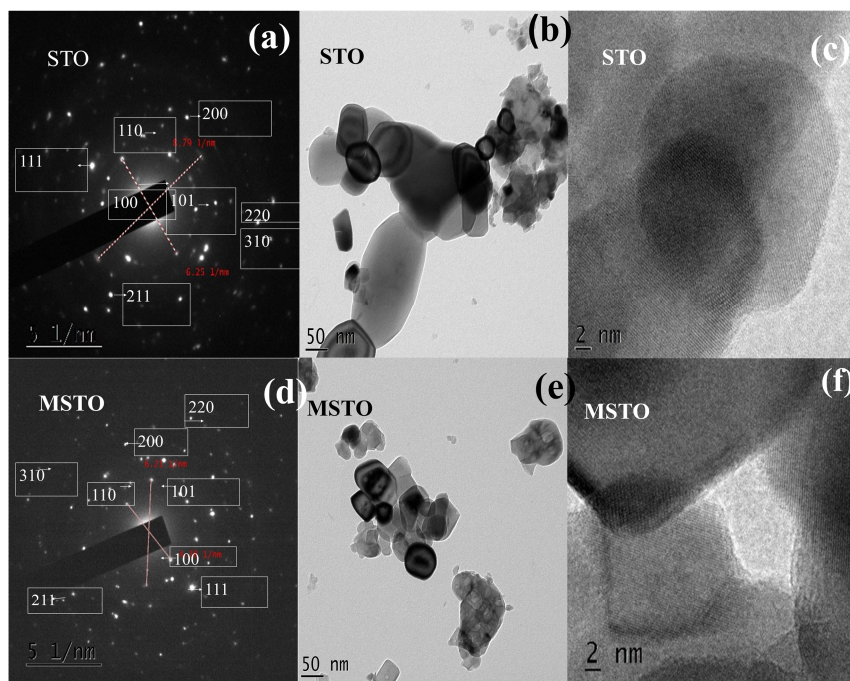


Figure 8.7 SAED patterns, TEM AND HRTEM images of STO and MSTO (a)SAED patterns of STO (b)TEM image of STO (c)HRTEM image of STO (d) SAED patterns of MSTO (e) TEM image of MSTO (f) HRTEM image of MSTO

The morphologies of Strontium titanate photocatalyst prepared in the presence and absence of structure-directing agent pluronic P123 were examined using the Scanning electron microscope. The SEM images (Figure 8.6) revealed bimodal particle distribution with small spherical particles and cubical particles. From the SEM images, it appeared that aggregation and clumping were much less pronounced in the STO and MSTO samples. The detailed structural properties of STO and MSTO samples were analyzed by TEM. The HR-TEM images of STO and MSTO were shown in Figure 8.7. The average particle size of spherical and cuboidal structures in STO and MSTO was 55 nm and 38

nm respectively. The results confirmed that the particles were in the nanometric regime. The measurements obtained from the SAED patterns for STO and MSTO samples were inconsistent with the strontium titanate plane space and clearly provided a deep understanding of the perovskite structure of the titanate nanostructure.

8.4.7 PL studies

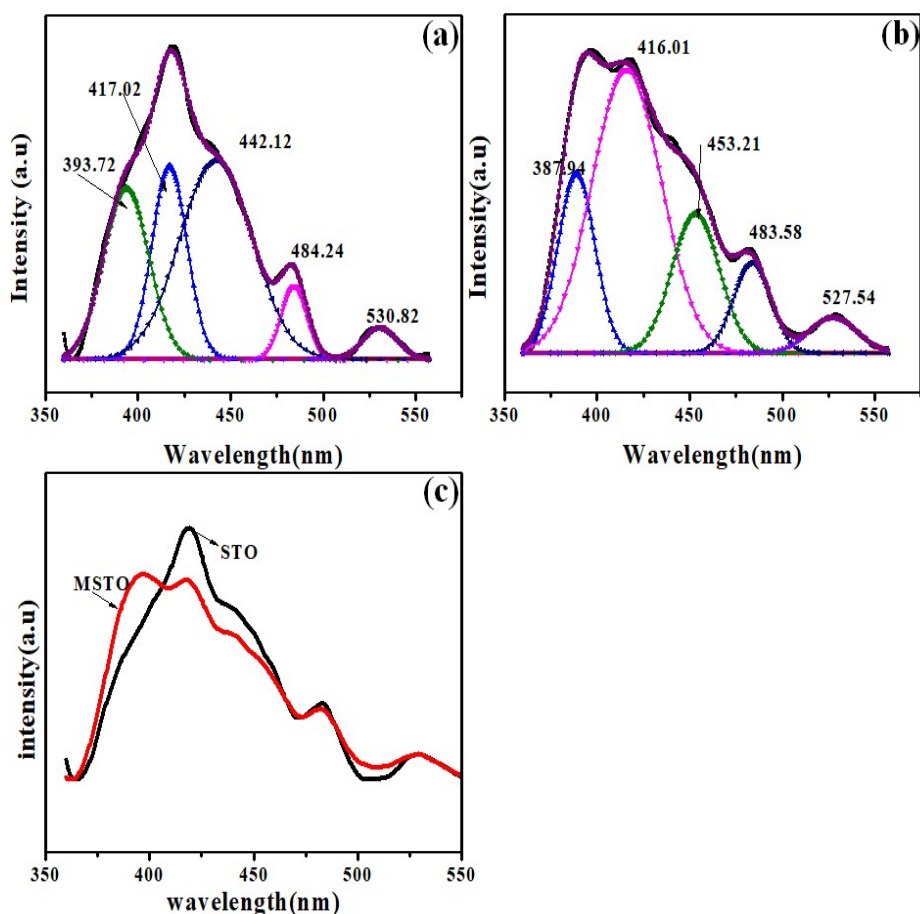


Figure 8.8 Photoluminescence emission spectra originate from various defect levels of (a) STO (b) MSTO, (c) the relative photoluminescence emission of STO and MSTO

The broad PL emissions observed for MSTO and STO were shown in Figure 8.8(a) and 8.8(b) respectively. The modification of MSTO has resulted in an appreciable change in the photoluminescence intensity. The STO's resolved peaks exhibited in Figure 8.8(a) are associated with various transitions that occurred due to its high sensitivity towards visible light. The same results were also obtained for MSTO with slightly displaced peak centers (Figure 8.8(b)). The emission band at 393 nm and 387 nm are related to shallow defect levels in strontium titanate⁴³. The intense broad emission 417 and 416 nm have resulted from the recombination of excited electrons and holes through the defect level and the emission at 442 and 453 nm can be attributed to the recombination of excited electrons and holes through their self-trapped excited states. The other two emissions were relatively weak and are deep level defect correlated emissions⁴⁴. The PL intensity of MSTO was quenched in comparison to that of STO ((Figure 8.8(c)). This might be due to the better charge separation in the mesoporous structure that resulted in the higher density of charge carriers.

8.5 Photocatalytic activity

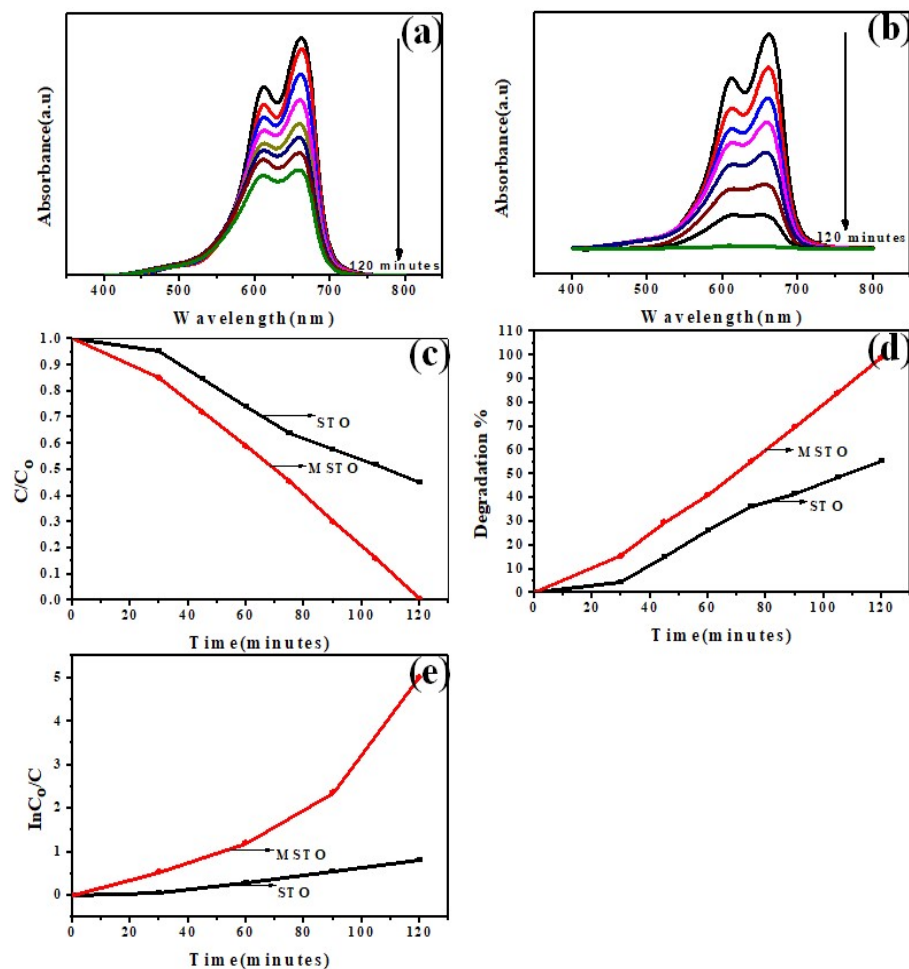


Figure 8.9 UV absorption Spectra of photocatalytic degradation of methylene blue in the presence of UV light irradiation (a) STO as photocatalyst (b) MSTO as a photocatalyst (c) C/C_0 versus time of methylene blue degradation under UV irradiation (d) percentage of degradation of methylene blue using STO and MSTO photocatalyst materials under UV irradiation (e) $\ln C_0/C$ versus time of methylene blue degradation using STO and MSTO photocatalyst material under UV irradiation

Photocatalytic degradation of methylene blue was performed using MSTO catalyst whose performance was compared with that of STO catalyst. The UV-Vis spectra of methylene blue degradation recorded for STO and MSTO catalysts are depicted in Figure 8.8 (a) and Figure 8.8 (b) respectively. In the comparative study on photocatalytic activity using 10^{-4} M methylene blue solution under UV source of illumination, the complete degradation of methylene blue was achieved within 120 minutes. The decrease in the concentration of dye was monitored by measuring the absorbance of the solution using a UV-Visible spectrophotometer. The efficiency of the degradation experiment was evaluated by using the equation

$$\text{Degradation percentage} = ((C_0 - C_t) / C_0) \times 100 \%$$

C_0 and C_t represent the concentration of methylene blue at the time '0' and 't' respectively. Figure 8.8 (d) illustrates the degradation efficiency of methylene blue versus irradiation time of MSTO and STO catalysts. It could be observed that the degradation efficiency of methylene blue enhanced greatly in the presence of MSTO catalyst. Figure 8.8(e) indicates a linear relationship between $\ln(C_0/C)$ and time, illustrating that the photocatalytic degradation of methylene blue followed the first-order kinetics. The rate of degradation experiment can be expressed using the equation

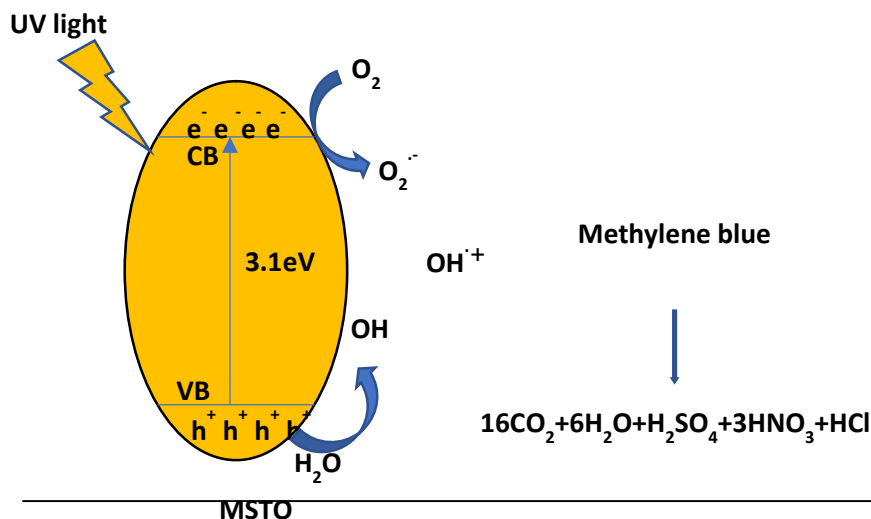
$\ln C_0/C = kt$, Where C_0 is the initial concentration of the dye methylene blue, C is the concentration of methylene blue at time t , k is the apparent rate constant. In Figure 8.8(e), $\ln C_0/C$ varied linearly with time which indicated the first-order kinetics with regression coefficient 0.95 and 0.85 for STO and MSTO respectively. The values of rate

constant obtained for STO and MSTO materials were 0.007 and 0.04 respectively. The photocatalytic activity of MSTO was found 5.65 times faster than STO as the mesoporous structures possessed nanoscale channel walls that allowed the rapid arrival of the photogenerated electrons and holes to the surface⁴⁵. This enhanced the charge transfer efficiency and suppressed the electron-hole recombination. Moreover, the low band gap and high density of charge carriers in MSTO samples facilitated the higher activity of MSTO compared to that of STO. The argument was well supported by DRS spectra and PL measurement. In the case of the STO photocatalyst, the low photocatalytic activity might be due to the formation of non-porous structures.

Photocatalyst	Regression coefficient(R^2)	K_{app} (min) ⁻¹
STO	0.95	0.007
MSTO	0.85	0.04

Table.2 Value of regression coefficient and rate constant

8.6 Mechanism



The degradation mechanism in this structure recites as follows, on irradiation with UV light the electrons in the valence band of strontium titanate are promoted to the conduction band thereby leaving holes in the valence band. The holes react with surface adsorbed water producing hydroxyl radicals ($\text{OH}\cdot$) whereas the electrons in the conduction band react with dissolved oxygen generating superoxide anions ($\text{O}_2^{\cdot-}$) which subsequently reacts with H^+ to generate hydroxyl radicals ($\text{OH}\cdot$). The hydroxyl radicals ($\text{OH}\cdot$) with high oxidizing ability degrade the methylene blue dye. The high density of charge carriers presents in the mesoporous structures enabled the complete degradation of methylene blue ⁴⁶.

8.7 Conclusion

Mesoporous strontium titanate nanomaterial was synthesized by a cost-effective sol-gel combustion method with high chemical purity and pronounced crystallinity using pluronic P123 and citric acid as a structure-directing agent and complexing agent respectively. Citric acid addition resulted in the enhanced purity and crystallinity of the samples. The present study revealed that the triblock copolymer was essential for the generation of mesostructure. The measurements obtained from the SAED pattern for STO and MSTO samples were consistent with the strontium titanate crystal plane obtained from XRD results. The UV-Vis DRS spectra showed a significant reduction in band gap energy when samples were reformed into mesoporous. The photoluminescence studies showed various excitations and transitions favorable for photocatalytic activity. The study summarizes that the

mesoporous strontium titanate is an excellent photocatalyst that can degrade methylene blue effectively. Moreover, the photocatalytic performance of mesoporous strontium titanate prepared using P123 was enhanced 5.65 times faster than strontium titanate. Based on the observations we can conclude that strontium titanate synthesized using pluronic P123 is a promising photocatalytic material for the environmental remediation process and also for related applications.

REFERENCES

1. Kiran S.V, Rajesh J. T, Kinjal J. S, Pradyumna J, Atindra D.S, Vimal G. G, *Water-Energy Nexus*, 2020, 3, 46–61
2. Joshi U.A, Lee J.S, *Nano-Micro Small* 2005, 12, 1172–1176
3. Hara S, Yoshimizu M, Tanigawa S, Ni L, Ohtani B, Irie H, *J. Phys. Chem. C*, 2012, 116, 17458–17463
4. Moniruddin M, Afroz K, Shabdan Y, Bizri B, Nuraje N, *Applied Surface Science*, 2017, 9, 886–892
5. Urban J.J, Yun W.S, Gu Q, Park H, *J. Am. Chem. Soc*, 2002, 124, 1186–1187
6. Browning N.D, Osterloh F.E, Townsend T.K, *ACS nano*, 2012, 6, 7420–7426
7. Junfang L, Hua B, Wencai Y, Jingyao L, Yahui L, Qing Z, Haifeng Y, Guangcheng X, *Nano Research*, 2016, 9, 1523–1531
8. Wenli Z, Wei Z, Guilian Z, Tianquan L, Fangfang X, Fuqiang H, *Cryst Eng Comm*, 2015, 17, 7528–753
9. Liang C, Shouchen Z, Liqiu W, Dongfeng X, Shu Y, *Journal of Crystal Growth*, 2009, 311, 746–748
10. Henrique A, Osmando F.L, Caue R, Valmor R.M, 2015, 30, 651–657
11. Lei S, Chunyang Z, Yuzhou J, Tiejun W, Noritatsu T, *Catal. Sci. Technol* 2012, 2, 2569–2577
12. Macaraig L, Chuangchot S, Sagawa T, *Journal of Materials Research*, 2014, 29, 123–130
13. Dogan M, Ozdemir Y, Alkan M, *Dyes and Pigments*, 2007, 75, 701–713
14. Karimi L, Zohoori S, Yazdanshenas M.E, *Journal of Saudi Chemical Society*, 2014, 18, 581–588
15. Correia V.M, Stephenson T, Judd S.J, *Environmental Technology*, 1994, 15, 917–929
16. Hameed B.H, Ahmad A.L, Latiff K.N.A, *Dyes and pigments*, 2007, 75, 143–149

17. Lakshmi S, Renganathan R, Fujita S, Journal of Photochemistry and Photobiology, A, Chemistry, 1995, 88 163-167
18. Umebayashi T, Yamaki T, Tanaka S, Asai K, Chemistry Letters, 2003, 32, 330-331
19. Shelly B, Jacques E.M, Keith B, Michael G, J. Phys. Chem. B, 1999, 103: 9328–9332
20. Zheng J, Jie Y, Xu J, Qiang B, Materials Letters 2013, 100, 62-65
21. Bugra E.K, Young J.L, Andreas K, Silvia G and Massimiliano D.A, Simone M, RSC Adv , 2016, 6, 90401- 90409
22. Lei S, Chunyang Z, Yuzhou J, Tiejun W, Noritatsu T, Catal. Sci. Technol , 2012, 2, 2569-2577
23. Guodon X, Hengming Z, Junji Z, Jun X, Journal of Crystal Growth, 2005, 279, 357–362
24. Bhagwata V.R, Ashok V.H, More S.D, Jadhav K.M, Materials Science and Engineering: B, 2019, 248, 114388
25. Tarawipa P, Thammanoon S, Susumu Y, Sumaeth C, Journal of Molecular Catalysis A: Chemical, 2008, 287, 70–79
26. Wei X, Xu G, Ren Z, Xu C, Weng W, Shen G, Han G, J. Am. Chem. Soc, 2010, 93, 1297-1305
27. Zheng J.Q, Zhu Y.J, Xu J.S, Lu B.Q, Qi C, Chen F, Wu J, Materials Letters , 2013, 100, 62–65
28. Fei Z, Zhen J, Xiaoqin Q, Yongxiang Z, Luyun J, Jinfang Z, Tiancun X and Peter P.E, Chem. Commun , 2012, 48.8514–8516
29. Zhengcui W, Yali Z, Xia W, Zexian Z, New J. Chem, 2017, 41 , 5678-5687
30. Peng L, Xueli H, Yujie L, Meng Z, Xiaoping L, Youzhou H, Fan D, Min F, Zhi. Z, RSC Adv, 2018, 8, 6315–6325 |
31. Shahabuddin S, Muhamad SN, Mohamad S, Joon C, Polymers, 2016, 8, 27
32. Thamarai S, Thiripuranthagan S, Applied Catalysis B: Environmental, 2017, 207, 218–230
33. Yongmei X, Zuming H, Yalin L, Bin T, Shunping S, Jiangbin S, Xiaoping.L, RSC Adv , 2018, 8, 5441-5450

34. Minh NH, Feng Z, Zhifu L, Lichao W, Lanyon L, Guanzhong L, Zhe Z, RSC Adv , 2016, 6, 21111-21118
35. Li L, Lin R, Tong Z, Feng Q, Nanoscale Research Letters, 2012, 7, 305
36. .Fernandes F.R.D, Pinto F.G.H.S, Lima E.L.F, Souza L.D, Caldeira V.P.S, Santo A.G.D, Appl. Sci. 2018, 8, 725
37. Zhelin W, Xuewei J, Mao P and Yongmin S, Minerals, 2020, 10, 377
38. Leofanti G, Padovan M, Tozzola G, Venturelli B, Catalysis Today, 1998, 41, 207-219
39. Kovalevsky A.V, Populoh S, Patricio S.G, Thiel P, Ferro M.C, Fagg D.P, Frade JR, Weidenkaff A, J. Phys. Chem. C , 2015, 9, 4466–4478
40. Tiantian C, Peng H, Kaichen Z, Ziqi S, Kai Z, Ligang Y, Kang C, Nin. C, Yongfang L, J. Mater. Chem. A , 2018, 6 , 435–3443
41. Yuan M, Zhengjie W, Haiwang W, Guanqi W, Yukai, Z, Pengcheng H, Yuanming L, Dekua. G, Hongqin P, Bingzhu W, Xiwei Q, Cryst Eng Comm, 2019, 21 , 3982-3992
42. Qi X.X, Jianjian F, Je M.Y, Rajaram S.M, Kwang H.K, RSC Adv , 2017, 7, 11000-11011
43. Ioannis T, Dong L, Fang X.X, Jian X, Ioannis T.P, Teddy S, Bin L, Qichun. Z, Stelios AC, Gerasimos S.A, Applied Catalysis B: Environmental, 2018, 236, 338-347
44. Kumar V, Choudhary S, Malik V, Nagarajan R, Kandasami A, Subramanian A, Phys. Status Solidi A , 2019, 216, 1900294
45. Subha N, Mahalakshmi M, Myilsamy M, LakshmanaReddyN, Shankar M.V, Neppolian B, Murugesan, Colloids, and Surfaces A: Physicochem. Eng. Aspects, 2017, 522, 193–206
46. Ahmed M.A, Abou-Gamra Z.M, Salem A.M, Journal of Environmental Chemical, 2017, 5, 4251-4261

CHAPTER 9

OVERALL CONCLUSION AND FUTURE OUTLOOK

Contents

9.1 Overall conclusion

9.2 Summary

9.3 Conclusions

9.4 Future outlook

9.1 Overall Conclusion

Our research work aimed to explore mixed, binary, and ternary nano metal oxide structures for energy generation and environmental remediation. Synthetic strategies like the sol-gel method and sol-gel combustion method were adopted for the synthesis of semiconducting nano metal oxides. The metal oxides were employed for various applications like photocatalytic water splitting, dye degradation, and drug degradation. We have included the introduction and experimental parts in Chapters 1 and 2. The entire research works are highlighted from chapter 3 to 8.

9.2 Summary

Chapter 3 deals with the synthesis, characterization, and photocatalytic application of mesoporous TiO_2 and mesoporous $\text{TiO}_2/\text{RuO}_2$ nanosystem. Evaluation of photocatalytic performance was done by conducting methylene blue degradation experiment under sunlight. The photocatalytic degradation of methylene blue was found to be improved by the introduction of RuO_2 to the catalytic system. The complete degradation of methylene blue was achieved within 40 minutes under sunlight illumination. The photocatalytic experiment was found to be influenced by various factors like catalyst weight, the concentration of dye, and the concentration of ruthenium dioxide. The degradation experiment followed first-order kinetics.

Chapter 4 deals with the synthesis and characterization of ternary metal oxide $\text{TiO}_2/\text{RuO}_2/\text{CuO}$ mesoporous nanostructures with the aid of structure-directing agent triblock copolymer, pluronic P123. The

catalyst was prepared via the sol-gel route. Various characterization techniques, UV-Vis-DRS powdered X-ray diffraction (XRD), X-ray photoelectron spectroscopy (XPS), Field emission scanning electron microscopy (FE-SEM), Transmission Electron microscopy (TEM), Brunauer–Emmett–Teller (BET) adsorption-desorption technique were employed for the analysis of the photocatalysts. The results revealed the successful formation of mesoporous $\text{TiO}_2/\text{RuO}_2/\text{CuO}$ structures.

Chapter 5 discusses the application of catalytic system $\text{TiO}_2/\text{RuO}_2/\text{CuO}$ for H_2 production via water splitting reaction. A comparative study on H_2 evolution was performed using catalysts mesoporous $\text{TiO}_2/\text{RuO}_2/\text{CuO}$, mesoporous $\text{TiO}_2/\text{RuO}_2$, and mesoporous TiO_2 . The maximum evolution of H_2 was observed when mesoporous $\text{TiO}_2/\text{RuO}_2/\text{CuO}$ was used as a photocatalyst. The H_2 evolution was monitored by varying various parameters like the weight of the catalyst, concentration of CuO, amount of sacrificial agent, and chain length of the sacrificial agent. Continuous irradiation of the photocatalyst for 18 hours resulted in the maximum evolution of 20.7 mmol of H_2 . The present study demonstrated that the ternary mesoporous system can be used as an efficient photocatalytic system for water splitting reactions.

Chapter 6 deals with the comparative study on photocatalytic sunlight-assisted mineralization studies of the antibiotic cefixime using the photocatalysts mesoporous $\text{TiO}_2/\text{RuO}_2/\text{CuO}$, mesoporous $\text{TiO}_2/\text{RuO}_2$, and mesoporous TiO_2 . The ternary system mesoporous $\text{TiO}_2/\text{RuO}_2/\text{CuO}$ proved to be the most efficient photocatalyst for the

mineralization of cefixime. The degradation experiment was found to be influenced by various parameters like concentration of antibiotic, irradiation time, the mass of the catalyst, and concentration of CuO. The present study revealed that mesoporous TiO₂/RuO₂/CuO is an excellent photocatalyst for controlling antibiotic-resistant bacterial strains.

In Chapter 7, the synthesis, characterization, and photocatalytic application of TiO₂, TiO₂/ZnO, and TiO₂/ZnO/Fe₂O₃ nanocomposite were described. The photocatalysts have been synthesized by a facile sol-gel method. We have conducted a detailed study on the photocatalytic performance of the catalysts. From the comparative study of the degradation experiments, TiO₂/ZnO/Fe₂O₃ showed maximum photocatalytic performance. The photocatalytic activity was evaluated by methylene blue degradation. The degradation experiment was conducted under sunlight. The complete degradation of dye was achieved within 130 and 170 minutes under UV and sunlight irradiation for the photocatalyst TiO₂/ZnO/Fe₂O₃. From the kinetic studies, it was revealed that photocatalysis followed first order kinetics.

In chapter 8 the comparative study on the synthesis, characterization, and photocatalytic application of SrTiO₃ prepared in the presence and absence of pluronic P123 was presented. A facile sol-gel method followed by combustion was adapted for the synthesis of SrTiO₃. The photocatalytic performance was monitored using methylene blue dye. From the kinetic studies, it was found that the photocatalytic activity of mesoporous SrTiO₃ was 5.65 times faster than that of nonmesoporous

SrTiO₃. The degradation followed first-order kinetics. Complete degradation of dye was achieved within 120 minutes. From our studies, it can be proved that mesoporous SrTiO₃ prepared in the presence of structure-directing agent pluronic P123 is a promising candidate for the photocatalytic degradation of methylene blue.

In chapter 9 we have presented a brief summary of the research work.

9.3 Conclusions

The major conclusions derived from the present research work are the following:

- Introduction of RuO₂ to the mesoporous framework of TiO₂ was found to be highly beneficial for the sunlight assisted degradation of methylene blue
- Mesoporous TiO₂/RuO₂/CuO was found to be an excellent photocatalyst for applications like photocatalytic H₂ evolution and sunlight-assisted photocatalytic degradation of antibiotic cefixime.
- TiO₂/ZnO/Fe₂O₃ nanocomposite can be employed for the complete mineralization of methylene blue dye.
- The structure-directing agent pluronic P123 played a prominent role in enhancing the photocatalytic performance of SrTiO₃.

9.4 Future Outlook

The increased level of CO₂ in the atmosphere is a major contributing factor to global warming¹. To combat this issue there needs a robust catalyst that reduces the CO₂ effectively utilizing solar energy. The photocatalytic reduction is an effective method for the conversion of CO₂ into hydrocarbon fuels as it contributes to industrial raw materials along with the reduction process, i.e., the reduction process results in the generation of methanol, carbon monoxide, methane, formaldehyde, and formic acid². The prepared photocatalyst, mesoporous TiO₂/RuO₂/CuO proved to be an excellent candidate for photocatalytic water splitting and sunlight-assisted antibiotic degradation. From the excellent photocatalytic performance of mesoporous TiO₂/RuO₂/CuO, it is expected that the catalyst can be chosen for the photocatalytic CO₂ reduction process. The catalysts that we have developed i.e., mesoporous TiO₂/RuO₂/CuO, can also be implemented for sunlight-assisted H₂ generation. In addition to these experiments, it can also be chosen for generating H₂ electrochemically.

REFERENCES

1. Nahar S, Zain M.F.M, Kadhum A.A.H, Hasan H.A, Hasan M.R, Materials, 2017 , 6, 629.
2. Qiu-Ye L, Lan-Lan Z, Chen L, Yu-Hui C, Xiao-Dong W, Jian-Jun Y, Advances in Condensed Matter Physics, 2014. <https://doi.org/10.1155/2014/316589>

LIST OF PUBLICATIONS

Paper accepted

1. Core Level X-ray Photo-Electron Emission Spectra and Structure-Surface Related Multi-Excitonic Photoluminescence with Reduced Recombination Rate in Mesoporous TiO₂/RuO₂/CuO Nanomaterials, Juliya Acha Parambil, Abdul Mujeeb V.M, Sreenivasan K.P, Jayaram P, Journal of Sol Gel Science and Technology

Papers Communicated

1. Enhanced H₂ evolution via photocatalytic water splitting using mesoporous TiO₂/RuO₂/CuO ternary nanomaterial, Juliya A. P, Abdul Mujeeb V.M, Sreenivasan K Parayil, Muraleedharan K, Journal of photochemistry and photobiology A
2. P123 Assisted Sol- Gel Combustion Synthesis of Mesoporous Strontium Titanate Nanomaterials for Photocatalytic Degradation of Methylene Blue, Juliya Acha Parambil, Abdul Mujeeb V.M, Sreenivasan K Parayil, Indian Journal of Chemistry
3. Enhanced Photocatalytic Degradation of Methylene Blue Using TiO₂/ZnO/Fe₂O₃ Ternary Nanocomposite, Juliya A. P, Jayaram P, Abdul Mujeeb V.M, Sreenivasan K Parayil, Muraleedharan.K, Chemical physics Impact

LIST OF PAPERS PRESENTED

1. Juliya.A. P, Sreenivasan.Koliat. Parayil and V.M. Abdul Mujeeb, National Seminar on “Recent trends in materials science (NSRTMS-2019)”, Govt. College Chittur, Palakkad, December 5- 6, 2019.
2. Juliya.A. P, Sreenivasan.Koliat. Parayil, and V.M. Abdul Mujeeb, International seminar on the Emerging Frontiers in Chemical Sciences (EFCS) ”, Farook College, Kozhikode, December 13-15, 2019.